EVALUATION OF GEOMECHANICAL DILATION AND ITS EFFECTS ON SAGD PERFORMANCE

by

Xinkui Wang

A thesis submitted in partial fulfilment of the requirements for the degree of

Doctor of Philosophy

In

Petroleum Engineering

Department of Civil and Environmental Engineering
University of Alberta

ABSTRACT

An effective Steam Assisted Gravity Drainage (SAGD) process requires thermal and hydraulic communication to be established between the injection and the production wells during the start-up operation. To achieve inter-well communication, the conventional steam circulation start-up operations typically take several months. The reductions in the start-up time can have a favourable impact on project economics. A strategy using fluid injection to promote geomechanical dilation of the oil sands, which enhance the inter-well permeability, has been proposed as a SAGD start-up technique. The mechanics of the fluid injection process involve complex interactions of thermal, geomechanical and multiple phase flow behaviours in the inter-well formation region. A better understanding of these interactions in establishing well-pair communication is essential for assessing the potential of deploying this dilation start-up technology and exploring improvements in the overall SAGD recovery performance.

This study intends to examine whether cold-water injection is sufficient to induce enhancements in effective permeability to water from geomechanical dilation mechanisms. An experimental program was first designed to quantify the geomechanical responses under dilation. The reclaimed and cleaned tailing sands from the McMurray Formation were treated to resume and maintain the initial water wettability, and were subsequently used to reconstruct synthetic core specimens. A modified sample preparation technique was developed to create reconstituted, dense,

water-wet and bitumen sand specimens with varying levels of fluid saturations, but with nearly identical porosities. A set of experiments was carried out in a triaxial cell under several reservoir conditions, varying in terms of pressure, temperature, and stress state. The experimental results demonstrated that the effective permeability to water and porosity was greatly enhanced in dilated zones during cold-water injection at modest levels of stress anisotropy. Three geomechanical compression tests were also conducted to obtain the geomechanical properties of the materials.

The triaxial compression tests and the geomechanical dilation tests were then analyzed and served as inputs for the field-scale numerical simulation models. Based on the results of the numerical simulation study, the SAGD performance did not show significant improvement through the enhanced dilation start-up operation due to cold-water injection. This could be considered as an efficient and sustainable solution to quickly establish communication between the well-pair, and to shorten the duration of the start-up phase.

ACKNOWLEDGEMENTS

I would like to first acknowledge Dr. Rick Chalaturnyk for his supervision and guidance, and Dr. Julianna Leung for her co-supervision. It would have been impossible for me to complete this long journey without their encouragement and support.

I would like to express my deepest gratitude to Dr. Haibo Huang for his coordination and co-supervision, who inspired me to pursue continuing education. Without his patience and support, this work would not be possible.

The financial support from InnoTech Alberta (previously Alberta Innovates – Technology Futures, now part of Alberta Innovates) and Energi Simulation Industrial Research Consortia in Reservoir Geomechanics for Unconventional Resources is gratefully acknowledged. I am also grateful to the management personnel of InnoTech Alberta for granting me permission to work on this doctoral study.

I would like to especially thank Dr. Nathan Deisman, the Research Associate, for his technical guidance and help in the numerical simulations. I would like to acknowledge my colleagues and peers at heavy Oil Group of InnoTech Alberta and Reservoir Geomechanics Research Group of University of Alberta for their great technical assistance and support in conducting the lab-scale tests and numerical simulations.

Finally, I would like to extend my love and appreciation to my wife Li Zhang, and my sons Jason RuoChen and Albert RuoYu, for supporting me in every step of my thesis study, and for being so incredibly patient and understanding.

TABLE OF CONTENTS

LIST OF TABLES

LIST OF FIGURES

LIST OF SYMBOLS AND ABBREVIATIONS

C_C:	Coefficient of curvature, or the coefficient of gradation, *Dimensionless*.
C_U:	Coefficient of uniformity, *Dimensionless*.
$C_{op}; C_{gp}; C_{wp}$:	Compressibility of water, oil, and gas, *1/kPa.*
$C_{bp}; C_{pp}; C_{sp}$:	Compressibility of bulk, pore, and solid, *1/kPa.*
$D_{10}; D_{30}; D_{60}$:	Grain diameter at which 10%, 30%, 60% of a sample's mass is finer than in size, respectively, *m.*
D_{50}:	Median diameter of a solid grain, *Dimensionless.*
D_d:	the relative density, *Dimensionless.*
E	Young's modulus, *kPa.*
ε_a:	Axial strain, *%.*
ε_v:	Volumetric strain, *%.*
e_{max}:	Void ratio of the sands packing during the test for the maximum index density, *Dimensionless*.
e_{min}:	Void ratio of the sands packing during the test for the minimum index density, *Dimensionless*.
g:	Acceleration due to gravity, *9.80665 m/s*^{2}.
GOR:	Gas oil ratio, *std* m^3/m^3.
K_a :	Absolute permeability of the medium, *Darcy.*
K_{ew}:	Effective permeability to water, *Darcy.*
k_o:	$k_o = \frac{\sigma_H'}{\sigma_V'}$; stress ratio of the effective horizontal stress (σ_h') to the effective vertical stress (σ_v'), *Dimensionless*.
K_H :	Horizontal permeability of the medium, *Darcy.*
K_V :	Vertical permeability of the medium, *Darcy.*

m:	Mass of the current sands packed in the cell, *grams.*
m_{max}:	Mass of the sands packed in the cell during the test for the minimum index density, *grams.*
m_{min}:	Mass of the sands packed in the cell during the test for the maximum index density, *grams.*
ρ:	Fluid's Density, *gram/cm*^{3}.
ΔP:	Differential Pressure, *kPa*.
Q:	Fluid Flow Rate, *m*^{3}*/s.*
ψ:	Frictional angle, °.
$\emptyset$:	Porosity of the medium, *%.*
$\emptyset_o$:	Initial porosity of the Medium, *%.*
S_{or} :	Residual oil saturation, *%.*
$S_o; S_g; S_w$:	Oil, Gas, and Water Saturation, *%.*
$S_{oi}; S_{gi}; S_{wi}$:	Initial Oil, Gas, and Water Saturation, *%.*
v_R:	Kinematic Viscosity of Oil at Reservoir Temperature, *m*^{2}*/s*.
SOR:	Steam oil ratio, *Dimensionless*.
P_p:	Pore pressure, *kPa.*
P_{atm}:	Atmospheric pressure, P_{atm}=101.325 *kPa.*
p':	Mean effective stress, $p' = \frac{2\sigma'_H + \sigma'_V}{3}$, *kPa.*
q:	Deviatoric stress,$q = \sigma'_1 - \sigma'_3 = \sigma'_V - \sigma'_H$, *kPa.*
$\sigma_1; \sigma_2; \sigma_3$:	The maximum stress, the intermedia stress, and the minimum stress, *kPa.*
$\sigma'_1; \sigma'_2; \sigma'_3$:	The maximum effective stress, the median effective stress, and the minimum effective stress, *kPa.*
σ_H:	Horizontal stress, *kPa.*
σ'_H:	Effective horizontal stress, $\sigma'_H = \sigma_H - u = \sigma_3 - u$, *kPa.*

σ_V: Vertical or axial stress, *kPa.*

σ'_V: Effective vertical or axial stress, $\sigma'_V = \sigma_V - u = \sigma_1 - u$, *kPa.*

σ': Effective stress, $\sigma' = \sigma - u$, *kPa.*

P_p: Pore pressure, *kPa.*

u_c: Critical injection pressure, *kPa.*

V_b: Bulk volume, m^3.

V_p: Pore volume, m^3.

CHAPTER 1. INTRODUCTION

1.1.Overview

The Steam Assisted Gravity Drainage (SAGD) process exhibits success in bitumen recovery in the Athabasca deposit; however, massive energy consumption and greenhouse gas emissions are the main concerns. Currently, approximately 280–350 kWh of energy is required to produce one barrel of oil from the oil sands, which corresponds to almost 75 kilograms of greenhouse gas emissions. The reduction of operating costs and environmental impacts are of the utmost practical importance in petroleum engineering. Optimization of the SAGD operation for maximizing wellbore productivity is one approach to achieve this target.

The SAGD start-up phase may be optimized to reduce operating costs. A complete cycle of SAGD includes start-up, semi-SAGD, full SAGD, and post-SAGD. A conventional SAGD start-up scheme involves steam or hot water circulation, during which either steam or hot water is injected into both the injection well and the production well to heat up the near-wellbore regions and the inter-well areas.

Enhanced start-up methods, e.g. cold-water dilation and steam dilation, involve the interactions of geomechanical responses and multiphase flow behaviours in the inter-well formation. Assessment of such interactions requires detailed experimental studies of the geomechanical responses of the oil sands formation during different stress and loading conditions. However, studies of these interactions during SAGD start-up operations in the literature have been scarce. In this research, a set of lab-scale experiments and numerical simulations are conducted to understand the mechanics and fundamentals of dilation during the SAGD start-up operation.

This study focuses on a particular dilation-based start-up operation strategy, which is a cold-water injection. The concept of enhanced start-up technology has recently

been proposed and deployed in several SAGD pilot well pairs, and the preliminary results point to the potential of dilation start-up in improving the overall SAGD recovery performance. It is hypothesized that fluid injectivity can be enhanced by creating positive geomechanical dilation via cold-water injection. One of the potential benefits of improved injectivity is expected to enable high convective heat flux, hence shorten the time for steam initialization prior to full SAGD commencement. It is expected that dilation could significantly increase the porosity in the near-well region, and it can be achieved through managing initial stress state and injection strategy prior to steam initialization; it is anticipated that the fluid injectivity in the dilated zone can be enhanced at modest levels of initial stress anisotropy.

This study aims to assess the effectiveness of dilation start-up in SAGD operations. Upon achieving a positive experimental result and satisfactory modelling, an enhanced start-up operation strategy such as cold-water dilation could be considered for oil sands and bitumen recovery. The research will assess whether cold-water injection can be implemented as an effective dilation start-up strategy to reduce steam (water and energy) usage and carbon dioxide emissions.

The metrological approaches include lab-scale experiments and numerical simulation. A set of physical experiments is designed to reproduce realistic field conditions in terms of pressure, temperature, and stress states and to study the interaction between geomechanical effects and fluid flow behaviours during cold-water injection conditions. Based on the laboratory results, a coupled hydrodynamic-geomechanical model is developed using Itasca's FLAC3D (reference?) to compute the enhanced porosity/permeability in the dilated zones, which are subsequently provided as inputs to the reservoir flow simulation model using CMG's STARS (reference?) for evaluating the impacts of dilation on the full phase of SAGD performance.

Considering the difficulties to extract a field core plug, synthetic sands cores are evaluated in a set of tests. These core specimens are representative of the

undisturbed McMurray Formation, as they are prepared with clean dry sands obtained from the McMurray Formation. The study intends to provide a comprehensive set of experimental data involving a dozen artificial specimens. It aims to investigate the operating conditions favouring dilation and evaluate the impacts of cold-water injection on the full SAGD performance. Successful implementation of dilation start-up may result in a more cost-effective process, with less steam consumption and carbon dioxide emissions. The geomechanical dilation strategy is expected to significantly increase the porosity in the near-well region and the effective permeability to water through the management of the injection schemes at modest levels of initial stress anisotropy. Fluid injectivity is thus enhanced in the dilated zone prior to steam initialization.

1.2. Problem Statement

Geomechanical dilation can potentially reduce the time required for the SAGD start-up phase. Achieving geomechanical dilation through fluid (water, steam, or solvent) injections was recently proposed and deployed in several SAGD pilot well pairs to enhance SAGD start-up, (Lin *et al.*, 2016) in Canada and China. Success with dilation enhancement was reported at some SAGD projects (Cenovus, 2014) (Lin *et al.*, 2016; Fan *et al.*, 2017).

Several unresolved issues must be addressed before the technology is accepted for wide-scale implementation. There is a lack of verifiable data and knowledge to offer definitive conclusions. There are limited mathematical models and empirical correlations for representing the interaction between geomechanical response and multiphase flow behaviours in porous media; the main physical mechanisms involved in dilation due to cold-water injection are not fully understood. There is a lack of understanding on the effective promotion of geomechanical dilation, and the correlation between volumetric strain, permeability, and pore pressure during water injection at in-situ stress state and temperature conditions of an oil sands reservoir. Specifically, the impact of the stress path on the dilation process, as well as the interactions between geomechanical response and multi-phase flow

behaviours during cold-water injection are determined to be minimal in the previous studies.

Moreover, laboratory experiments and field practices have not been sufficiently comprehensive to define the petrophysical and favourable geomechanical conditions under which dilation enhancement is effective and feasible for SAGD field operation. It is still difficult to achieve consistent success by deploying the dilation-based start-up strategy in a selected well pair.

With sufficient oil sands characteristics obtained through lab-scale testing, a numerical model can then be built. The impact of a dilation-based start-up on full SAGD performance can be assessed through the numerical simulation.

1.3. Research Objectives & Scope of The Research

This study aims to investigate the fundamentals of dilation-based start-up operations and to assess its feasibility at field-scale conditions. It focuses on the impact of the stress path on dilation in terms of the interactions between geomechanical response and multiple phase flow behaviours during the cold-water injection. Results from the experimental study are used to establish various correlations between reservoir properties (i.e., porosity and effective permeability to water) and geomechanical responses (i.e., effective stress and volumetric strain), which are then used to construct a coupled hydrodynamic-geomechanical simulation model and a reservoir flow simulation to assess the impact of geomechanical dilation over the entire SAGD production life at field scale. The three main objectives of this study are:

- Formulating a comprehensive experimental program for measuring the geomechanical responses and variations in reservoir properties during the dilation process;
- Establishing empirical correlations between porosity and effective permeability to water with effective stress and volumetric strain, while considering the impacts of stress paths on dilation.

- Constructing field-scale models coupling multiphase flow simulations with geomechanical calculations to quantify the impacts of dilation start-up on SAGD production performance.

A set of lab-scale experiments are proposed in which multiphase flow behaviours and geomechanical responses are examined. This involves conducting a set of triaxial tests on both bitumen-rich/free core specimens. The main testing activities include, but are not limited to the following:

1) Examining the effects of initial isotropic stress state on dilation;
2) Examining the effects of initial anisotropic stress state on dilation;
3) Examining the effects of fluid saturation on dilation;
4) Examining the effects of pore pressure on dilation;
5) Evaluating the effects of injection rate on dilation;
6) Examining favourable conditions for cold-water injection to enhance fluid injectivity in oil sands formation;
7) Evaluating the permeability variation with geomechanical dilation;
8) Generating the Mohr-Coulomb failure envelope of the core specimen tested and obtaining other geo-properties.

Two sets of the lab-scale triaxial tests are performed: geomechanical dilation and triaxial compression. The tests will generate new correlations between porosity/effective-permeability with volumetric stress at an elevated effective strain at reservoir temperature, which can then be incorporated in the numerical simulation.

The goal of the numerical simulation is to build up a numerical model, which can capture the main mechanisms of geomechanical dilation on an element through a

set of lab-scale tests. The influence on the SAGD performance of the dilation start-up can then be assessed accordingly for a field-scale SAGD application.

The study addresses only dilation start-up through cold-water injection. Several other options for dilation-based start-up, including cyclic injection, hot water, steam, and solvent injection are beyond the scope of this research.

1.4.Structure of the Thesis

This study addresses dilation-based enhancement by promoting positive geomechanical dilation through cold-water injection. This dissertation is organized into the following chapters:

It begins with CHAPTER 1, which including the problem statement, research objectives, and the structure of the thesis.

CHAPTER 2 presents with a literature review of topics pertinent to the establishment of inter-well communication in oil sands formations; in particular, the interactions between geomechanical dilation and multiphase flow in oil sands are described; finally, several field examples of dilation-based start-up technology are presented.

The research methodology and the characterization of the materials tested in the study are presented in CHAPTER 3, followed by the experimental design and setting for a geomechanical dilation test. It discloses some improved techniques to obtain and densify the almost identical synthetic core specimens. This greatly enhances the specimen quality, while also ensuring reliability, repeatability, and representatively of a testing specimen. This chapter also presents geomechanical properties and parameters obtained through triaxial compression tests at elevated effective stress, which could serve as inputs in the numerical simulation models.

CHAPTER 4 delivers the experimental results related to the geomechanical dilation tests. The verification of the concept of geomechanical dilation is conducted through cold-water injection dilation as a SAGD start-up technique. The lab-scale test demonstrates the feasibility of geomechanical dilation and the test results are presented in terms of phase flow behaviours in the porous media due to cold-water injection. This chapter also presents a semi-analytical model based on the failure envelopes, which suggests the minimum injection pressure required to reach plastic dilation.

Error! Reference source not found. discusses a reservoir-geomechanical model to assess the impacts of dilation start-up on the overall SAGD recovery performance, which consists of a geomechanical model and flow model. It also presents the assessment results based on a field size SAGD well pair using the numerical model established in this chapter.

CHAPTER 6 summarizes the research study and provides a recommendation for future works.

CHAPTER 2. LITERATURE REVIEW

2.1. Inter-well Communication Establishment in Oil Sands Formations

The SAGD process was initially proposed and disclosed by Butler and Stephens (Butler and Stephens, 1981). Prior to a full SAGD operation, the communication between two inter-wells in oil sands formations must be established. Only after the thermal and hydraulic communication is established between the injection well and the production well, can the SAGD process fully commence.

Over the last few decades, researchers and industry engineers (Butler and Stephens, 1981; Stone, Edmunds and Kristoff, 1989; Edmunds and Gittins, 1991; Khodaverdian and McElfresh, 2000; Abbate et al., 2013, 2014) have made efforts to speed up communication between the well pairs and start-up operations in oil sands and to address the issues of low injectivity. To increase fluid injectivity in the formation and to achieve a high fluid injection rate, two common strategies are adopted: (1) imposing a high fluid injection pressure, and (2) transferring thermal energy into the formation by means of heat conduction through hot water flooding or steam circulation.

The major concern with a high-pressure injection in SAGD is that fractures might be induced during the injection. If fractures are created before full SAGD commences, injected steam could easily channel through the fractures and bypass much of the formation. Additionally, a high injection pressure could greatly compromise the caprock's integrity, enabling fluids to travel to the surface or below the reservoir and connect to other formations with bottom water/top gas. Therefore, the injection operating pressure should be maintained below the maximum principal stress of the local reservoir.

Butler developed a classical start-up operation strategy prior to commencing a full SAGD process (Butler, 1979). Steam circulates separately for some time through

each of the injection and production wells to heat the oil sands near the wellbore in the formation and establish thermal and fluid communication between the inter-wells. Thermal conduction heats the oil sands formation by injecting steam through the tubing and returning the fluid mixture of steam, condensed water, and oil through the annulus of tubing and casings at a pressure below the fracture pressure.

It will usually take up to one full year to obtain communication between the inter-wells for a conventional initialization stage. Researchers and engineers have been seeking an enhanced start-up operation to speed up the initialization stage. Recently, four patents related to geomechanical dilation were disclosed and claimed by three companies: Cenovus Energy, Bitcan Geoscience and Engineering, and Husky Energy (Davidson and Frederick, 2015).

2.1.1. SAGD Start-up Strategies

Prior to the innovation of horizontal drilling, the process of cyclic steam stimulation (CSS) with vertical wells had been the main option for heavy oil and bitumen recovery in Alberta. The communication between vertical wells was one of the main focuses for enhancing heavy oil and bitumen recovery. Forming an initial entry zone into the formation by means such as hydraulic fracturing and propping (Allen and Redford, 1975), was one of the proposed methods for establishing communication pathways in the viscous oil sands formations. This method could target the pre-existing high-permeability streaks within the formation It also involves the injection of high-pressure fluids to create an initial entry zone into the formation by means of hydraulic fracturing (Allen and Redford, 1975).

When the conceptual SAGD process and the technology of drilling a horizontal well were anticipated and applied in industry, Butler and Stephens proposed and disclosed a practical process (Butler and Stephens, 1981), which employed either injecting steam at pressures above the fracture pressure or hydraulically fracturing to establish thermal communication between the wells via vertical fracturing. This practise was particularly popular in the early era of SAGD technology. One of the major concerns on this type of enhanced technology is the high-pressure injection,

where fractures might be induced. Once full SAGD commences, the steam injection will easily leak through the fracture and take a short-cut channel back to the surface. Additionally, a high injection pressure can greatly increase the risk of fluid leak-off through the caprock, enabling fluids to travel to the surface, or travel below the reservoir and connect to other formations with bottom water or top gas/water. Therefore, the injection operating pressure is expected to be maintained below the maximum principal stress of the local reservoir.

Edmunds and Gittins developed an alternative scheme, which has since become the most widely-adopted start-up operation strategy (Edmunds and Gittins, 1991). Steam is circulated separately for some time through each of the wells to heat the oil sands near the wellbore in the formation. Thermal and fluid communication is established between the two wells. Circulation is conducted by injecting steam or hot water through the inside of the tubing and returning through the annulus at a pressure below the fracture pressure. The technology of start-up operation through steam circulation was firstly proposed and carried out in Phase A of the UTF project (Edmunds and Gittins, 1991). A combination of conduction heating followed by mild steam flooding was implemented by circulating steam in both wells with a pressure differential (at the wellheads) of about 350 kPa (Edmunds and Gittins, 1991). Once communication was established, steam circulation in the producer was discontinued and the fluids were produced through the tubing.

Steam injection strategy is another option to speed up start-up operations. In the early era of the SAGD process, a well is designed with one single tubing for each injector and producer. To deliver relatively uniform steam along the length of a well, dual or multiple tubing strings are designed. In some SAGD projects (Li *et al.*, 2011) steam is injected from the wellhead, through long tubing (LT) and short tubing (ST), down to the toe, and fluids are pumped back from the heel of the horizontal section to the surface.

No pressure differential between the well pair is required for start-up. When thermal conduction via steam circulation has heated the bitumen to a temperature between

50˚C and 100˚C, the bitumen is sufficiently mobile so that it can be displaced by hot water, followed by rapid convective heating. Under these conditions, and a small ΔP, steam breakthrough to the producer will take only a few days.

Aiming to a specific formation, such as with high permeability above the injector but low permeability between the wells, Mukherjee et al. proposed a so-called laboured start-up of production (Mukherjee *et al.*, 1995). This situation allows the development of the steam chamber but chokes off fluid transport to the producer and impedes the attainment of steam temperature in the zone around the producer. A similar effect could occur during steam circulation to initiate communication. Increasing the ΔP can increase fluid transport and convection; however, this solution is not applicable once breakthrough has occurred anywhere along with the well pair. Mukherjee et al. suggest that hot water injection could provide a better solution. The water will flow downwards, under gravity, from the injector to producer more easily than water and bitumen resulting in a faster rate of heat transfer and communication.

Besides hot water and steam as options for energy resources, electrical power and another type of solvent are also considered field applications.

Yuan et al. proposed a new method that uses electrical heating in the start-up SAGD operation and patented the wet electric heating (WEH) process (US patent 6,631,761) (Yuan *et al.*, 2004) in the USA. The reservoir is designed to be heated directly via Ohmic heating through the electric conductivity of the reservoir. The delivery of thermal energy by WEH was instantaneous. A series of lab-scale tests were conducted to validate this conceptual strategy for potential applications to SAGD/VAPEX initialization.

Solvent soaking is another option to enhance fluid communication between the inter-wells. Morris proposed a method of steam initialization to accelerate the establishment of fluid communication between horizontal wells (Morris, 2011). A modest amount of solvent is injected into a subject well which has very limited fluid mobility. A specific solvent, xylene, is used, and sub-fracturing pressures are

applied. The solvent is used to soak the oil sands in the formation around the wellbores and helps to reduce the viscosity of the bitumen.

Numerical simulation is also employed for analyzing and optimizing the circulation process. Yuan and McFarlane reviewed various techniques for start-up procedures in SAGD processes (Yuan and McFarlane, 2011). Simulation analysis indicates that, for a given set of tubing and liner sizes and reservoir properties, relatively lower circulation rates at high steam quality are more favourable for faster initialization and development of uniform temperature between the horizontal well pair. On the other hand, the use of high-quality steam in combination with high circulation rates may lead to slower initialization, with less uniform heating along the length of the wells, and with the possibility of the premature steam breakthrough at the heel. A small pressure difference between the well pair, offsetting the natural hydraulic pressure (50 kPa), appears to be more favourable for faster and more uniform initialization.

2.1.2. Enhanced SAGD Start-up Schemes

An enhanced SAGD start-up operation strategy is desired and required for SAGD operation to shorten the time. An effective and efficient start-up operation is crucial to enhance SAGD operation performance in terms of achieving good wellbore temperature conformance and rapid production ramp-up. It has long been a focus to seek such effective and economic means to enhance SAGD start-up operation. Various methods have been developed in the last decades.

In a traditional SAGD start-up using steam circulation, steam is injected into a well to the toe and fluids are produced back to surface at the heel. Anderson and Kennedy proposed a bull-heading start-up (Anderson and Kennedy, 2012), where the returning fluids are not produced and all the injected steam is forced to leak off into the reservoir. By avoiding fluid production, bull-heading offers significant advantages over traditional circulation schemes in terms of thermal efficiency, steam demand, operational simplicity and facility requirements.

Abbate et al. disclosed two inventions (Abbate *et al.*, 2013, 2014) and presented a method of establishing fluid communication between a well pair in an oil-sand reservoir by dilation with steam or water circulation at elevated pressures. Steam or water is circulated within at least one well at increasing pressure to a dilation pressure, which is sufficiently high to dilate the oil sands in the near-wellbore regions. The key technical concept is to create a dilation zone in the inter-well region by circulating steam or water at a bottom-hole pressure above the in-situ minimum principal stress. The bottom-hole pressure increases slowly in stepped increments at a low rate of 10 - 1000 kPa per hour to avoid fracturing or localized dilation and to gradually approach the breakdown pressure. The patents disclose that a sharp drop in bottom-hole pressure or a reduction in the produced steam from the same well may indicate formation breakdown and the onset of dilation. The concept also includes the maintenance of steam injection at a substantial and steady rate. The rates of steam or water injection and production may be monitored and adjusted, and the bottom-hole pressure may be controlled by adjusting the rate of steam-water injection or production.

A similar method to generate a dilation zone between a SAGD well pair was disclosed in a U.S. patent (Yuan, 2014). The method consists of several steps: conditioning wells, injecting a stimulant at pressures greater than the in-situ minimum stress of the formation, continuing stimulant injection into one of two wells while maintaining a target pressure at another well to propagate the dilation zone homogenously along the well length.

Prior to initiating geomechanical dilation through the injection of pressured fluids in oil sands formation, it is critical to gather information related to the characteristics of the formations of interest. The fact is some zones of the formation along an entire length of a wellbore might not require enhancement, as their initial porosities are high, or their initial bitumen saturations are very low. It is uneconomical to inject fluids in such regions. Davidson and Frederick proposed a pre-stimulation information gathering method (Davidson, Frederick and Meling, 2015) to determine the porosities and geology over several discrete intervals along

the length of the wellbore. Fluid penetration within each interval is inferred from the characteristics of fluid pressurization through the packer elements and tools at the surface or downhole.

2.1.3. Cyclic Injection Pulsing

Considering the elastic and plastic nature of oil sands, geotechnical responses including changes in volume, porosity and permeability might occur due to fluid injection and heating in an oil sands reservoir. These responses could be either elastic ones, which are temporary and recoverable, or plastic ones that are permanent and irrecoverable, or a combination of both as well. These elastic and plastic responses arise due to the expansion and contraction of the geomaterials including oil sands, mud, shale, gas, water and bitumen. The effects of heating will not be considered and covered in this section as this is beyond the study's scope.

Kosar carried out a series of constrained compression tests and isotropic compression tests with Athabasca McMurray Formation oil sands and Athabasca Clearwater Formation oil sands (Kosar, 1989). The isotropic cyclic consolidation test results indicate that the volumetric strains in stress cycling vary along the same path after the initial loading. The repeatability of the results indicates the elastic behaviour of the oil sand in stress cycling.

In the recovery of heavy oil and oil sands, sufficient efforts have been made to apply cyclic injection with pulsing pressure to enhance production performance. Various methods have been developed for oil recovery, which ranges from maintaining reservoir pressure waterflooding to thermal-induced processes. Fluid injection with pressure pulse has been used in the conventional oil and gas extraction industry to increase well production yields. Muhamad et al. found that fluid injection with pulsing pressure could lead to a significant improvement in oil production (Muhamad *et al.*, 2012). In a set of lab-scale VAPEX experiments, pressure variations were applied by sudden release and reinjection of the solvent; the oil production rate was enhanced by 20~30% (Muhamad *et al.*, 2012). In this process, the high viscosity of the heavy oil was expected to be reduced and the oil

production was directly related to the transfer of solvent into the heavy oil, which was due to low diffusion of solvent. This study showed that more oil was produced through short pressure blips by introducing injection pressure change than that under the base case of constant solvent injection pressure. The short pressure blips were more beneficial for lower permeability models and higher viscosity oils.

Wang applied periodic or continuous excitation of a porous medium under constant external fluid pressure and a change in the internal pressure distribution was found (Wang *et al.*, 1998). The experimental results displayed enhancement of flow rate by as much as 90% even in the absence of compaction or fabric changes. When excitation was stopped, the enhanced flow rate decayed slowly to the previous steady-state flow rate. It can be noted that the effective stress decreased with increasing fluid pressure. The shear-induced volume changes led to a porosity increase, which can affect the oil flow rate during a recovery process. Synergistic internal effects associated with the phenomenon of porosity diffusion appeared to be responsible for the flow rate increase. It appeared that the increase in rate arose because of internal pressure changes caused by the excitation.

A series of numerical and experimental simulation results of a cyclic solvent injection process study (Ivory *et al.*, 2010) indicated that 50% of oil recovery was achieved after primary production and six injection cycles. Oil swelling was considered as one of the main mechanisms for oil recovery enhancement.

Injection tools were used to apply a pressure pulse to the subsurface in unconsolidated material and yielded increasing oil production (Morris, 2011). A series of lab and field applications in the oil and environmental sectors have been completed. They extensively demonstrated that during fluid injection with pulsing pressure, the liquids repeatedly flow into and out of the wellbore and pore throats, generating intense mixing and superior dispersion, stabilizing displacement fronts, suppressing fingering, and greatly increasing the contact area of a liquid with the porous media (Davidson and Spanos, 2004).

Fluid injection with a wide range of pulsing pressure leads to elastic responses. Temporary changes in volumetric strain occur and permeability varies due to the elastic perturbation. The elastic excitation causes a periodic and gentle perturbation. For the elastic perturbation, the geomaterials relax to the previous equilibrium state after the injection pressure drops back to the initial reservoir pressure. However, strong perturbations are expected to be generated during fluid injection. Some irreversible changes or plastic deformation in porous media could be generated and maintained to enhance fluid injectivity and flow. For the plastic portion, some residual and irreversible deformation might bring about permanent porosity or permeability changes.

2.2. Interaction Between Geomechanical Dilation and Multiphase Flow in Oil Sands Formations

The literature review reveals that many triaxial tests, such as triaxial compression and a radial extension, were conducted to simulate stress variation during the thermal recovery process. Although some triaxial experiments displayed very significant dilation in an oil sands core during injection, they may not fully represent the stress path and deformation that reservoirs undergo during the injection.

2.2.1. Geomechanical Dilation due to Fluid injection

The concept of geomechanical dilation through a fluid (water, steam, or solvent) injection has recently been proposed and deployed in SAGD pilot well pairs to enhance SAGD start-up (Abbate *et al.*, 2013, 2014; Lin *et al.*, 2016) in Canada and China. The dilation-based start-up operation involves interactions between geomechanical response and multiphase flow in porous media. Geomechanical dilation represents either the rearrangement of solid particles due to rotation or distortion of grains, or the transportation or physical movement in space under varying loading and stress conditions. When dilation occurs, the volumetric strain

increases and the pore space increases accordingly, providing more space for water to flow through the immobile bitumen.

Some previous work has attempted to improve bitumen recovery through geomechanical dilation. Git proposed a process (Git et al., 2002) by which the solvent was injected at a pressure above its bubble point. The pressure was sufficient to induce geomechanical formation dilation or pore fluid compression, allowing the solvent to mix with bitumen. On one hand, the viscosity of bitumen was reduced due to the solvent's impact, and on the other hand, the increasing pore space due to dilation occurring allowed more space for water and solvent to flow through the immobile bitumen. When the pore pressure dropped, solvent gas drove the immobile bitumen. Evidence of the solvent gas drive of bitumen from the reservoir was also found.

Yaich conducted a series of confined compression tests under both increasing and decreasing mean stress conditions (Yaich, 2008) and found a more pronounced increase of permeability for a core sample with fine grain during dilation in comparison with coarse grain.

Khan carried out a laboratory test to study deformation induced by dilatant shear failure in unconsolidated reservoirs under the stress paths of triaxial compression and radial extension at low confining stress (Khan, 2009; Khan, Olson and Holder, 2011). The absolute permeability, relative permeability to oil and water, and residual saturations were examined and assessed through a series of tests. The experimental results showed advantageous increases in absolute and relative permeability caused by localized shearing under dilatant volumetric strain conditions, although dilatant shear failure does not guarantee increased flow capacity for unconsolidated sands. Computerized Tomography (CT) scans of the deformed sand samples indicated localized shear deformation along with discrete, high porosity bands with radial symmetry. The porosity in the deformation bands was as much as 50% higher than the less deformed surrounding sand pack.

The triaxial experiments displayed significant dilation in the sands during injection (Yale, Mayer and Wang, 2010). This group studied field oil sands samples with interbedded mudstone under fluid injection. The triaxial tests were carried out at room temperature under reservoir boundary conditions with only modest levels of stress anisotropy (stress ratio of 1.1). An empirical function of volumetric strain with relative permeability was inferred. The findings suggested a portion of the increased water saturation is equal to the variation in volumetric strain.

2.2.2. Geomechanical Response and Multiphase Flow Behaviour Variation Due to Stress Change

Geomechanical dilation of oil sands formations leads to the growth of porosity and permeability. It is impacted by the initial stress condition, stress anisotropy, stress path, fluid injection, and geo-properties of oil sands. This mechanical deformation can affect the fluid flow in the dilated zone of the oil sands formation.

At in-situ reservoir conditions, bitumen is immobile at an extremely low temperature (~8˚C). Any stress change induced will result in a pore volume change, which changes in the water saturation in the formation. The effective permeability to water varies accordingly.

Various authors have conducted experimental investigations into the flow behaviours and geomechanical response under triaxial stress conditions for oil sands (Wong, Barr and Kry, 1993; Scott, Proskin and Adhikary, 1994; Touhidi-Baghini, 1998; Yaich, 2008; Khan, 2009; Yale *et al.*, 2010; Khan, Olson and Holder, 2011; Hamoud, 2012; Abdallah, Hamoud and Chalaturnyk, 2014). A promising result has been reported indicating that permeability is enhanced by shearing dilation. Dusseault conducted triaxial tests (Dusseault, 1977) at confining stress of 0.4 ~ 2.0 MPa and reported a strong correlation between permeability variation and volumetric strain changes during shearing failure. He claimed that high confining stress over 1.0 MPa cannot result in permeability enhancement, even with a significant increase in deviatoric stress that corresponds to a high degree of shearing dilation. Wong and Scott et al. studied the stress-strain response of Cold

Lake Clearwater Formation oil sands (Wong, Barr and Kry, 1993), (Scott, Proskin and Adhikary, 1994). Scott et al. observed a 10% increase and a 32% reduction in permeability upon shearing dilation under 1.0 MPa and 7.0 MPa of confining stress, respectively, in a series of triaxial tests on Cold Lake oil sands. Oldakowski and Touhidi-Baghini concluded that increasing the mean stress resulted in less volumetric strain and less permeability enhancement (Oldakowski, 1994; Touhidi-Baghini, 1998). Experimental results (Oldakowski, 1994) indicated that the magnitude of volume change at the failure point depended on the stress path. During the triaxial compression shear tests, the specimens contracted at the beginning and subsequently expanded at higher axial strains. At the end of testing, the specimen volume was larger than it had been initially.

Bruno studied the stress-induced permeability anisotropy, and the damage in sedimentary rock, and the underlying micromechanics. He summarized three mechanisms for permeability alteration due to the micro-cracking processes (Bruno, 1994) (Manchanda, Olson and Sharma, 2012).

1. Pore volume compression and reduction in mean pore throat radii leading to permeability reduction.
2. Preferential closure of existing micro-cracks and elongated pores.
3. Additional micro-cracking events due to local shear and tensile failure of the intergranular and intergranular bonds. This creates high conductivity flow channels hence increasing permeability.

Bulk volume and pore volume compressibility of Athabasca oil sands have been studied and measured either by confined compression in an oedometer or by isotropic compression in a triaxial cell. The important finding is that, under an isotropic cyclic stress condition, the oil sands behave elastically. Agar found that the relationship between effective confining stress and volumetric strain upon unloading and reloading in isotropic cyclic consolidation is repeatable (Agar, 1984). He carried out a series of constrained compression tests and isotropic

compression tests with Athabasca McMurray Formation oil sands and Athabasca Clearwater Formation oil sands.

The bulk compressibility (C_{bp}) of the oil sands core, the effect of effective-stress (σ') variations on the total bulk volume (V_b) of the oil sands specimen under the constant confining pressure (P_c), is expressed as follows.

$$C_{bp} = \frac{1}{V_b}\left(\frac{\partial V_b}{\partial \sigma'}\right)_{P_c} \quad \text{Eq. 2-1}$$

Pore compressibility (C_{pp})of sands core, the effect of pore pressure (P_p), variations on the total pore volume (V_p) in the oil sands specimen under the constant confining pressure (P_c), is expressed as follows. φ is the porosity of the sample.

$$C_{pp} = -\frac{1}{\varphi V_b}\left(\frac{\partial V_p}{\partial P_p}\right)_{P_c} \quad \text{Eq. 2-2}$$

The relative change of volume ($\frac{\Delta V}{V}$) due to the deformation of the material can be calculated by the relative change of length ($\frac{\Delta L}{L}$) and Poisson's ratio (v) as the following (Chalaturnyk, 1996).

$$\frac{\Delta V}{V} \approx (1 - 2v)\frac{\Delta L}{L} \quad \text{Eq. 2-3}$$

The change in absolute permeability (ΔK_a) can be defined in terms of volumetric strain ($\mathcal{E}_v$)and initial porosity (φ_o) (Chalaturnyk, 1996):

$$\Delta K_a = 31\frac{\mathcal{E}_v(1 - \varphi_o)}{1 + \mathcal{E}_v} \quad \text{Eq. 2-4}$$

Coccia and McCartney built a new thermo-hydro-mechanical true triaxial cell (Coccia and McCartney, 2012) used for the evaluation of the impact of stress-induced anisotropy on thermally induced volume changes in saturated soils. Principal stresses were applied to the sides of a cubical specimen independently using flexible bladders, while the pore water pressure and temperature were controlled at the top and bottom of the specimen using rigid plates with embedded heaters and fluid control ports. The deformations of the four faces of the specimen

in the x and y directions are monitored during the application of mechanical stresses and temperature changes using linearly variable differential transformers (LVDTs).

The changes in the physical properties of sandstone samples under several different temperatures were measured (Somerton, 1961). Increases in bulk volume were comparatively small, but the resultant changes in porosity and permeability were substantial. Porosities were increased by as much as 20 percent and permeability by over 60 percent, depending upon the maximum heating temperature. Brodsky et al.'s study indicated that permeability was affected mainly by thermal cracking and fluid-rock chemical reactions when the temperature was increased (Brodsky, Getting and Spetzler, 1985). The former increased flow; however, the latter produced a clogging effect due to precipitation of new phases.

Several noteworthy aspects regarding the constitutive behaviour of oil sands due to the rate of heating and load history were summarized as the following (Kosar, 1989):

1. All three specimens show a cumulative volume increase during heating.
2. The specimen which underwent stress cycling before heating shows the greatest thermal volume increase. The non-cycled specimens displayed approximately the same amount of thermal expansion (0.35%) at 225°C.

Automatic measurement and recording of volume changes were the most difficult to accomplish for the measurements required in compression tests on oil sands. Numerous methods have been tried, the earliest of which was probably using a mercury null displacement unit. With the increasing precision of a commercial syringe pump, it is more common to directly measure the volume change through a digital display panel on the pump.

Oldakowski inferred from the experimental results that the magnitude of the volume change at the moment of failure depends on the stress path leading to a

failure (Oldakowski, 1994). During the triaxial compression shear tests, the specimens contracted at the beginning and then, in most cases, expanded at higher axial strains. At the end of testing, specimen volume was larger than it had been initially. To explain this volumetric behaviour, it is convenient to refer to the concept of two components of stress states: mean principal effective stress and deviatoric stress.

The permeability of an oil sands core can be measured by applying either a liquid or a gas flow through the core. Darcy's law is used and either a constant flow rate or pressure is maintained during operation. Touhidi-Baghini proposed an empirical relationship relating to permeability changes to volumetric strain (Touhidi-Baghini, 1998). Hamza investigated the SAGD process using samples constructed from loose Athabasca sand (Hamza, 2012). The results indicated that permeability changes (absolute and relative) and endpoint oil and water saturation variation were a function of loading boundary conditions. Triaxial loading paths (increasing mean stress) showed increased permeability with sample dilatancy upon failure at low confining stress (100 to 400 psi), which diminished when running at higher confining stress (800 psi). Residual oil saturation increases during compaction and decreased during dilation while initial water saturation decreased during compaction and increases during dilation.

2.3. Field Application of Dilation-Based Start-Up

Cenovus and PetroChina Xinjiang deployed the dilation start-up technique in their field SAGD projects. This is to revisit the field practices to examine the geomechanical impacts on SAGD dilation start-up performance.

2.3.1. Cenovus - Christina Lake SAGD Project

Christina Lake SAGD project is one of Cenovus' two major producing oil sands projects located approximately 150 kilometres southeast of Fort McMurray. It has operated for more than 15 years since initial production in 2002. Cenovus currently has five producing phases (A-E) at Christina Lake; this project is one of the most efficient in the industry. The average steam to oil ratio (SOR) was lower than 2.0.

The Christina Lake SAGD project yielded an average daily production of 150,000 gross barrels of oil per day in 2015.

Cenovus piloted the enhanced start-up strategy on some SAGD pads in the Christina Lake SAGD project in 2010 to shorten start-up time. It was expected to create a high-porosity dilation zone between the SAGD injection and production wells via controlled high-pressure injection.

Field operation began with steam circulation followed by the bottom-hole pressure slowly increasing to formation breakdown pressure. Continuous hot-fluid injection into both wells promoted dilation along the well pair length. After steam dilation completed, it took approximately 30 days of steam injection to achieve thermal communication in the inter-well region. Then, the dual well pair converted to the ramp-up mode of operation.

A steam dilation procedure started with preconditioning and increased injection pressure. In general, a reservoir was preconditioned for about two weeks before steam dilation operation began. Based on Cenovus's experience in Christina Lake, the duration of preconditioning using steam dilation was longer than using water dilation to allow the reservoir to be heated as well as pressurized.

Since 2010, when the first steam dilation was applied in the pilot well and the first water dilation was applied in pilot well, the enhanced dilation start-up technique has been used on more than 18 well pairs in the Christina Lake project.

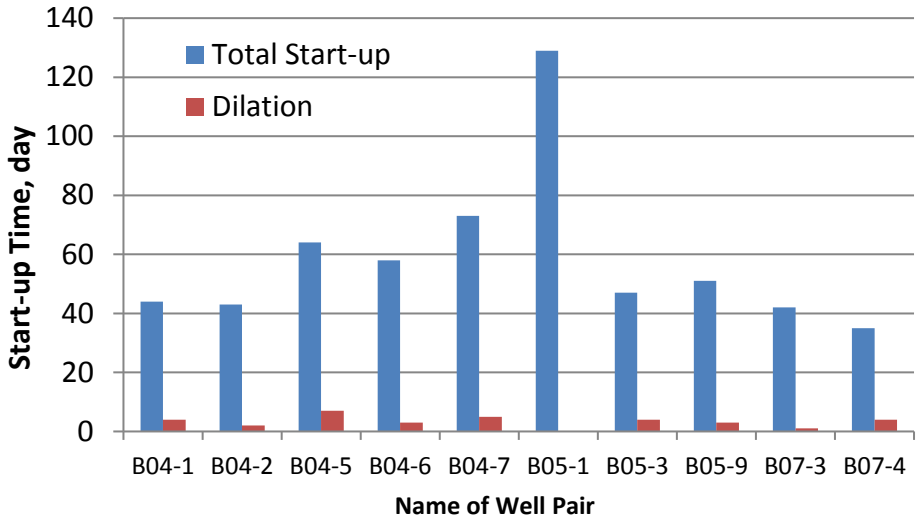

Figure 2-1. Start-up days in ten well pairs after dilation start-up in the Christina Lake SAGD project (Cenovus, 2014)

Start-up days of ten well pairs in Phase C in the Christina Lake SAGD project were collected and listed in It is clear that the communication time was greatly shortened to approximately 50 days, as compared to the 10 to 12 months typically associated with conventional circulation start-up procedures; approximately 5 days of the entire period were taken to carry out the dilation operation. In the Alberta Energy Regulator (AER) Report (Cenovus, 2014), it was indicated that communication between the inter-well pair can be achieved in less than 3 weeks in cases with superior reservoir quality using the dilation start-up method.

2.3.2. Xinjiang, PetroChina SAGD Project

PetroChina's Xinjiang Oilfield is located in northwest China and is the sixth-largest oil producer in China. Compared to the marine deposit type of oil sands reservoirs in Alberta, an oil sands reservoir in Xinjiang presents a continent deposit type with features of even higher viscosity, lower porosity, and permeability.

Based on Lin et al.'s conference papers (Lin *et al.*, 2016; Fan *et al.*, 2017), the average reservoir depth is about 300 meters under the ground, and the average

reservoir thickness is 35 meters. Initial oil viscosity is up to 10,000,000 cP while porosity ranges from 25% to 28%. Initial oil saturation varies from 65% to 75%, and absolute permeability ranges from 500 mD to 700 mD. The first SAGD pilot well pair started in 2009. The reservoir in Xinjiang has high heterogeneity with poor quality and presents a big challenge for a thermal recovery process; steam circulation time takes up to one full year. The horizontal well pair length is limited to around 400 m due to the steam conformance issue.

PetroChina Xinjiang Oilfield collaborated with the Bitcan company to exploit oil sands reservoirs by employing geomechanical dilation start-up, which was intended to shorten SAGD circulation time in 2013.

A similar dilation start-up technology which was applied in the Christina Lake SAGD project, FUSE^{TM} (Lin *et al.*, 2016; Fan *et al.*, 2017), was tested in Xinjiang oil sands reservoir. The first step was to achieve hydraulic communication between the injection and projection wells. After both wells were preconditioned at a certain level of pressure through fluid injection, the production well was then shut-in. The fluid was injected into the injector well with a controlled rate at an elevated pressure pattern to establish hydraulic communication. The hydraulic communication between a well pair was detected by a pressure change of the bottom hole. When a pressure increase was observed at the producer, it reflected fluid flow from the injector. The second step was to build thermal communication by injecting hot fluid through the injector, which was verified through monitoring the temperature response of 10 thermo-couples located along the horizontal section of the producer. A temperature increase of the entire thermal couples indicated full thermal conformance along the horizontal well. Dilation start-up operation ended once the inter-well communication was determined as described above. Then, the third step was to switch and turn over to steam circulation. To transfer more convection heat into the reservoir, high injection pressure was applied during the following circulation period.

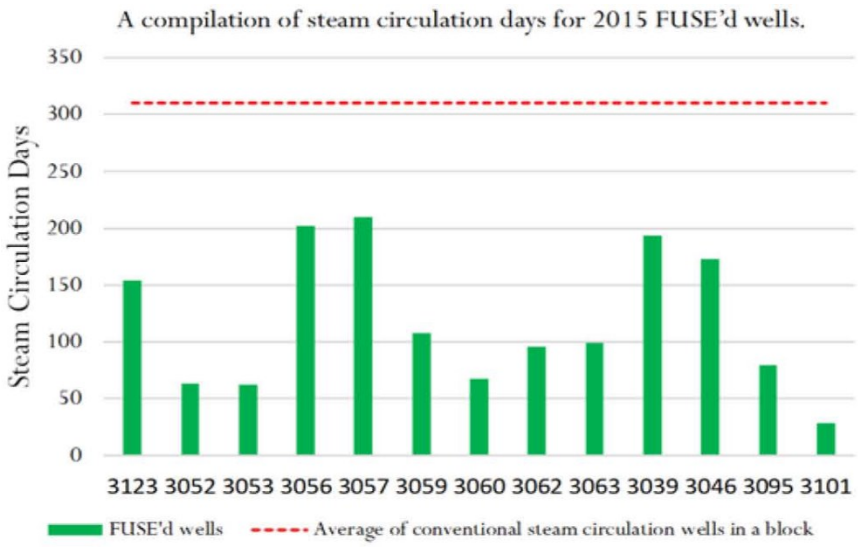

Figure 2-2. Steam circulation days in 13 SAGD start-up wells after dilation start-up in Xinjiang in 2013 (Fan *et al.*, 2017)

Since the first dilation start-up process was applied in Xinjiang in 2013 (Fan *et al.*, 2017), it has been expanded to include all SAGD wells in 2015. The time required for steam circulation (days) in thirteen SAGD start-up well pairs were collected and listed in Figure 2-2. With this dilation technology, the start-up time shortened to around three months in the Xinjiang oilfield, compared with approximately 12 months for average conventional start-up time.

2.4. Assessment of Dilation-Based Start-Up on SAGD Performance

Numerical simulation is often utilized to study the coupling of geomechanical and flow processes during SAGD performance (Chalaturnyk and Scott, 1997), (Li and Chalaturnyk, 2005), (Tran, Nghiem and Buchanan, 2009), (Warpinski *et al.*, 2012), (Khajeh, Chalaturnyk and Boisvert, 2011), (Pang *et al.*, 2015), and (Nassir and Walters, 2018). These approaches couple the stress-strain behaviour to multiphase flow using porosity, fluid saturation, and relative permeability as the coupling parameters. The geomechanics simulator and the reservoir simulator are used in a staggered manner. Pore pressure and temperature changes are calculated from the reservoir simulator and transferred to the geomechanics simulator where the stress and the displacement changes are then calculated in the geomechanics simulation. The literature review indicates that most of these coupled reservoir geomechanical simulations examined the full SAGD stage but did not model the dilation-based start-up. In comparison, this simulation study will examine the early phase through dilation start-up operation by water injection and focus on the impacts of such dilation on full SAGD performance in terms of bitumen production rate.

Xie and Shao studied the elastoplastic deformation of porous chalk (Xie and Shao, 2006). Two plastic deformation mechanisms were considered: plastic pore collapse and plastic shearing. The plastic pore collapse process is an important phenomenon of porous chalks and a new elastoplastic model was proposed, considering the two plastic mechanisms in relation to the microstructure of porous chalks.

There is a need to develop more general constitutive models where are able to describe the various features of oil sands including dilation and deformation. Based on the adaptation of classic elastoplastic models used in soil mechanics, an elastoplastic model of oil sands is expected to be developed and proposed. Two basic plastic flow mechanisms include plastic shearing of the solid matrix and volumetric dilation. The physical mechanism of volumetric dilation is related to the microstructure of material (Xie and Shao, 2006). In granular material, the

volumetric dilation may be generated by the rearrangement of grains increasing pore space. In porous cohesive materials like oil sands, the volumetric dilation generally results in inelastic pore collapse by breaking contact forces between grains. Depending on oil sands and loading conditions, one or more plastic mechanisms may be privileged in constitutive modelling. For modelling of two plastic flow mechanisms in geological materials, the classic method is to combine two yield surfaces, a cap surface for plastic consolidation and a cone surface for plastic shearing.

2.5.Summary

Steam or hot water circulation is one of conventional SAGD start-up strategies to establish communication in the transition formation. Either steam or hot water is pumped into both the injection well and the production well to heat up the oil sands in the inter-well areas. Hot fluids circulate across the full horizontal length of both the injection and the production well and heat up the wellbores. The heat is then transferred to the oil sands in the formation near the wellbore by means of thermal conduction. The bitumen in the transition zone between the two wells is gradually warmed up and the communication between the top and the bottom is established. Usually, this conventional steam circulation start-up operation takes a few months to achieve communication between wells. To improve the efficiency of steam to heat up the formation; researchers and engineers have been making efforts in searching for a better method.

This enhanced SAGD (Steam-Assisted Gravity Drainage) start-up scheme (Abbate *et al.*, 2013) has recently been deployed in a pilot SAGD well pad to shorten SAGD start-up operation time. The accelerated start-up scheme is related to pore pressure injection, which is expected to create a dilation zone vertically connecting two horizontal wells. This dilation zone is expected to increase porosity, permeability, and water mobility in the inter-well region. There have been several publications on permeability variation associated with shear-induced in unconsolidated sands

through a series of triaxial tests (Wong, Barr and Kry, 1993; Oldakowski, 1994; Scott, Proskin and Adhikary, 1994; Touhidi-Baghini, 1998; Yaich, 2008; Khan, 2009; Yale, Mayer and Wang, 2010; Khan, Olson and Holder, 2011; Hamoud, 2012; Abdallah, Hamoud and Chalaturnyk, 2014).

Most of these triaxial tests are conducted with the following stress path: maintaining confining stress while increasing axial or vertical stress to induce shearing failure. In general, such tests were designed and intended to simulate the stress variation, such as triaxial compression and a radial extension, during the thermal recovery process. Although some triaxial experiments displayed very significant dilation in the sands core during injection, they may not fully represent the stress path and deformation that reservoirs undergo during the injection. Yale studied field oil sands samples with the stress path under fluid injection (Yale, Mayer and Wang, 2010). Modest levels of stress anisotropy (stress ratio 1.1) were studied in his research. However, there are other scenarios of stress anisotropy.

While some geomechanical responses such as volumetric changes associated with in-situ bitumen extraction operations are recognized under different levels of stress anisotropy, it is still unclear how volumetric changes correlate with pore pressure increase under in-situ reservoir conditions in terms of pore pressure, stress state, and reservoir temperature.

Laboratory experiments and field practices have not been sufficiently comprehensive defining the petrophysical conditions under which dilation enhancement is the most effective and feasible for field operations.

Most of the progress in production technologies are based on empirical discoveries in the past; they were only recently followed by attempts to build a physical model and develop a theory to explain, analyze, and predict field behaviour. The SAGD start-up process through fluid injection dilation is a good example that achieved some success for bitumen recovery. It involves thermal expansion, viscosity reduction, and fluid compaction in a reservoir. The geomechanical response also plays a critical role in this enhancement process.

Based on the strength theories of geomaterials, it is not necessary to operate at high injection pressures exceeding the maximum principal stress to achieve geomechanical dilation. Plastic geomechanical dilation occurs if the deviatoric stress reaches the yielding points. Such geomechanical dilation is expected to greatly increase porosity and enhance fluid injectivity in the dilated zone, while the operating pressure is maintained below the principal stress. Two immediate potential advantages of this operational approach include the following: (1) a relatively low injection pressure is required for enhancing fluid injectivity, and (2) porosity could be greatly increased, which might yield the effective permeability enhancement as well.

CHAPTER 3. METHODOLOGY OF THE RESEARCH, EXPERIMENTAL DESIGN OF GEOMECHANICAL DILATION AND PREPARATION OF TESTING CORE

3.1.Methodology of The Research

The research methodology consists of laboratory testing and numerical model development. To achieve the research objectives, the study will carry out the tasks identified in this section.

3.1.1. Experimental Study

An oil sands core from McMurray Formation is crucial to lab-scale tests to obtain relevant characteristics of the geomaterials of interest. Considering the difficulties in extracting such a field core without disturbance, one option is to substitute a synthetic sand core for a field core. The synthetic specimen is prepared with clean dry sand obtained from the McMurray Formation.

3.1.1.1. Preparing Materials and Specimen for Lab Tests

To mimic the reservoir in-situ conditions, the testing material is well represented by targeting reservoir formation. Sands were initially extracted from tailings (provided by Syncrude Canada Ltd.), which were sourced from the McMurray Formation. The bitumen had been removed when the sample arrived at the university campus. It was representative of the oil sands in McMurray Formation.

The bitumen used for this study was obtained from the Mackay River SAGD project and possessed a high viscosity of 517,300 cP at 20˚C and 2,863,000 cP at 10˚C. A CT scanner was used to assess the fluid saturation along the length of the synthetic oil sands cores after the cores are saturated with bitumen.

Formation water is mimicked with 3% brine, which is used to flood the core during preparation.

3.1.1.2. Developing Lab Techniques to Densify Sand Packing

To conduct a set of comparison triaxial tests, all cores are prepared to the same dry density, wet density, and porosity or void ratio. Fluid saturation is well controlled to be homogenous and uniform along the core length. A specific packing technique is required to assure reliability and high quality.

a) b)

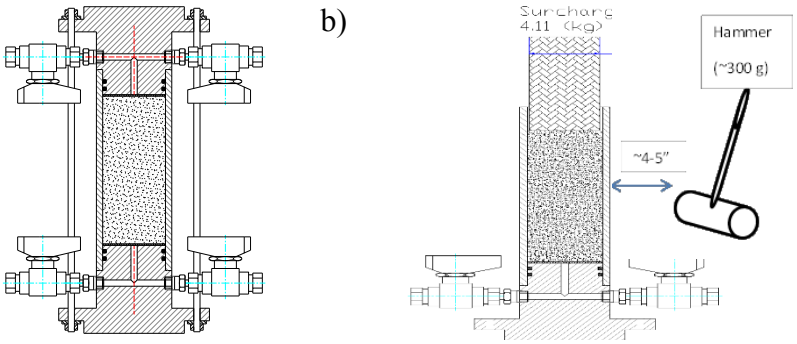

Figure 3-1. a) Image of core preparation apparatus assembly. b) Schematic diagram of sand packing using a hammer rather than a table vibrator.

During sand packing, sands are poured slowly and continuously into the steel cylinder shown in Figure 3-1. Extra weight is placed on the sand to apply a vertical load. The cylinder wall is tapped continuously at high amplitude and low frequency from the top to the bottom along the circumference of the packing cylinder cell.

3.1.1.3. Reconstituting a Core to Represent an Interesting Formation

The leak-free, sand packed model is evacuated and flooded with brackish water. The sands packing is flooded with brackish water under the vacuum conditions at a constant flow rate. Water is injected from the bottom to the top of the model using a cylindrical piston pump to maintain a uniform and smooth interface, which is shown in Figure 3-1**(a)**.

3.1.1.4. Triaxial Experimentation Design

A representative core, which is considered as an element between the injection well and the production well, is used to carry out a set of triaxial tests under conditions that mimic an in-situ reservoir in terms of pore fluids and pressure, temperature, and stress states.

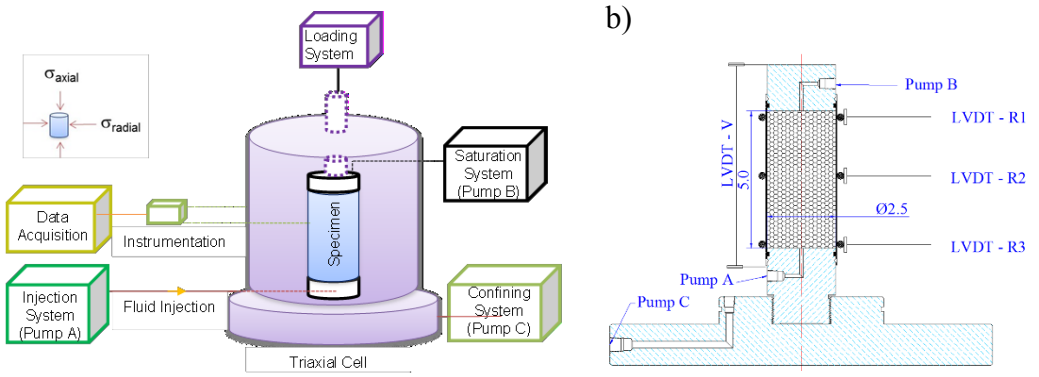

Figure 3-2 a) Schematic diagram of experimentation on dilation including loading frame, syringe pumps, data acquisition system, environmental chamber, and cooling system. b) Schematic diagram of instrumentation installed for the specimen in the triaxial test system.

Lab-scale experimentation is geomechanically engineered as shown in Error! Reference source not found. It consists of a confinement vessel, a test model, an axial loading system, an injection system, and an instrumentation and data acquisition system. Geomechanical dilation is initialized by fluid injection through the bottom of the core specimen. After the specimen is taken out of the test frame, it is either cut into slices or visually examined to describe the dilation.

3.1.1.5. Experimental Procedures and Stress Path

A synthetic specimen is tested in a triaxial cell and followed the multiple stress paths shown in Figure 3-3, which mimic in-situ reservoir temperature, pore pressure, and stress state. Tests are carried out under either isotropic stress or anisotropic stress conditions during the cold-water injection.

To simulate a deposit under isotropic stress conditions, the stress path of K_o=1 is applied, where the specimen is first consolidated and then injected with water under the isotropic state, shown as blue lines in Figure 3-3. The paths shown as red and green lines in Figure 3-3 indicate a core plug from a shallow deposit with an initial stress ratio (K_o) above 1.0, and one from a deep deposit with an initial stress ratio (K_o) less than 1, respectively. The specimen is anisotropically consolidated and then injected with water under anisotropic states until failure.

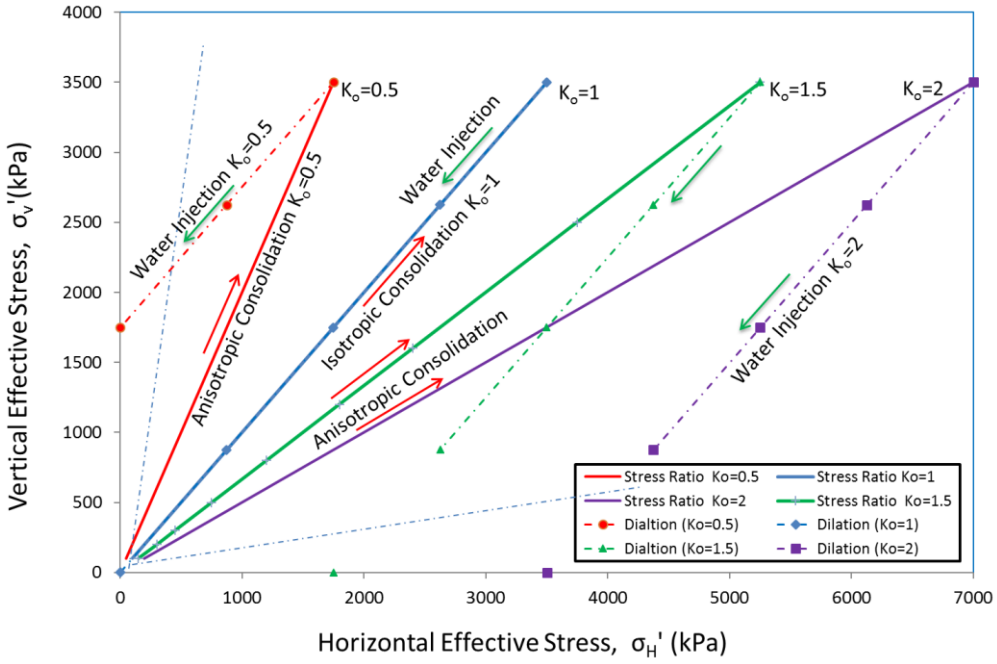

Figure 3-3. Stress path during cold-water injection

3.1.1.6. Boundary Conditions

Ten test runs were carried out to assess dilation mechanisms associated with four types of stress conditions, as shown in Figure 3-4. Tests #1, #2, #4, #6, and #7, which are framed with blue boxes, were carried out under an initial isotropic effective stress. Both horizontal effective stress and vertical effective stress were maintained at the same initial values during pore pressure injection.

Tests #3, #5, #8, #9 and #10, which are framed with red, purple, or green, were conducted for pore pressure injection under anisotropic stress conditions. The stress ratio was 0.5, 1.5, or 2.0, respectively, which is the ratio of the initial horizontal effective stress and the initial vertical effective stress.

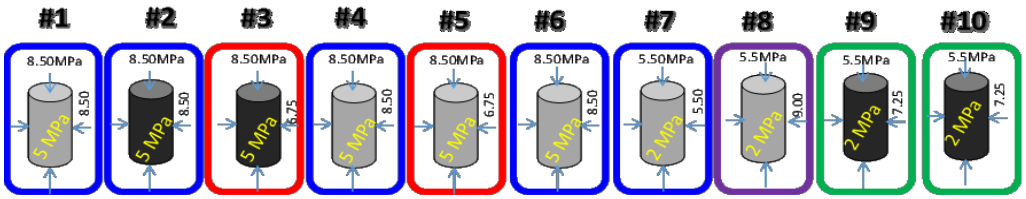

Figure 3-4. Parametric conditions of ten tests of dilation due to pore pressure injection (brine saturated specimens are GREY in colour and bitumen saturated ones BLACK in colour; tests under isotropic stress state with stress ratio K_o=1.0 are in a BLUE frame, ones under anisotropic stress state with stress ratio K_o=0.5 in a RED frame, with stress ratio K_o=1.5 in a GREEN frame, and with stress ratio K_o=2.0 in a PURPLE frame,).

3.1.2. Data Integration and Analysis Model

The geomechanical dilation and triaxial compression tests produced qualitative observations and quantitative measurements. Based on the triaxial tests conducted on oil-rich/free sand core materials, the experimental data were analyzed to investigate the injection strategy and operating conditions favouring dilation, and specifically the critical effective pressures where dramatic injectivity enhancement begins.

3.1.2.1. Examining Effective Permeability Variation under Initial Isotropic and Anisotropic Stresses

Under both initial isotropic and anisotropic stress states, the effective permeability to water on a bitumen-rich core and the absolute permeability on a bitumen-free sand core were assessed through the measured differential pressure and flow rate. The pore pressure increased due to injection at a very slow flow rate to ensure a low differential pressure across the length of the core specimen. The permeability

was measured at each stage with 100%, 75%, 50%, and 25% of the initial vertical effective stress until failure.

3.1.2.2. Volumetric Change during Cold-water Injection

To examine the effects of the initial stress state, oil sands cores were first tested under an initial isotropic stress state with a stress ratio of 1.0, and then again under the initial anisotropic stress state with a stress ratio of 0.5, 1.5, and 2.0. Volumetric change is based on the cumulative value of water injected and the axial strain can be read from the local LVDT sensors.

3.1.2.3. Failure Envelopes

The Mohr-Coulomb failure analysis for water-saturated sand was conducted and obtained through a set of compression tests under a drained condition. The stress-strain relationships are expressed at three elevated effective stresses of 500, 1500, and 3500 kPa, respectively.

3.1.2.4. Critical Injection Pressure to Enhance Fluid Injectivity in Oil Sands Formations

Given the initial stress state, reservoir pressure, and geomechanical behaviours of oil sands, it was possible to estimate a critical operating pressure, enabling the generation of a positive geomechanical response and the enhancement of water injectivity. The critical injection pressure, which is based on a semi-analytical model, is compared with the lab-scale tests.

3.1.3. Reservoir Geomechanical Modelling

Numerical models were established to evaluate operation strategies with dilation as a SAGD start-up strategy. One of two numerical modelling platforms is the geomechanical simulator FLAC3D, which is based on the finite difference method. The flow response during SAGD was simulated using CMG's STARS.

Based on constitutive equations supported by the laboratory results, a mechanical fluid coupled geomechanical model was developed using Itasca's FLAC3D to simulate the dilation start-up process and to compute the enhanced

porosity/permeability in the dilated zones. These parameters were subsequently provided as inputs to the flow simulation model using CMG's STARS for evaluating its impacts on the full-phase SAGD performance. The idea was to simulate the geomechanical response in terms of volumetric strain change during cold-water injection and to examine the conditions over which dilation may or may not affect near-well porosity/effective-permeability distribution in a permanent manner. The goal is to assess the potential impacts of the near-well dilated zone on SAGD recovery performance and to recommend the proactive utilization of a dilation-based start-up process for in-situ oil sands development.

3.1.3.1. Assumptions

The following assumptions are made to develop a numerical model:

1) Due to the extremely high viscosity of bitumen, the low in-situ temperature (10 °C) limits the bitumen mobility. Therefore, bitumen is assumed to be immobile and water is the only flowing phase in the porous media. The problem is simplified to a single-phase Darcy model.

2) Therefore, bitumen in porous media is considered part of the solids.

3) Temperature is kept constant throughout the water injection (i.e., isothermal conditions apply).

3.1.3.2. Geomechanical Constitutive Models and Flow Model

The modelling of the dilation start-up requires three distinct material constitutive models: wellbore, shale, and oil sands. The wellbore mechanical model is elastic, assuming isotropic flow conditions apply. The mechanical behaviours of shale and oil sands are modelled using a Strain Softening model; however, the shale is set to behave like a perfectly plastic material. Additionally, the oil sands are described by a stress-dependent Young's modulus model. An anisotropic flow model is used for both the shales and the oil sands.

The effective porosity of the core is defined as the volume of pores containing water divided by the bulk volume. The effective water porosity and the effective permeability during the cold-water injection were calculated. The effective permeability was examined through the triaxial cell tests.

3.1.3.3. Permeability Change due to Volumetric Strain/ Dilation

As sand is dilated in the reservoir and volume change occurs, the porosity changes, which leads to a change in permeability. Positive volumetric strain represents dilation and the negative volumetric strain shows compaction. The elastic response is similar to compaction or expansion of the material. On the other hand, the plastic response occurs due to the failure and the plastic behaviour of the material.

3.1.3.4. FLAC3D Verification

Two model types were used to verify the proposed geomechanical, fluid flow, and permeability update models inside of FLAC3D. A simple, single-cell model was used to test the mechanical model, the permeability update model, and the pore-pressure injection model. A seven-block stacked model was used to simulate fluid flow across several zones. In each model, the bottom was fixed, and boundary conditions were applied where required.

3.1.3.5. 2D Coupled Reservoir Geomechanical Model

A sequentially coupled reservoir geomechanical model was developed using the FLAC3D software to simulate the dilation start-up process. Caprock's integrity during the dilation start-up process is beyond the scope of this study.

Full SAGD performance may be affected by the cold-water dilation as well. Consequently, a model of the reservoir was built, and its performance due to geomechanical changes was studied through numerical modelling with codes such as FLAC3D, using an explicit coupling approach. Such modelling could address the question of how operating temperature may affect the full SAGD operation. It could also examine the influence of geomechanical effects at the reservoir level on the full cycle of the SAGD operation.

3.2. Experimental Design of Geomechanical Dilation

As described in Chapters 1 and 2, the concept of geomechanical dilation through fluid (water, steam, or solvent) injection is a relatively new operation strategy and has recently been proposed in the last couple years in Canada and China (Abbate *et al.*, 2013, 2014; Lin *et al.*, 2016). To increase understanding and verify the conceptual scheme and fundamentals of the dilation-based start-up operation, a set of lab-scale tests is required. The set of geomechanical dilation testing focused on the impact of the stress path on dilation in terms of the interactions between geomechanical response and multiple phase flow behaviours during water injection. The data generated from the triaxial test were used to calibrate the coupled reservoir geomechanical model which was then used to assess the impact of geomechanical dilation on overall SAGD performance.

3.2.1. Experimental Setting for Geomechanical Dilation

A set of lab-scale experiments were proposed in which multiple phase flow behaviours and geomechanical responses could be examined through the test. The set of tests included triaxial cell tests on core specimens, which were either bitumen-rich or bitumen-free.

The experimental model-simulated and represented a piece of oil sands between the injection well and the production well, which was well representative for an element in a typical McMurray formation with a porosity around 32 %, permeability to air around 0.5 Darcy, around half million centipoises of bitumen viscosity at 20 ˚C, and three million centipoises at 10˚C. Some in-situ reservoir conditions, including pore pressure and stress state in the Athabasca deposits, were employed in this research project to investigate the impacts of cold-water injection on the performance of a SAGD start-up operation,

A conventional triaxial cell was modified to satisfy the experimental objective. Figure 3-5 shows a schematic drawing of the fully automated triaxial-testing system used in the geomechanical-dilation tests. The testing apparatus included the

pressure vessel, the base, the top ram, and the confining fluids, which were chilled in a cold room before being transferred to a testing lab.

A conventional triaxial-test cell was used for confining stress. An environmental chamber housed the triaxial cell during the test, where the temperature was controlled with a thermal bath. A 400-kN high-precision load machine can apply a vertical load on the ram of the triaxial cell to generate vertical stress on a specimen. The axial loading rate can be varied from 0.00005 to 1016 mm/min with a position-measurement accuracy of 60.01mm or 0.05 % of displacement.

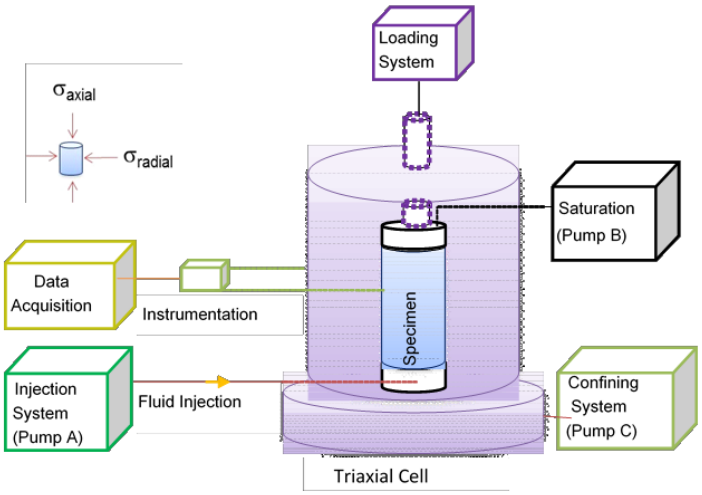

Figure 3-5. Schematic diagram of a triaxial test system for cold-water injection to generate and monitor geomechanical dilation

The confinement pressure was loaded through a silicon membrane, which isolated the core specimen from the confinement fluid. The ISCO pump was used to control the confinement pressure. The pore pressure was applied to the specimen through an opening on the top of the end cap, which was connected to the Quizix pump. During the test, the second Quizix pump was employed to control the injection or withdrawal pressure.

The core specimen was laid down on a porous stone, which sat on the base of the triaxial cell shown in Figure 3-6. Three pumps were used to control the confinement pressure, back pressure, and injection pressure, respectively. Three linear variable

differential transducers (LVDT) were mounted around the core specimen to monitor the radial strains and axial strains.

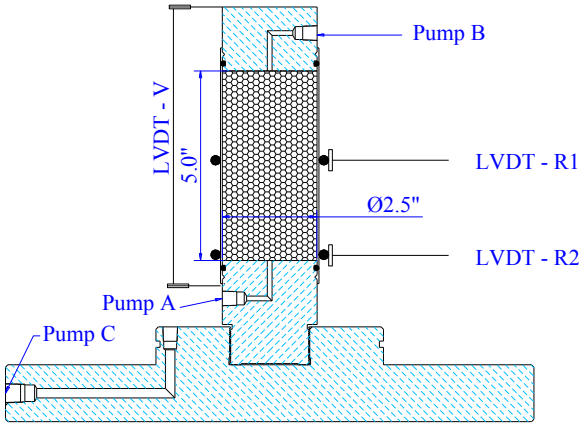

Figure 3-6. Schematic diagram of instrumentation (three LVDT) sensors connected to the triaxial test system: sensor LVDT-V for vertical distance, sensors LVDT-R for circumference change

Pressure transducers were installed to monitor pressure change during the experiment, including back (or pore) pressure, control confinement (or overburden, or cell), injection pressure, and differential pressure across the length of the core.

An environmental chamber housed the triaxial cell during the test, where the temperature was controlled with a thermal bath. A 400 kN of the Instron machine, which is shown in Figure 3-7, could apply a vertical load on the ram of the triaxial cell to generate vertical stress on a specimen.

Any test apparatus and instrumentation with high precision allow the measurement of tiny variation and response during the test. The University of Alberta Reservoir Geomechanics Research Group $[RG]^2$ Lab is equipped with the Instron model 5980 series as a loading frame to apply axial stress during a test. The loading rate can be varied from 0.00005 to 1016 mm/min with position measurement accuracy ±0.01 mm or 0.05% of displacement. The maximum load range of the frame is 400 kN. The triaxial cell was specially designed for high-pressure tests, which was made from high strength steel.

Two different types of pumps were employed during the set of the triaxial test: ISCO syringe pump and Quizix high-pressure series pump. The 260D syringe pump provides precise, predictable flow and pressure control at flow rates from 0.001 to 107 ml/min. Flow accuracy can reach ±0.5% of the setpoint, while the standard pressure accuracy holds 0.5% of full scale.

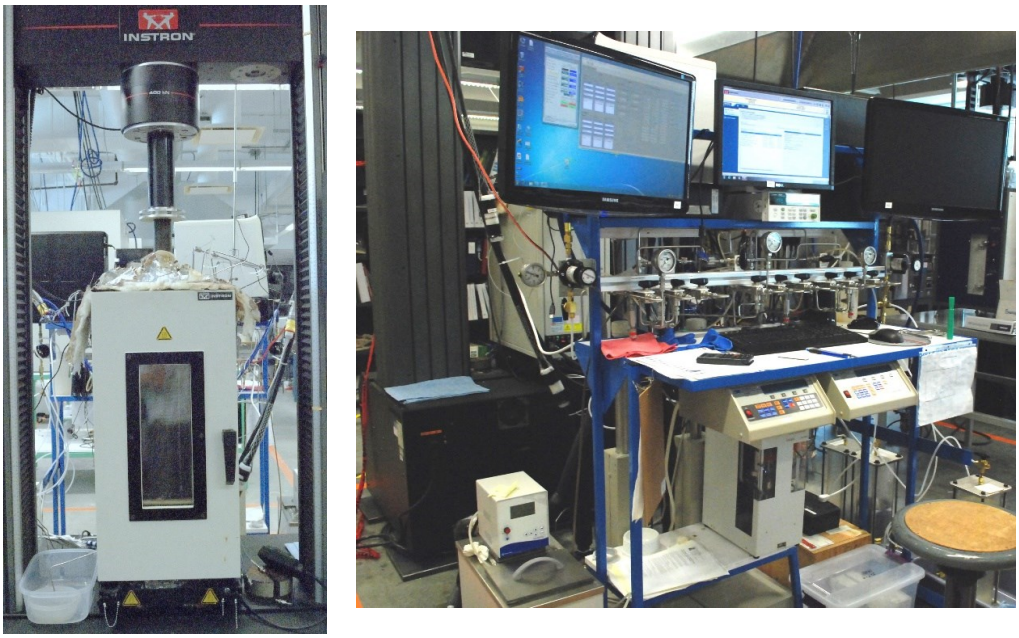

Figure 3-7. Left: Image of 400 kN Instron loading machine and environmental chamber; Right: Injection pumps, data acquisition, monitoring and controlling system

The procedure of automatic measurement and recording of volume change was the most challenging aspect of the setup. Numerous methods have been reported in the public domain, the earliest of which detailed the use of a mercury null-displacement unit. With the increasing precision of commercial positive-displacement (syringe) pumps, it is more common to directly measure the volume change using these pumps. This study used two types of syringe pumps to control confinement pressure, fluid injection, and withdrawal. Fluid-flow accuracy can reach 0.5 % of a set point, the standard pressure accuracy is 0.5 % of full scale, and a constant flow rate can be maintained as low as 0.001 cm^3/min. The volume injected through a

pump has a sufficiently high precision to identify and respond to the minute variation of pore pressure. This is to ensure that extremely low permeability (10^{-6}Darcys) can be measured properly across a 12.7 centimetres sample with the capacity of an extremely low flow rate. The differential pressure (DP) sensor cells must be chosen with an appropriate measurement range to obtain high-precision pressure-drop measurements.

To accurately measure DP across the specimen core, two types of DP transmitters were used. One pressure transducer was set with a high range of DP (0 to 2200 kPa), and another one was calibrated with a low range of DP (from –100 to 400 kPa) with the accuracy of 0.04 % span.

Permeability in the microdarcy range of a porous medium (sand specimen with 127 mm length) can be measured properly with the capacity of extremely low flow rate provided by the Quizix pump and an appropriate range of DP cell with high precision.

3.2.2. Stress Paths during Geomechanical Dilation

The effect of in-situ stresses on production is generally not considered in petroleum engineering. It is commonly assumed that the permeability and porosity remain constant or change very little during oil production in the reservoir lifetime. However, this assumption does not reflect the field reality and it is not true when considering the variation of in-situ stresses during the entire course of oil recovery. The local stress varies with the fluctuating pore pressure due to oil production, specifically in a thermal recovery process such as SAGD.

It is essential to address the effects of in-situ stresses on reservoir activities and obtain a better understanding of this issue. Athabasca oil sands are contained in unconsolidated sand reservoirs which are fluvial or tidal in origin and are deposited less than 600m from the surface (Yale, Mayer and Wang, 2010).

The stress path is identified by K, the relation between effective horizontal stress (σ_h') and effective vertical stresses (σ_v') as in the following expression: $K = \frac{\sigma_h'}{\sigma_v'}$.

Considering a depth of 200 to 250 meters combined with compressive horizontal stresses from the Rocky Mountains, the minimum principal stress vector is vertical, and the intermediate and the maximum principal stresses are horizontal. Then, at the depth of 250 meters or below, the stress ratio is greater than one: $K = \frac{\sigma_h'}{\sigma_v'} > 1$. At depths greater than 200 meters, but still less than 250 meters, one of the horizontal stress vectors is the lowest and the vertical stress is the maximum principal stress, where, all fractures are vertical. Then, at the depth of 250 meters or above, the stress ratio is less than one: $K = \frac{\sigma_h'}{\sigma_v'} < 1$.

Especially when combined with thermal stresses induced during steam injection processes the reservoir formation leads to horizontal fracturing during injection at depths down to 400- 500 meters in the southern part of the area to 300 ~ 400 meters in the northern part (Dusseault, 1977; Chhina *et al.*, 1987; Kry, 1990; Wong, Barr and Kry, 1993; Leung, Kry and Wong, 1995; Boonen *et al.*, 2005). The over-consolidated nature of the sands, combined with their angular nature and slight cementation in some sands, leads to a stiff matrix and a "locked" nature of the sands mechanically (Dusseault and Morgenstern, 1979).

A classic triaxial compression test in a lab follows the stress path: the increasing vertical stresses and the constant horizontal stress result in increasing mean stress as well as increasing differential stress. However, the geomechanical dilation test has a different stress path. The pore pressure increases in the reservoir and meanwhile reduces the effective vertical and horizontal stresses due to the fluid injection. This represents a path of decreasing mean stress. This stress path can be studied either by conducting radial extension experiments at constant axial stress in a triaxial apparatus or by increasing sample pore pressure under constant confining and axial boundary conditions.

Experimental tests were conducted to evaluate permeability variations and volumetric strains during pore pressure injection. A water-wet (brine saturated) or bitumen sand core was tested in a triaxial cell housed in an environmental chamber

to simulate reservoir boundary conditions in terms of stress state, temperature, and pore pressure. A specimen mounted in the triaxial cell was subjected to effective confining stress in the horizontal direction and effective axial stress generated by the Instron loading frame. A series of experiments were carried out following the stress paths are shown in Figure 3-8. The goal of the testing was to assess specimen behaviour under pore pressure injection for different initial isotropic and anisotropic stress conditions.

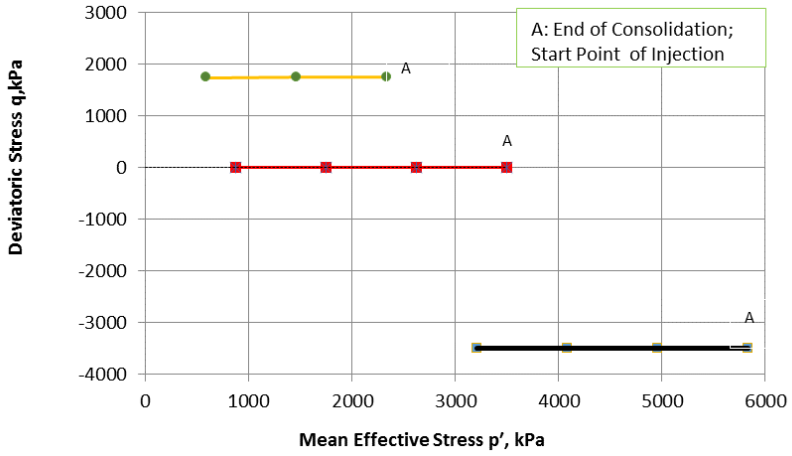

Figure 3-8. Schematic diagram of stress paths during water injection under different stress conditions

To simulate a formation under identical values of horizontal stress and vertical effective stress, the stress path of K_o=1 was applied, where the specimen was first isotropically consolidated (point A on the red line in Figure 3-8) and then injected with water under the initial isotropic state. For anisotropic stress states (e.g. shallow formations where the initial K_o >1, and deep formations K_o <1), the specimens must be anisotropically consolidated to the required stress state (point A on the black and orange lines in Figure 3-8) prior to beginning the pore pressure injection stress path.

After either isotropic or anisotropic consolidation, water injection started in the core specimen. Starting from point A (Figure 3-8), a constant deviatoric stress path was imposed with the mean stress reduced, while the deviatoric stress was kept constant under a different stress state. Figure 3-9 depicts three main stress paths followed

by a core specimen during water injection under either initial isotropic stress or initial anisotropic stress condition. A set of experimental parameters was applied to the testing apparatus, which physically simulated the in-situ reservoir conditions in terms of temperature, pore pressure, and stress. The testing temperature was set at 8~10 °C and the initial pore pressure was set to 2.0 MPa or 5.0 MPa. The initial horizontal and vertical stresses ranged from 5.5 MPa to 9.0 MPa.

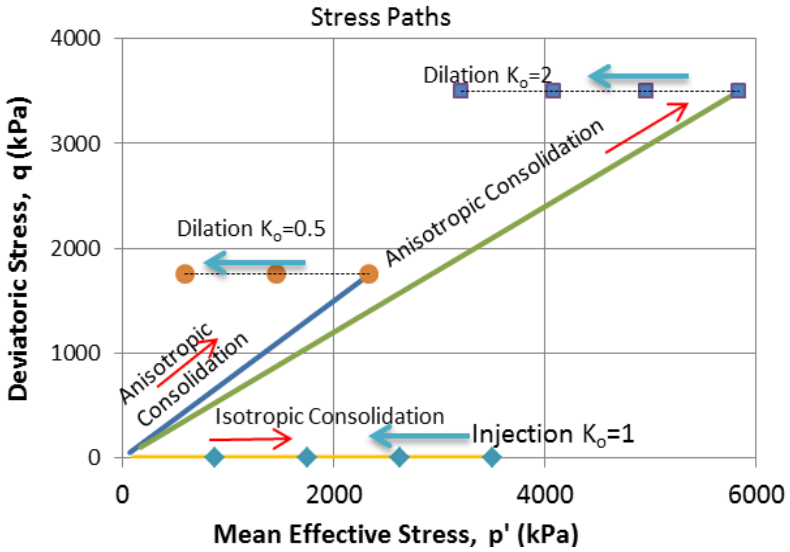

Figure 3-9. Schematic diagram of stress paths during water injection under different stress conditions

A pore pressure of 5.0 MPa, vertical stress of 5.1 MPa and a horizontal pressure of 5.1 MPa were applied to the sample, which was left overnight for thawing and re-saturation. After complete thawing and re-saturation, the core sample was consolidated in stages, with the effective stress of 50, 100, 200, 400, 800, 1600, and 3500 kPa. At the end of consolidation with the initial vertical effective stress of 3500 kPa, a permeability measurement was conducted.

3.2.3. Experimental Procedures for a Geomechanical Dilation Test

All prepared specimens were frozen to minimize core damage and were stored at -18 °C. Prior to beginning a test, the specimen was immersed in a container filled with dry ice to drop the specimen temperature to at least -40 °C prior to final trimming to approximately 12.7 cm length using a diamond saw. The surfaces of

both sample ends must be smooth and normal to the axis. The trimmed specimen was then returned to the dry ice to prepare the specimen for mounting in the testing cell.

This procedure could assure that the specimen will not thaw before it was set up in the triaxial cell and transferred to the environmental chamber. After it was covered with a silicone sleeve, the specimen was then placed on the base pedestal. Three LVDT sensors were mounted to monitor the radial strain around the middle and bottom sections of the specimen, as well as the vertical displacement during the pore pressure injection, respectively.

The core specimen was then consolidated either isotropically or anisotropically. Then, pore pressure injection was carried out through the Quizix pump at a very low flow rate (0.05 ~ 0.5 ml/hour) to assure a low differential pressure across the specimen. The lowest possible differential pressure across the core was achieved. A slow flow rate was intended to ensure the pore pressure increased at a similar rate across the length of the core. During the test, the vertical stress loaded by the Instron machine and the horizontal confining pressure were maintained at constant levels for all tests. The volume variation was measured and recorded through the Quizix pump.

An effective permeability to water on the bitumen-rich core and absolute permeability in the bitumen-free water-wet sand core was then computed from the DP and flow rate measurements.

The permeability was assessed at approximately 25%, 50%, 75% and 100% of the peak strength of the specimens. The differential pressure across the core was maintained below 10% of effective stress for the permeability measurement.

3.3. Characterization of Geomaterials Used in Lab-Scale Tests

The material characterization includes the grain size distribution (GSD) analysis, the specific gravity of sands, and the viscosity of bitumen used in the study. It also included the determination of specimen bulk and dry densities, bitumen and water saturation, and porosities. Additionally, the unit weights of solids and bitumen were measured and XRD mineralogy analyses for each facies were performed. The average specimen porosities were measured after isotropic consolidation at minimum in-situ principal stresses.

3.3.1. Treatment of Sands

Sands were initially extracted from the tailings sands by Syncrude Canada Ltd., which was sourced from the McMurray Formation oil sands formation. The bitumen had been removed when the sample arrived at the university campus. It was representative of McMurray Formation oil sands. After it was extracted by the Syncrude Canada Ltd. by means of open-pit mining, the bitumen was removed in a research laboratory. Although the detail process was unknown, solvents were involved in the recovery process as there was some black coke-like material found in the sample. Before the sands sample could be employed in the preparation of artificial oil sands cores, the coke-like material was removed.

The image in Figure 3-10 reflected the sands specimen before it was cleaned up. It can be noted that some soil particles were aggregated, which must be broken up. All the aggregations were manually squeezed to break into single pieces. Dean-Stark trap was used to remove any remaining bitumen from the tailing sands samples. The sands were then treated properly to retain their initial wettability. Although all of the coke-like was checked out though, the coarse sands were kept in and blended into the mixture to well represent the original components and ratios of grain with different sizes. Sands were then evenly dispensed into 18 portions shown in Figure 3-10, which could then be sampled for grain size distribution (GSD) analysis.

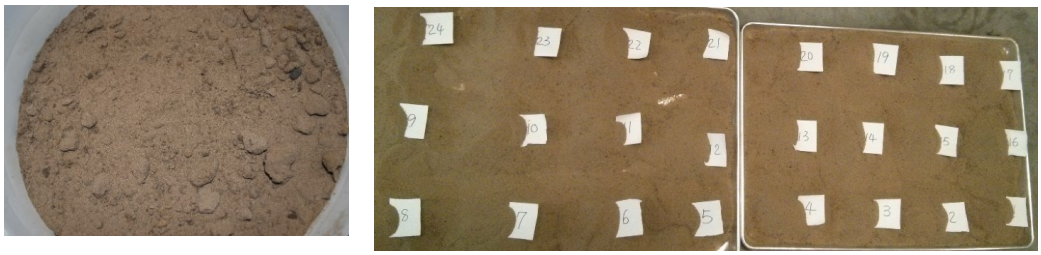

Figure 3-10. Left: a snapped image of dry sands; Right: sands were dispensed into 18 portions to be sampled for GSD analysis

3.3.2. Grain Size Distribution of Sands

The mechanical or sieve analysis was performed to determine the distribution of the percentage of different grain sizes contained within sands. This method was mainly employed for the coarser and larger-sized particles only, which constituted a high percentage of the batch pail. The hydrometer method, which was used to determine the distribution of the finer particles, was not necessarily due to the low percentage of the finer particles.

Before the sands were taken for size distribution analysis, the entire batch pail of the sand sample was well mixed in a big container. Then it was dispensed into 18 portions as shown in Figure 3-10 which were roughly even in mass. Six portions of the total set were taken from the tray for GSD analysis. Sands in each portion were then added in the stack of the sieve and allow them to pass through a set of sieves, which was comprised of No. 4, 10, 20, 40, 60, 80, 100, 120, 200, 325, and pan.

Figure 3-11. Left: a snapped image of weighing dry sands remaining in a sieve; Right: the image of sieve stack in a shaker machine

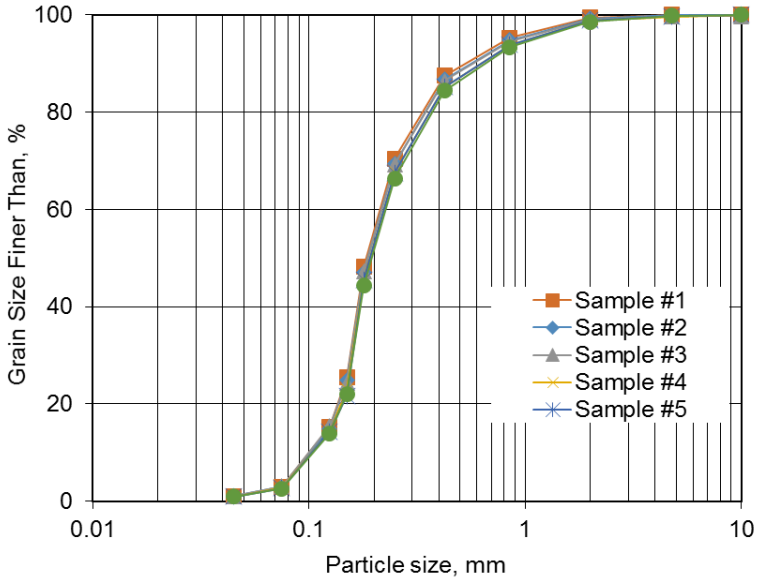

Figure 3-12. Grain size distribution of 5 sands samples

Based on the measured mass corresponding to each size opening, the percentage passing through an opening can be calculated. Figure 3-12 demonstrates the grain size distribution analysis results for five sands samples, which were randomly picked up from 18 portions. It can be noted that five GSD curves almost overlapped each other, which indicated that each sample had an almost identical grain-size distribution. Sands from each portion were well represented for the whole batch of sands. The sands were uniformly mixed and dispensed.

Combining the measured mass corresponding to each opening size with all sampling portions, the average percentage passing through an opening can be calculated, which is shown in the following **Error! Reference source not found.**.

Table 3-1 Grain size of sands used in the study

Sieve No.	Opening (mm)	Net Wt. (g)	Net Wt. (%)	Finer than (%)
0	10.00			100
4	4.75	32.86	0.25	99.75
10	2.00	109.20	0.82	98.94
20	0.85	647.80	4.84	94.09
40	0.425	1136.05	8.50	85.60
60	0.25	2350.28	17.58	68.02
80	0.18	2982.48	22.31	45.71
100	0.15	3074.08	22.99	22.72
120	0.125	1109.44	8.30	14.43
200	0.075	1553.86	11.62	2.80
325	0.045	245.96	1.84	0.96
Pan	---	128.94	0.96	0.00
Subtotal		13,371		

Based on **Error! Reference source not found.**, the mass percentage passing corresponding to particle size was determined, shown in Figure 3-13.

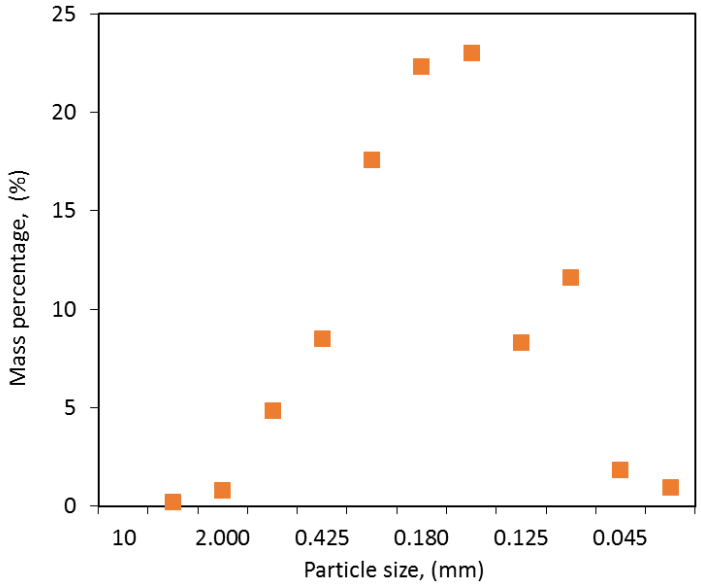

Figure 3-13. The mass percentage of sands corresponding to grain size

It indicated that the biggest percentage 22.99% in mass corresponded to the sands with a size of 0.25 mm, and the sands with a size between 0.18 mm and 0.25 mm took up around 45.5% in mass.

It can be noted that the mean size of this batch specimen was around 200 micrometres (μm). Sieve analyses in Figure 3-14 indicated a relatively large range of particle sizes and modest poorly-graded sands with an effective size D10 of 105 μm and an average grain size D50 of 200 μm.

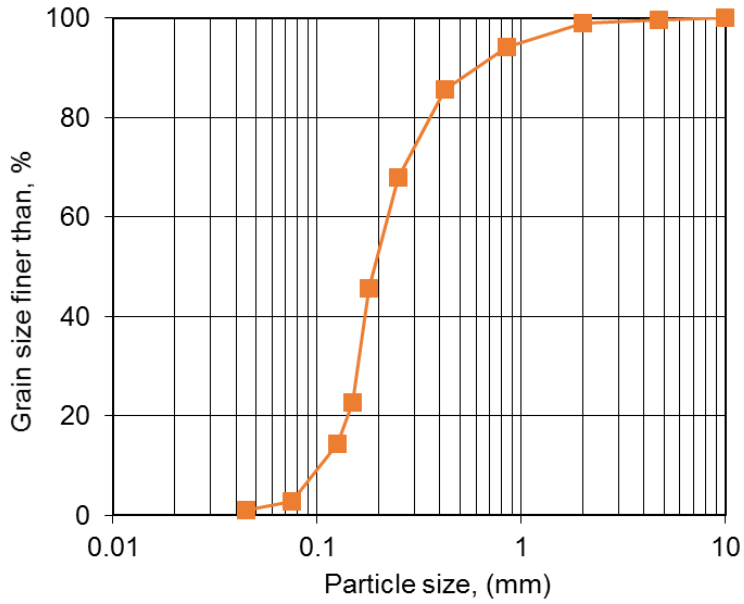

Figure 3-14. Grain size distribution of total sands used in the test

The general slope of the distribution curve can be described by means of the coefficient of uniformity ($\boldsymbol{C_U}$),

$$C_U = \frac{D_{60}}{D_{10}} = 2.2 \qquad \text{Eq. 3-1}$$

and the shape of the distribution curve can be described by the coefficient of curvature ($\boldsymbol{C_C}$),

$$C_C = \frac{{D_{30}}^2}{D_{60}D_{10}} = 1.0 \qquad \text{Eq. 3-2}$$

3.3.3. XRD Analysis

Mineralogy of sands used in this research was determined using x-ray diffraction (XRD). The XRD analysis result indicated that the sands samples consist mainly of quartz (silicon dioxide, SiO_2), which was 95 % in weight. It also contained 5 % of potassium feldspar, less than 1 % of kaolinite, and less than 1 % of muscovite.

Table 3-2 XRD Semi-quantitative results

Sample Name	Clay/Minerals	Weight (%)	Comments
Tailing Sands	Kaolinite	<1	trace
	Quartz	95	
	K-Feldspar	5	
	Muscovite	<1	trace

3.3.4. Specific Gravity of Sands

The specific gravity reflects the average density of a batch of the sample. To well represent the entire sample, the sands sample in the pail was mixed thoroughly and evenly. Two samples of 100 grams each were prepared and laid in an oven overnight to dry out completely before their properties were measured. Then the measuring procedure was followed up and two values were obtained.

The ambient room temperature was recorded at 23.3 (˚C), at which the density of water was assumed with 0.9975 (grams/ cm^3). By averaging these two values, the magnitude of specific gravity was determined to be 2.65.

3.3.5. Viscosity of Bitumen

The Athabasca field bitumen was selected to use in the set of triaxial tests. The viscosity curve is plotted in Figure 3-15, which was temperature dependent. The bitumen used for this study was obtained from the Mackay River SAGD project and possessed a high viscosity of 517,300 cP at 20 ˚C of room temperature and 2,863,000 cP at 10˚C.

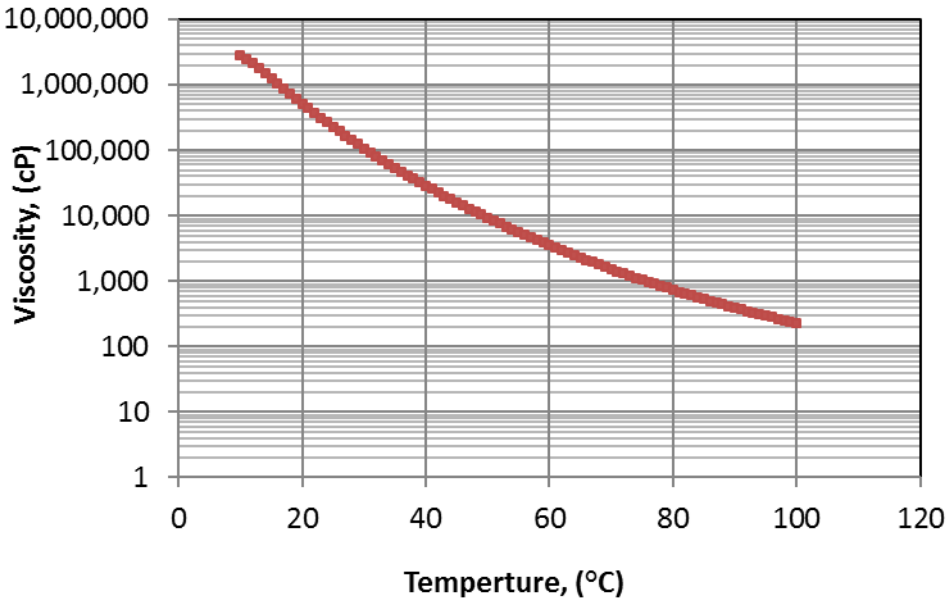

Figure 3-15. The viscosity of Mackay Lake SAGD project bitumen at the elevated temperature

3.4. Improved Technique to Obtain Identical Synthetic Core Specimen

Obtaining reliable geomechanical and petrophysical properties are key to evaluating the potential of a reservoir for deploying a new process. Considering the difficulties of obtaining a non-disturbed representative field specimen, the preparation of artificial oil sands samples provides an option to obtain the desired characteristic. A synthetic core specimen is commonly used in laboratory tests to obtain a geomechanical response and multiple phase behaviours in porous media through a triaxial test.

To simplify the effects of multiple mechanisms dominating the parameters, an artificial specimen is usually prepared under a consistent procedure, where the uniform distribution of grain size, density, fluid saturation, and porosity along the length of a core plug could be well controlled and retained. It is crucial to keep the

fluid saturation well distributed along the core length in the series of experiments related to geomechanical dilation.

To obtain the desired characteristics for the geomaterials in the reservoir formation, the testing specimen must be representative of this formation. The testing specimens used in the lab-scale triaxial tests must be as identical as possible in terms of the characterization and the structural matrix of the testing material for comparison and prediction. Specifically, the specimen is expected to have a high degree of homogeneity to allow identification of the main factor affecting the mechanism and mechanics.

A synthetic core specimen was assessed to determine its quality. Experimental techniques were developed to inspect and assess the sample quality in terms of void ratio, dry density, fluid saturation distribution and other petrophysics in the core.

3.4.1. Existing Techniques to Constitute Synthetic Oil-Sands Specimen

The preparation of an oil-sands specimen for testing oil sands to study the multiple phase flow behaviours and geomechanical responses through porous media models is of some general interest in Alberta. To provide fundamental data, researchers built and conducted a series of experimental tests on geomaterials. Reconstituted Athabasca samples have been used in some research studies (Dusseault, 1977), (Agar, 1984), (Ivory *et al.*, 1987), (Polikar *et al.*, 1988), (Oldakowski, 1994), (Touhidi-Baghini, 1998), and (Hamoud, 2012).

There are mainly four ways to prepare for a core specimen. The first one is to drill a section of the core with little or no least disturbance in the formation interested and then trim a specimen, which can well represent the specific formation. A big challenge is that the in-situ stress state will immediately change once the section core is extracted from the reservoir to the surface. The high degree of heterogeneity along the length of the core does not allow identifying the main factors affecting the geophysics and petrophysics. The second option is to reconstitute a core specimen using loose oil sands, which mixes them in a sample cylinder and then applies extra loads to compact them as tight as possible. The main issue with this

method is the possible trapping of air in the oil sand, which impacts fluid behaviours in a test related oil sands recovery process. Dusseault et al. used similar compaction techniques to prepare some remoulded oil sand samples (Dusseault, Soderberg and Sterne, 1984). The third one is to mix the wet sand and the desired bitumen sample. The dry sands must be first soaked with water, after which the excess water is removed in a centrifuge (Ivory *et al.*, 1987). The same issues as in the second preparation method mentioned previously may arise, where the trapped air in the oil sand is an extra phase besides water, oil, and solid. The last but the most commonly used way is to prepare a dry or wet sands core and then vacuum the core to remove air. Water or bitumen then is injected to flood the core sample.

In the early years, the packing preparation methods for sands core specimens applied similar techniques for lab compaction in soil engineering, where a vibrator is used to densify the packing (ASTM, 2003). Dusseault prepared samples by vibrating Ottawa sands (C-109) with a variable vibration amplitude control (Dusseault, 1977). The vibration was continuous throughout the sedimentation process. Conducted by gently striking the side of the mould with a wooden mallet, was used to complement the vibration. Bulk densities were calculated when the total dry weight was determined after testing.

The reproducible sand packing technique was then modified by the researchers at InnoTech Alberta. Ivory et al. produced cylindrical oil sand cores (Ivory *et al.*, 1987) by filling, tamping, and vibrating (banging) the sands mixture in a core holder that was made of a softened copper pipe. A tamper rod was used to tamp the sand bordering the core holder, rather than pressing against the cross-section during the sand packing. The banging in a helical pattern on the sleeve generated horizontal impacts to allow rearrangement of the sand grains, leading to a compact configuration. A relatively loose packing mainly resulted from insufficient stress from vertical direction except for the gravity of sand grains.

InnoTech Alberta provided with the facility to prepare synthetic sands specimens. Polikar constituted some core specimens and carried out relative permeability

measurement for his Ph.D. degree research (Polikar *et al.*, 1988). A pneumatic vibrator was used during the sand packing procedure in a transparent Lucite tube.

Touhidi-Baghini continued to use the vibratory table to prepare synthetic specimens at the University of Alberta. He also used cored bitumen-free, intact Athabasca samples (Touhidi-Baghini, 1998); the initial porosity in samples ranged from 33 to 35 percent, and the initial permeability for both horizontal and vertical samples was between 1.5 and 4 Darcys. In Oldakowski 's experiments for measuring the absolute permeability change, reconstituted oil-free oil sands samples and extracted sand cores were utilized within the same range when the porosities were similar (Oldakowski, 1994). Then the specimen preparation technique was modified and developed to prepare for a small size artificial oil sand sample in a lab (Hamoud, 2012). The technique controlled the geophysical properties of the sand cores very well. The key point was to pack the same amount of air-dry sand in the fixed bulk volume of the sleeve which was made of an aluminum cylinder with a dimension of 2" in diameter by 2" in height. A surcharge weight was applied vertically over the sample and a vibrator was utilized during sand packing. All the sands specimens could be removed from the split mould as well. Based on previous lab practice, the porosity of a beach sand core with an average grain size (D50) of 390 μm should not exceed 34%. The relatively high average porosity indicated the relative density of the cores was not as dense as expected, and it was attributed to the usage of a vibrator.

Through a series of lab testing program, Wong et al. realized that unique parameters were hard to attain from experiments due to the granular nature of oil sands and the effect of sample disturbance (Wong, Samieh and Kuhlemeyer, 1994). Therefore, the effect of sample disturbance on the stress-strain response must be minimized as much as possible. On one hand, the number of tests must be sufficient to characterize the geomechanical dilation behaviour. On the other hand, all the specimens should be as identical as possible in terms of the degree of disturbance for comparison and prediction.

Based on a great number of previous experiments, a better preparation technique has been developed, which is explained in the following section. Basically, a horizontal impact was employed in addition to vertical load during sand packing. A surcharge weight is necessary for applying load vertically over the sample, which not only limits sand grains from "dancing" freely, but also provides vertical stress to allow them to settle down. The preparation cell must be well-grounded to avoid grain's repelling each other due to electrical charge. This sample preparation technique provides a reasonably identical core specimen, under which a synthetic sample could be replicated.

3.4.2. Preparation Method of Synthetic Core Specimens in This Study[1]

In this study, an improved sand packing method is proposed. Synthetic cores were prepared in the Geomechanical Reservoir Engineering Facility (Geo-REF) at the University of Alberta. The core specimen preparation consists of five successive stages: sand packing, sands densification, fluid saturation, specimen freezing, and specimen extraction. The improved technique was based on previous sample preparation protocols at the University of Alberta. The previous technique could only provide 25 mm diameter by 25 mm (height) cylindrical samples; the new technique can produce high-quality specimens of 63.5 mm diameter and 152.4 mm in height.

Figure 3-16 shows the main parts of the sand packing assembly. The assembly also includes a differential pressure cell to monitor the differential pressure across the length of the core sample, and a pressure gauge to display pore pressure at the base of the cell during the core preparation.

[1] A partial of this chapter has been published.
Wang, X., Rick Chalaturnyk, H. Huang, and J. Leung. 2015. "Permeability Variations Associated with Various Stress State during Pore Pressure Injection." prepared for presentation at the 49th US Rock Mechanics/Geomechanics Symposium held in San Francisco, CA, USA, 28 June- 1 July 2015 (X. Wang *et al.*, 2015).

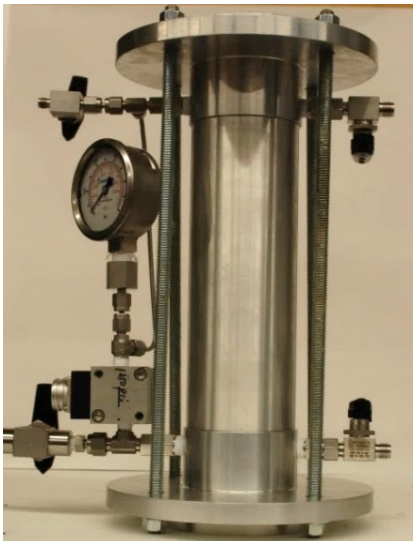

Figure 3-16. Image of sands core preparation apparatus assembly

3.4.3. Sand Packing for a Synthetic Core

During sand packing, sands were slowly and continuously poured into the metal cylinder until the sand level was close to the cylinder mouth. An extra cylindrical bar was placed on the sand to apply a vertical load. Vertical stress of 14 kPa was applied to the surface of the sands to compare the new method with the ASTM standard for measuring relative density (ASTM, 2000a, 2000b). Depending on the cross-sectional area of the surcharge rod, the surcharge weight can be modified. Based on a rod with a 6.1mm diameter, the surcharge mass is approximately 4,110 grams just as shown in the following Figure 3-17.

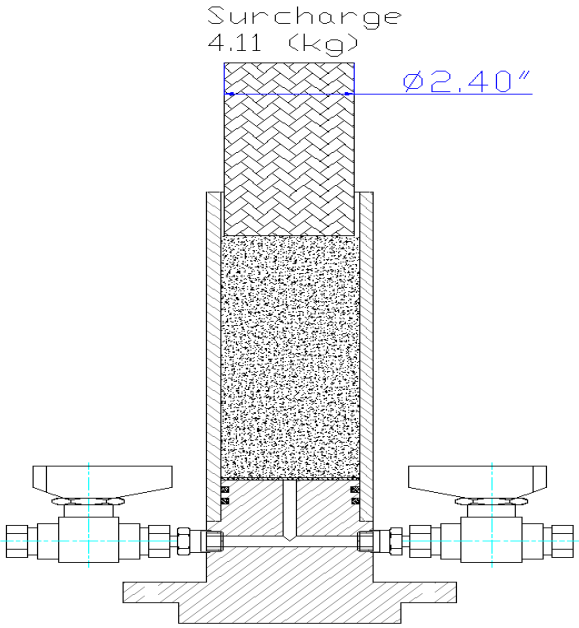

Figure 3-17. Schematic drawing of packing and densifying sand in a cylinder

An improved technique and method were developed to prepare a reliable and representative wet/oil sands specimen for reservoir geomechanical testing. The packing technique allows high quality, repeatable (porosity, relative density, and dry density), very dense sands specimen to be created.

3.4.4. Water Saturation in Synthetic Core

A sand core can be constituted by either dry packing or wet packing. Both packing methods could be considered to fully saturate the sands core with saline water to mimic reservoir fluids.

To prepare with a sand core by dry packing, dry sands were directly added in the preparation cylinder shown in Figure 3-17 and Figure 3-24. However, by using the method of wet packing, dry sands were soaked with deionized water in a container that was heated on a hot plate. Any air around the grains could thus be removed when the water was boiled for around five minutes. Sands were then packed in the preparation cylinder shown in Figure 3-17 and Figure 3-24 after the water and sands

cooled down to ambient temperature. Sands had been fully covered with water during the transfer from the container to the preparation cylinder to avoid air entering with sand grains.

A sands core, prepared by either dry packing or wet packing was then flooded with brine. A bottom injection of brine water was performed to avoid gravity segregation, as shown in Figure 3-18. The brine water was vacuumed prior to injection. The concentration of the saline water was 3.0 %, which had a high salinity of 30,000 ppm and was close to the salinity of seawater roughly 35,000 ppm. At room temperature, 20 °C, the density of the saline water is 1.0196 (g/cm^3) (Mostafa H, V and Zubair, 2013).

As per the classic protocol to prepare for a synthetic sands sample, the dry sand core was vacuumed first before it was wetted with saline water from the bottom to the top just as Polikar et al. completed in their test runs (Polikar *et al.*, 1988). For a wet sands core by wet-packing, injection of brine was needed to displace the deionized water in the core with saline water.

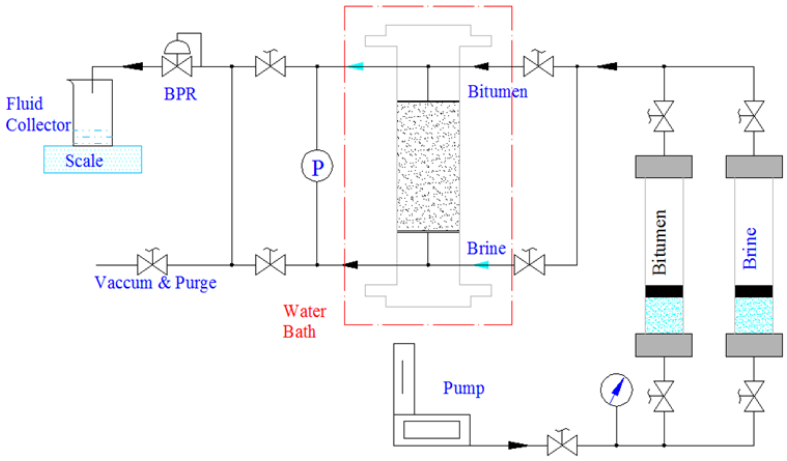

Figure 3-18. Schematic drawing of a fluid saturation system

3.4.5. Bitumen Saturation in Synthetic Core

After a sand core was prepared and then flooded with brine solution, two methods could be considered to obtain an oil sands core. One is to mix the wet sand and the desired bitumen sample. The free water in the wet sands core must be removed in a centrifuge (Ivory *et al.*, 1987) before sands were mixed with bitumen. One of the main problems with this method included air being trapped in the oil sand, which was a big issue for a test related oil sands recovery process. Dusseault et al. used similar compaction techniques to prepare for some oil sand samples and achieved 34.5- 37% of porosity (Dusseault, Soderberg and Sterne, 1984). The other way to prepare for oil sands specimens is to displace the water in the core with bitumen, in which the formation of air channels is minimized and the natural formation of oil sand deposits is closely simulated.

In a classic protocol to prepare a synthetic oil sands sample, the bottom injection of heavy oil or bitumen is performed to avoid gravity segregation. The average initial oil saturation of the synthetic oil core sample is approximately 90%. The results in Polikar et al.'s runs indicated that the synthetic oil sands samples by this procedure were relatively identical, reproducible, and consistent (Polikar *et al.*, 1988). However, a reversed flow was applied through the top after the wet sands core was saturated with hot bitumen for one and a half pore volume inIvory et al.'s test (Ivory *et al.*, 1987). Finally, the bitumen saturation ranged from 13 % at the top to 11 % at the bottom.

In this study, the brine-water-flooded sands cores were saturated with Mackay Lake bitumen by injecting the oil from the top to the bottom of the model which considered the density difference between water and oil. The injection rate of oil was set at a constant rate to maintain a uniform and smooth displacement interface. The oil saturation process was run in a heated condition. The oil container, the core preparation apparatus, and the saturation lines were wrapped with heating tapes and thermal insulation blankets to allow the temperature to maintain around 60 °C. Fluid flow was controlled with a needle valve as a back-pressure regulator in the system during oil saturation. The produced fluid was measured on a balance, and

the flood was terminated when 1.1 pore volumes of dead oil had been injected. The sand pack was then shut-in.

The amount of oil and the total initial water in the sands core was then tracked based on the material balance. Table 3-3 summarizes the initial conditions and fluid properties of the experiment.

Based on Table 3-3 and **Error! Reference source not found.**, the wet bulk density of core specimens ranged from 2.06 to 2.12 gm/cm^3, which were reasonably consistent from one specimen to another. When a core specimen was packed with the dry-packing method, it had a less wet density. It indicated that the wet-packing method provided a feasible way to densify a sands-based core specimen.

In Dusseault's research, the wet bulk density was calculated with 2.13 gm/ cm^3 (Dusseault, 1977).

Based on Table 3-3 and Figure 3-20, the porosity of core specimens ranged from 32.3% to 34.2%. For the core specimens packed with the wet-packing method, their porosities were maintained very close to each other.

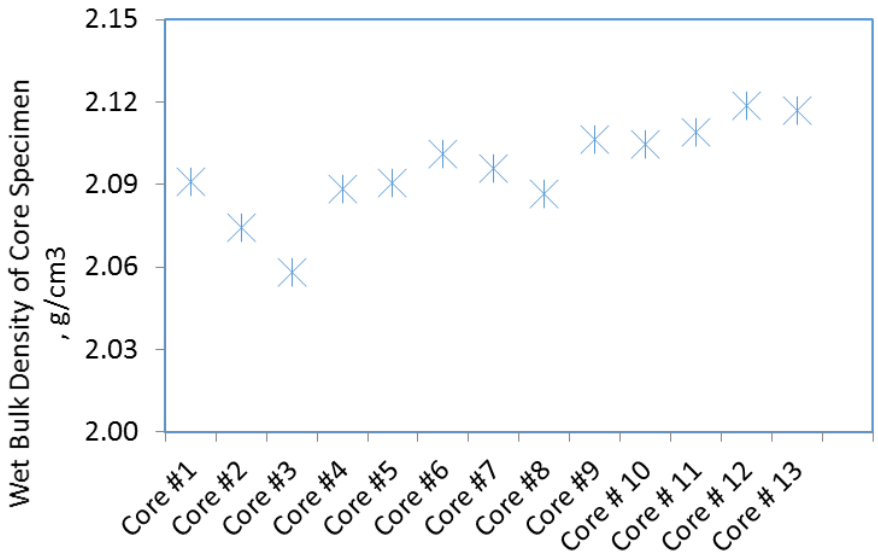

Figure 3-19. The wet bulk density of 13 core specimens

With the previous studies being considered, the porosity varied in a relatively big window range. In Dusseault's study, the porosity of the prepared specimens fell in the range from 30.7% to 32.3% (Dusseault, 1977). In Ivory et al.'s projects, the average porosity of four sand packings, the mixture of outcrop sand and 40/60 mesh of Ottawa sands by using their procedure ranged from 32% to 34 %. Due to limited data with few sands packing plugs, it was not possible to determine whether the core specimen was reproducible or not (Ivory *et al.*, 1987). In Polikar et al.'s study, totalling 51 cores packed with 140 mesh of sand, they showed an average porosity ranging from 31.8 to 35.8% (Polikar *et al.*, 1988). The initial porosity in samples ranged from 33 to 35 percent, and the initial permeability for both horizontal and vertical samples was between 1.5 and 4 Darcys (Touhidi-Baghini, 1998). By using the procedure mentioned in his thesis, Hamoud prepared twenty-two sand cores with porosity ranging from 34.51% to 35.65% (Hamoud, 2012).

Table 3-3 Summary of sands packing

Packing Method	Core No.	Wet Bulk Density, (g/cm^3)	Dry Bulk Density, (g/cm^3)	Porosity, (%)	Void Ratio, (cm^3/cm^3)	Relative Density, (%)
Dry Packing	Maximum	N/A	1.53	42.3	0.73	100
	Minimum	N/A	1.39	47.5	0.91	0
	Core #1	2.09	1.77	33.1	0.49	236
	Core #2	2.07	1.74	34.2	0.52	222
	Core #3	2.06	1.75	34.0	0.52	236
Wet Packing	Core #4	2.09	1.79	32.3	0.48	246
	Core #5	2.09	1.79	32.3	0.48	246
	Core #6	2.10	1.79	32.3	0.48	246
	Core #7	2.10	1.79	32.3	0.48	246
	Core #8	2.09	1.79	32.3	0.48	246
	Core #9	2.11	1.79	32.3	0.48	246
	Core # 10	2.10	1.80	32.2	0.47	248
	Core # 11	2.11	1.80	32.2	0.47	248
	Core # 12	2.12	1.80	32.2	0.47	248
	Core # 13	2.12	1.80	32.2	0.47	248

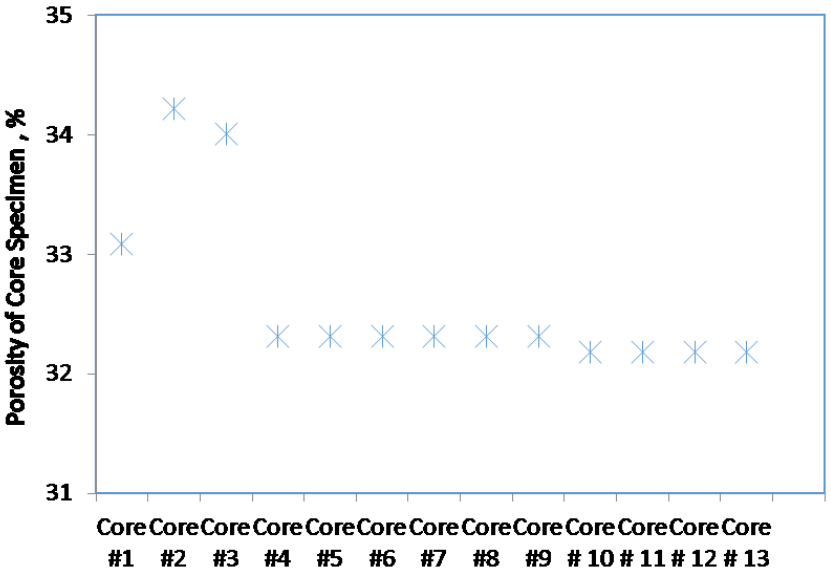

Figure 3-20. The porosity of 13 sands cores prepared in the lab

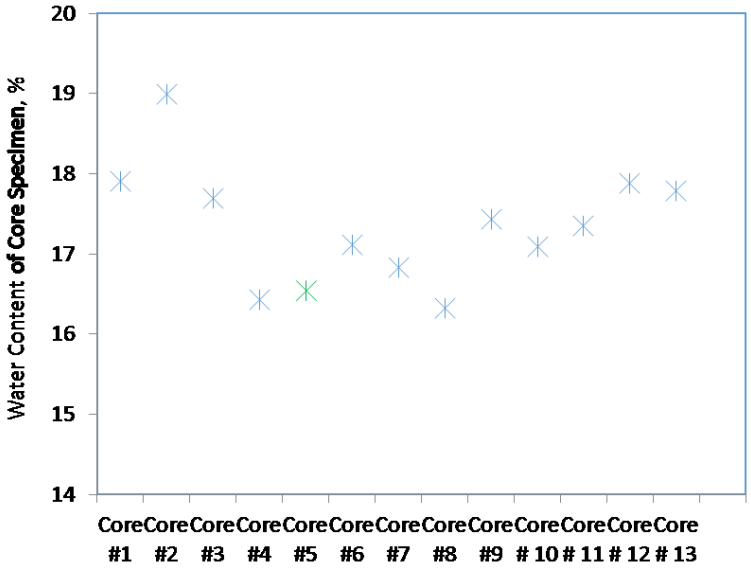

Figure 3-21. Water content of the core specimen

It can be found each single packing method cited above could not achieve a consistent porosity, and the porosities were relatively too high with respective grain sizes. Compared with the previous research results, it indicated that the sands packing method, which was developed and used in this study, has greatly improved quality control in terms of repeatability and consistency.

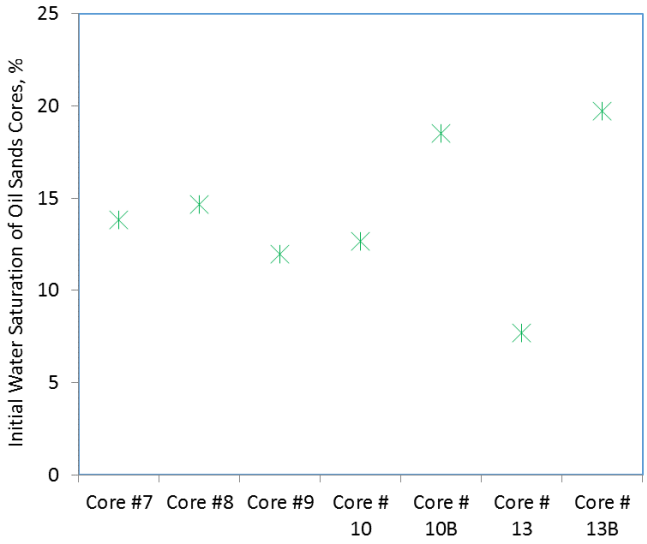

Figure 3-22. Initial water saturation of oil sands cores

Figure 3-21and Figure 3-22 reflects the amount of water in each core specimen, which was based on the material balance and calculation from its initial dry packing.

Figure 3-23. Snapped picture of densifying sand packing

Figure 3-23 shows a final, bitumen saturated sample, which was prepared and produced from the preparation apparatus described above. The uniform densified specimens were a cylindrical shape with 63.5 mm in diameter and 152.4 mm in height.

It was crucial to preserve the integrity of the sand core specimens, which had been constructed under a deep-low-temperature at around -60°C. The wet clean sands or bitumen-saturated sand cores were well sealed in a vacuum bag to prevent water from evaporating when they were sealed and stored in a freezer at -18°C, which minimized structural disturbances of the mineral grains and water content changes. An undisturbed core with high quality was critical to accurately determine the fluid flow behaviour in unconsolidated sands subjected to effective stress changes.

3.5. Developing a Technique to Densify Synthetic Core Specimens

The surcharge weight remained on the surface of the sand throughout the sand packing process. The cylinder wall was tapped continuously from top to bottom along the circumference of the packing cylinder cell with a 300-gram hammer. Tapping frequency was maintained at approximately 120 times per minute.

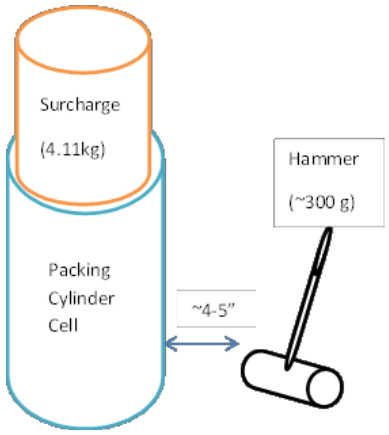

Figure 3-24. Schematic drawing of how to densify sand packing

The distance between the hammer and the cylinder was controlled with a range of 4 inches to 5 inches, as shown in Figure 3-24. Continuous tapping was required for around one full hour, which was equivalent to 20,000 times of random tapping on the surface of the cylinder. This was automated for future testing programs.

As the sand densified, the surcharge weight was removed to allow for sand addition and the process was repeated until a known mass of sand was packed into a known volume and hence, a known dry density or porosity.

Thirteen sands core samples were constructed, three of which were done with dry packing and the other ten with wet packing. For dry packing, oven-dried sands were used, and water flooding was induced to fully saturate the whole pack with liquid, while wet sands were packed during the preparation of the sands core.

It can be noted that the sands packing methods with applying the application of the improved technique provided higher dry bulk density and lower porosity compared with those as per the ASTM standards (ASTM, 2000a, 2000b). Specifically, the relative density was approximately 248%, which indicates that the sands packings were very dense.

More importantly, some of the physical properties of the core samples could be controlled and maintained consistently, e.g. bulk density, wet density, and fluid saturation.

The well-saturated sands were then transferred to the cylindrical cell, which was initially partially filled with DI water. The sand remained submerged in water during the entire course of the sand packing to avoid or minimize air being trapped in the core. Table 3-3 summarized some physical properties of the first thirteen sands specimens.

3.5.1. Determination of Relative Density

For sands, the maximum index density/unit weight is one of the key components in evaluating the state of compactness of given sand mass that is either naturally occurring or artificially packed. Relative density and percent compaction are commonly used for evaluating the state of compactness of a given sand mass. It is generally recognized that relative density is a good indicator of the state of compactness of a given soils or sands mass (ASTM, 2000a, 2000b).

The maximum and minimum index void ratio of sands is determined using test methods recommended by the American Society for Testing and Materials, which is a globally recognized leader in the development and delivery of international voluntary consensus standards.

However, the engineering properties, such as strength, compressibility, and permeability of a given sand mass, compacted by various methods to a given state of compactness can vary considerably. Therefore, considerable engineering

judgment must be used in relating the engineering properties of sands to the state of compactness.

The maximum index density and the minimum index density of sands are determined using test methods recommended by ASTM as well.

According to the ASTM standards (ASTM, 2000a, 2000b), the maximum index density, showing the minimum index void ratio (e_{min}) characterizes the densest condition of cohesionless, free-draining sands that can be attained by a standard laboratory procedure. Dried sands were packed on an electromagnetic, vertically vibrating table for determining the maximum index density in this study. The oven-dried sand was placed in the core preparation cell and a surcharge weight of 4.11 kg was applied to the surface of the sands. Considering the area of the cell cylinder with two and a half inches in diameter, the surcharge pressure is approximately 2-lb/in.^{2} (14-kPa). The cell with the surcharge weight was set on a vibrating table and vibrated continuously for 8 minutes at 60 Hz. Three runs of measurement were carried out before the maximum oven-dried mass was obtained; this is the maximum index density.

The maximum index void ratio, e_{max}, refers to the void ratio of sands at the minimum index density/unit weight. To obtain the minimum index density, the method of using a funnel pouring device or a hand scoop to place the material in the mould is utilized in this study. It represents the loosest condition of sands packing that can be attained by a standard laboratory procedure. The maximum index density is calculated by dividing the oven-dried mass/weight of the densified sands by volume (average height of densified soil times area of mould).

As

$$V_{total} = V_{void} + V_{sands} \quad \text{Eq. 3-3}$$

then,

$$e = \frac{V_{void}}{V_{sands}} = \frac{V_{total}}{V_{sands}} - 1 = \frac{V_{total}\rho_{sands}}{m_{sands}} - 1 \quad \text{Eq. 3-4}$$

With the same density and total volume for the sands in the experiments, the relative density can be expressed as the following.

$$D_d = \frac{e_{max} - e}{e_{max} - e_{min}} = \frac{V_{total}\rho_{sands}(\frac{1}{m_{max}} - \frac{1}{m})}{V_{total}\rho_{sands}(\frac{1}{m_{max}} - \frac{1}{m_{min}})} \quad \text{Eq. 3-5}$$

$$D_d = \frac{\frac{1}{m_{max}} - \frac{1}{m}}{\frac{1}{m_{max}} - \frac{1}{m_{min}}} \quad \text{Eq. 3-6}$$

Where,

e_{max}: the void ratio of the sands packing during the test for the maximum index density;

e_{min}: the void ratio of the sands packing during the test for the minimum index density;

m: the mass of the current sands packed in the cell;

m_{max}: the mass of the sands packed in the cell during the test for the minimum index density;

m_{min}: the mass of the sands packed in the cell during the test for the maximum index density;

Experimental results indicated that the improved method could yield significantly higher values of relative density for the sands used in the experiments. Although

the wet packing method might generate a higher maximum index densities/unit weights, the dry packing method was preferred as results can usually be obtained more quickly and air can't be easily entrapped in the packing.

Six runs were carried out for the minimum index density, with 661.60, 647.32, 649.66, 641.20, 644.83, 642.11, grams of sands, respectively, packed into the same cell up to the same level marked. The second least value (642.11) was considered as the mass of the sands packed in the cell during the test for the minimum index density.

Three runs were carried out for the maximum index density, with 691.30, 683.55, and 706.67 grams of sands, respectively, packed into the same cell up to the same level marked. A mass of 4110 grams of surcharge rod was utilized in all three runs for the maximum index density. Each run was conducted using 60Hz of frequency and eight minutes for vibration. The greatest value (706.67) among three runs was considered as the mass of the sands packed into the cell during the test for the maximum index density.

With the specific testing protocol for this study, 799.8 grams of sands were packed in the same cell up to the same level. Therefore, 215.8% of relative density was achieved by applying specific packing methods.

Sands for the test specimens were obtained from tailings sand, which was sourced from the McMurray Formation oil sands formation. Sieve analyses (Xinkui Wang *et al.*, 2015) indicated a relatively large range of particle sizes and relatively uniform and well-graded sands with an effective size D10 of 105μm and an average grain size D50 of 200 μm.

It can be noted that the method proposed in this study could yield significantly higher values of relative density for the sands used in the experiments. The wet packing method can generate a higher maximum index densities/unit weights.

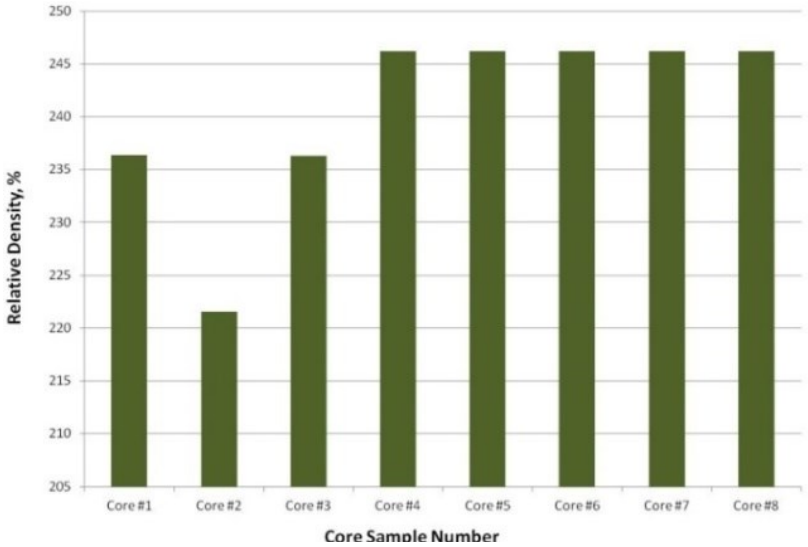

Figure 3-25 Relative density of the core specimen

3.5.2. Fluid Saturation and Quality Assessment of Oil Sands Specimen

It is crucial to keep the fluid saturation well distributed along the core length in the series of experiments related to geomechanical dilation and triaxial compression. Experimental techniques were developed to inspect and assess the sample quality in terms of fluid saturation distribution and dense in the core. Some destructive and non-destructive techniques (Sedgwick and Miles-Dixon, 1988) have been developed, which include X-ray CT scanning, microwaves, electric resistance, X-ray and γ-ray attenuation, and nuclear magnetic resonance.

The key element to reducing disturbance of a core is to treat the core material with appropriate methods and to avoid negative impacts of fluctuating temperature, losing moisture, and defective texture during core preparation for testing. The Dean-Stark analysis is another option for material content at each separate section along the core length.

3.6. Discussion on Specimen Preparation

Reliable geomechanical and geophysical parameters are required for use in design, numerical simulation, and evaluation of new recovery technologies. A test on studying the multiple phase flow behaviours and geomechanical responses through porous media models is therefore of some general interest. Many preparations and testing methods have been developed over the last several decades for oil sands recovery testing. Considering the difficulties of obtaining a non-disturbed representative field specimen, this innovation disclosure provides a convenient methodology. It provides a feasible and practical technology to produce an oil sands specimen with high quality, in terms of retaining uniform distribution of grain size, density, fluid saturation, and porosity along the length of a core plug. It is a reliable technique to reproduce almost identical oil sands samples, and from which the desired characteristics can be obtained.

Preparation techniques were developed by some researchers (Dusseault, Soderberg and Sterne, 1984; Scott, Proskin and Adhikary, 1994) for sampling an oil sands core from the field at the University of Alberta. A sample must be treated to minimize structural disturbance, gas evolution, and expansion of cohesionless fabric. It should be kept wrapped in plastic stored in a refrigerated room. Before trimming, a sample should be stored in dry ice to provide the rigidity required for cutting and lathing.

It can be noted that the sample preparation technique by Ivory et al. is able to provide reasonably identical core specimens (Ivory *et al.*, 1987). The identical synthetic sample could be replicated under this packing technique, although it could be conducted much better. However, the packing procedure used by Polikar et al. could not control the geophysical properties of specimens well (Polikar *et al.*, 1988). The issues mainly resulted from the preparation techniques, including the deformable sleeve and inconsistent packing procedure. All the cores could be taken out of a core holder and be used in another parametric testing. As the tube is made of a Lucite tube, which is not rigid enough under high pressure and high

temperature, the net volume of the packing chamber might fluctuate with varying temperatures and pressure. The porosity, density, and permeability of the sand packing could not be maintained consistently during sand packing and fluid flooding. It is hard to produce relatively identical core specimen from time to time. By using a vibrator during sand packing, a relatively loose packing was almost unavoidable due to insufficient stress from vertical direction except for the gravity of sand grains. The extra time duration of vibration did not help to compact or densify the packing. Layered structure with coarse sands upwards might be apparent along the length of the core, which is a big issue due to anisotropic permeability distribution in the core.

A few core preparation methods have been developed over the last decades for oil sands and carbonate bitumen recovery testing. Notwithstanding the limited practices for successful preparing core specimens (including oil sands, shale, and carbonate), there remain some gaps to provide the core specimen with the least disturbance.

This technique provides the capability to prepare high-quality oil sands samples that possess almost identical geophysical properties. It greatly enhances the capability of researchers to study the fundamental behaviours related to reservoir engineering and geomechanical engineering.

This study presents an improved technique and method to prepare for a reliable representative water wet/oil sands specimen for laboratory analysis. A series of synthetic wet/oil sands core specimen has been prepared with different fluid saturation using reclaimed/cleaned tailings sand from oil sands mining operations, which are representative of McMurray Formation oil sands. The updated approach of sand packing greatly enhances the capability to study fundamentals related to reservoir engineering and geomechanical engineering.

3.7. Geomechanical Properties at Elevated Effective Stress Through Triaxial Compression Tests

In the determination of mechanical properties of the reservoir geomaterials, various laboratory testing programs have been initialized in the last decades through scholars' and engineers' studies. The majority of fundamental research works have been conducted by degree pursuers under their academic supervisors at the University of Alberta's Oil Sands Geotechnical Research Facility and InnoTech Alberta (previously AITF: Alberta Innovates –Technology Futures, and ARC: Albert Research Council). These include but not limited to the following: (Dusseault, 1977), (Agar, 1984), (Howard Douglas Plewes, 1987), (Kosar, 1989), (Oldakowski, 1994), (Chalaturnyk, 1996), (Touhidi-Baghini, 1998), and (Hamoud, 2012). Some other recent works have been carried out at other facilities, which include Wong et al. at the University of Calgary, University of Waterloo, and Hamza et al. at the University of Texas at Austin (Hamza, 2012).

In this study, a set of triaxial compression tests allowed the shear strength and stiffness of oil sands to be determined for use in numerical simulation. Advantages over simpler procedures, such as the direct shear test, include the ability to control specimen drainage, take measurements of pore water pressures, and determine permeability variation before and after the shear failure of a core sample.

The main objective of these tests was to obtain the elastic and strength parameters of the oil sand to be used in the geomechanical numerical simulations of the reservoir materials' behaviour during SAGD operations. Specifically, all the parameters measured through the triaxial compression testing served as inputs for the geomechanical models to assess the impacts of geomechanical dilation as a start-up process in full SAGD performance.

Three compression tests on different effective stress conditions were conducted to obtain the Mohr-Coulomb failure envelopes. All triaxial tests were conducted at the drained condition, which meant the pore pressure was kept constant at 2000 kPa

and pore fluid was free to move in or out of the sample. The B-value was also obtained at the start of each experimental run. Continuous permeability tests during shearing were also conducted in all the tests.

The primary parameters obtained from the set of triaxial compression tests, included friction angle, cohesion, dilation angle, and the shear strength related to the specimens tested. Other parameters, such as the shear stiffness, Mohr-Column envelope, and permeability may also be determined.

3.7.1. Triaxial Compression Test Setting

The sands core specimens used in the set of the triaxial test were originally prepared in a lab with the same techniques described above. In this set of triaxial compression tests, all three sands cores were bitumen free.

All the core specimens were kept frozen before and during placement in the triaxial cell. The core specimen was trimmed to the same dimensions in terms of diameter and length. A specimen with a nominal 63 mm (2.5 inches) in diameter and 127 mm (5 inches) in height was carefully prepared using a diamond circular saw. The ratio of height to diameter for each compression test was kept around 2.0. Figure 3-26 shows the sample specimen used in the triaxial compression test prior to the testing.

The mass, dimensions, and images of the core specimen were recorded as a reference. All three triaxial compression tests were conducted by placing the cylindrical specimen into a pressure vessel.

Figure 3-26. Sands core specimen used in one test prior to conducting the triaxial compression test

The specimen with an approximate 2:1 height-to-diameter ratio was first sealed within a silicon membrane. After a core specimen was placed on the pedestal, drainage tubing was attached to the top cap and the cell base. The specimen was placed between two end caps and saturated sintered stainless steel porous stones. Two LVDT sensors were mounted around the mid-height and the bottom of the specimen outside of the silicon sleeve, respectively, to measure the strain variance along the circumference of the core during the compression testing. An LVDT sensor was attached to the rings to monitor the vertical strain, as shown in Figure 3-27.

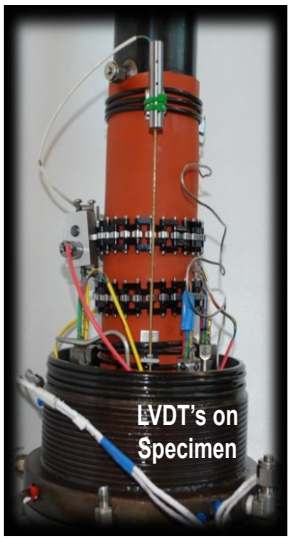

Figure 3-27. A sands core encased in a silicone sleeve and mounted on the pedestal and three LVDT sensors mounted to measure strains along the circumference and length of the core

Vacuum pressure was then applied to evacuate air from the system and the portion of pore space occupied by gas. As a result, a positive pressure equal to around 90 kPa was created around the core specimen. It was an effective and efficient way to detect if any leakage would occur. Meanwhile, dry ice was used to cover the core specimen to maintain it in the pressure shell and to help preserve the integrity of the sand core specimen under deep-low-temperature. Once the core specimen and its system were determined to be leakage-free, the shell would cover the core specimen and its attachment, and connect with the cell base to close the triaxial cell. The cell was then filled with mineral oil, which served as the medium for applying confining pressure.

The triaxial cell was then transferred and housed in the environmental chamber, where the temperature was controlled by a circulation chiller and pre-set to 10°C. All external drainage lines and instrumentation were connected at this point and back pressure (pore pressure) was applied. The final assembly of the cell was completed by connecting it with the back-pressure system and cell pressure system before a positive confining pressure could be applied.

3.7.2. Procedures of Triaxial Compression Test

The general procedures for a drained triaxial compression test include the following:

1. Preparation of a cylindrical specimen
2. Placement of core specimen in a rubber sleeve
3. Instruments installation between end caps in the pressure vessel
4. Application of confining pressure
5. Saturation of the core specimen with brackish water
6. Consolidation of the core specimen
7. Setting of the predetermined effective confining stress
8. Compression of the core specimen
9. Increase of axial load at a constant rate until the specimen fails
10. Continuity of axial load to reach its residual strength conditions.

The ram of the Instron machine was then moved down and contacted the ram of the triaxial cell to apply an axial load on the core specimen. The saturation lines and pedestals were fully charged with de-ionized water with 3000 ppm salinity fluid. After the injection line, the production line, and the confining port were connected properly, small effective stress was kept throughout the process of specimen saturation by increasing cell pressure and accordingly increasing pore pressure with injected formation water.

All specimens were saturated at pore pressures approximately equal to those of the reservoir i.e. 2000 kPa for sand core specimens. An effective stress of 50 kPa was applied to the core, which was isolated from a silicon membrane. The back (pore) pressure and the cell pressure were incrementally increased to 2000 kPa and 2050 kPa, respectively. The mean effective confining stress of 50 kPa was maintained over 12 hours and allowed the core to thaw completely and saturate with water throughout the entire specimen volume.

The pressurized specimens were left overnight to allow for the dissolution of any gas that could remain in pore space. The B value tests were carried out where the

relationship between a change in confining pressure and the corresponding pore pressure was calculated. A ratio of the pressure differential between the confining pressure and the corresponding pore pressure approximated to 1.0, which indicated that the state of full saturation was achieved along the length of the core specimen.

To reach the stress conditions specified for each test, the cell pressure was increased (and decreased, if necessary) while maintaining the pore pressure at 2000 kPa. Successive load increments were applied once consolidation had ceased.

Before applying deviatoric stress to shear the sample, isotropic consolidation was carried out on the sands specimens. The sample was isotopically consolidated to $\sigma_3' = 50$ kPa, 100kPa, 200 kPa, 400kPa, 800 kPa, 1600kPa, and 3500 kPa, then unloaded gradually to $\sigma_3' = 100$ kPa from 3500kPa, and again loaded to $\sigma_3' = 3500$ kPa from 100 kPa. Finally, the core specimen was unloaded to 500 kPa, or 1500 kPa, or 3500 kPa before each triaxial compression test, respectively.

All specimens were consolidated by means of several cycles of isotropic confining stresses while the pore pressure was kept unchanged. The maximum effective principal stress was equal to approximately 3500 kPa for sand specimens. All triaxial compression tests were conducted at fully drained conditions. Therefore, low axial strain rates were used to allow for sufficient time for pore pressures to come to equilibrium within the specimens due to volumetric changes. A shearing rate of 5% per day, which was equal to 5.8×10^{-7} (1/s) of strain rate was used. Load and strain readings were continuously recorded by the data acquisition system.

At the end of the shear test, the compression machine Instron was stopped, the back and cell pressures were released and the triaxial cell was removed from the loading frame. The triaxial cell was then carefully disassembled and the specimen was preserved in the moisture room.

During the compression under the drained shear conditions, the back-pressure valve was left open and fluids were permitted to flow into or out of the specimen. Volume

change was measured by the positive displacement pump used to control the pore pressure, which was set to the constant pressure control mode during drained shear.

3.7.3. Three Triaxial Compression Tests

Drained triaxial compression tests were carried out at three elevated confining effective stresses. This section presents the results of geomechanical compression testing and analysis performed on three artificial sands core samples. The sands came from geological facies of McMurray Formation.

3.7.3.1. Initial Conditions of Specimens

The sands samples were prepared with the same sands packing methods and were expected to be almost identical in terms of porosity, void ratio, bulk density, dry density, particle size distribution, and water saturation. Every core specimen had been manipulated to vary and examine the different amounts of effective stress.

The initial conditions of tested specimens were summarized in Table 3-4. It includes specimens' mass, height, diameter, and void ratio both 1) just after trimming, still in the frozen state, and 2) after they were mounted in the triaxial cell and exposed to effective confining stress of 94 kPa.

Table 3-4 Summary of test results at initial stages of triaxial tests of samples

Test Number	Core Number	Diameter (mm)	Height (mm)	Mass (g)	Area (m^2)	Void Ratio
13	15	64.15	124.11	831.9	3.23E-03	0.474
11	14	63.77	117.96	775.6	3.18E-03	0.474
12	12	63.88	128.37	843.9	3.21E-03	0.465

3.7.3.2. Measurement of B value and Reconsolidation

The ratio of the pore pressure change to the confinement stress change under isotropic loading is denoted by B value, which is related to the excess pore pressure to an increment of deviatoric stress, as shown in the following.

$$B = \frac{\Delta u}{\Delta \sigma} \qquad \text{Eq. 3-7}$$

The level of B value reflects the saturation degree of the core specimen. The measurements of B value at the effective stress $\sigma_3' = 500$ kPa, 1500kPa, and 3500 kPa are shown in Figure 3-28, which depicted the relationship between the differential pressures of the confining pressure and the corresponding differential pressures of the pore pressure. The slope of the curve approximated to 0.90, which reflected that the state of almost full saturation was achieved along the length of the core specimen.

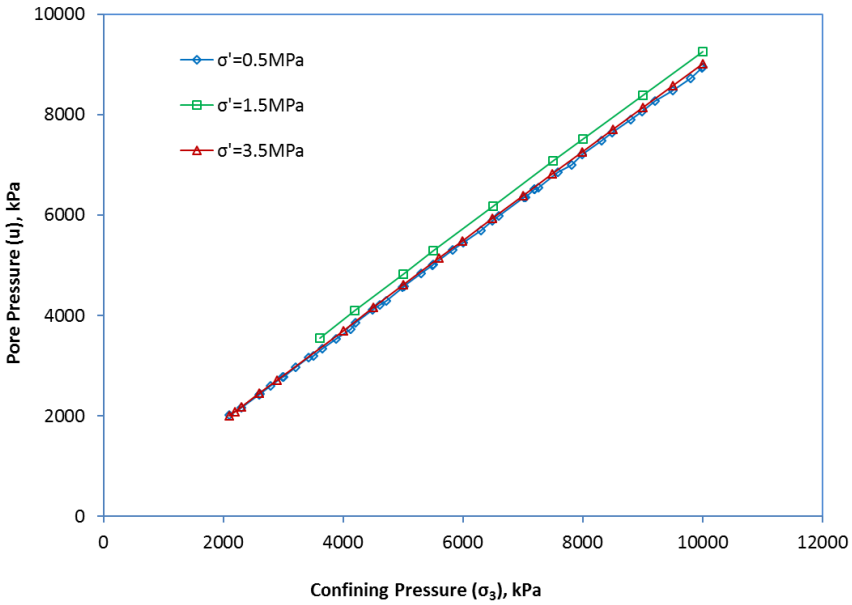

Figure 3-28. B-Test after the core specimen thawed overnight in the triaxial cell for test specimen at 500, 1500, 3500 kPa effective stress, respectively

After pre-shearing permeability measurements, deviatoric stress was applied and changes in the condition of the specimen (i.e. vertical displacement and pore volume change) were recorded during the test.

3.7.3.3. Consolidation and Compressibility Coefficients

All three synthetic sand specimens were consolidated by means of several cycles of isotropic stresses to establish similar stress conditions as in-situ environments. The same procedure was used to deal with a fresh core, which was extracted from the field. The maximum effective stresses used were approximately equal to the minimum principal stresses, which was 3500 kPa in the case of oil sands specimens. During the geomechanical compression tests, the pore pressure, the confinement pressure, the axial compression stress, and both circumference and vertical strains were logged and recorded.

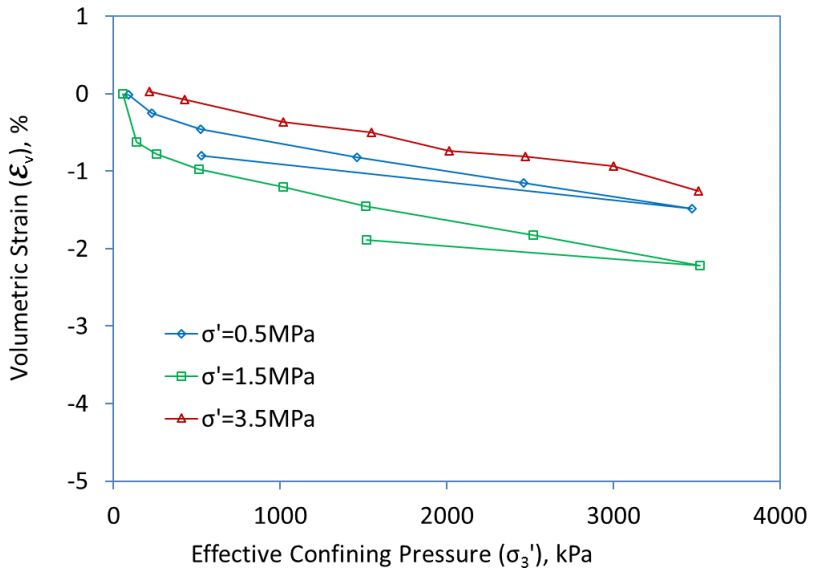

Figure 3-29. Compressibility curve for test specimen at 500 kPa effective stress

After consolidation, the dimensions of the core were recorded in Table 3-5. The volumetric strains decreased by 1.50%, 1.89%, 1.26%, respectively, for the three tests, which were associated with the effective stresses of 500kPa, 1500kPa, and 3500kPa. The axial strains decreased by 0.32%, 0.38%, and 0.31%, respectively, during the reconsolidation.

Table 3-5. Summary of test results after the isotropic consolidation of triaxial tests of samples

Test Number	Core Number	Height (mm)	Area (m^2)	Void ratio	Volumetric Strain (%)	Axial Strain (%)
13	15	123.71	3.20E-03	0.453	-1.50	0.32
11	14	117.51	3.15E-03	0.447	-1.89	0.38
12	12	127.97	3.18E-03	0.446	-1.26	0.31

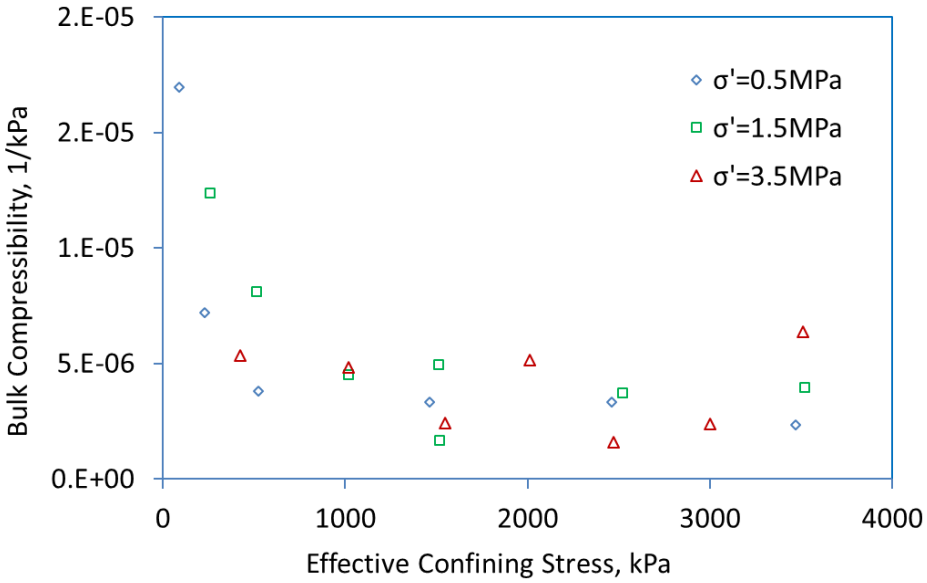

Figure 3-30. Bulk compressibility (1/kPa) vs. effective confining stress (kPa) at 500, 1500, 3500 kPa of effective stress, respectively, during a shearing test on sands specimens

The results of the consolidation tests were plotted in Figure 3-30, which depicted the bulk compressibility versus the applied isotropic effective stresses.

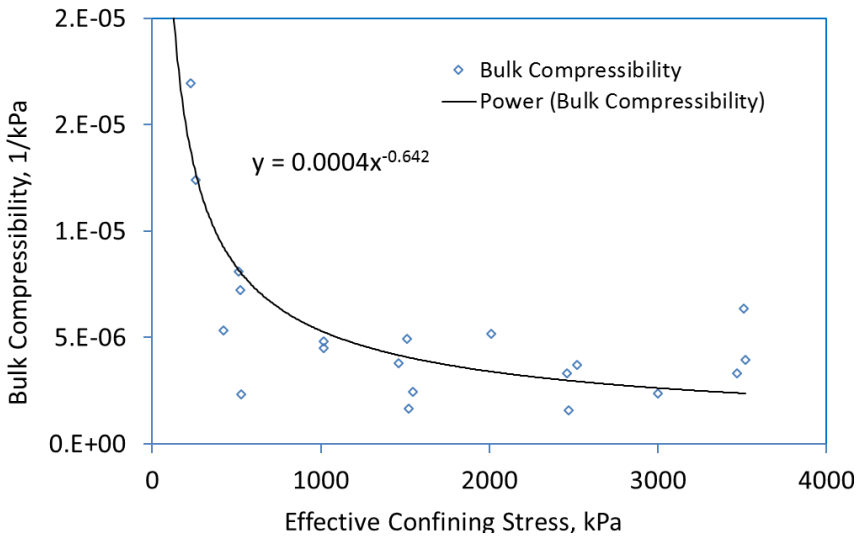

Figure 3-31. Bulk compressibility (1/kPa) versus effective confining stress (kPa) during a compression test on sands specimens

Figure 3-31 also contained points representing the bulk compressibility coefficient C_b calculated as the ratio of volume change to the corresponding stress change ($C_b = \frac{\Delta V}{\sigma_3'}$). The best fit to those points with the power-list-square function was expressed as the following.

$$C_b = 0.00042\ (\sigma_3')^{-0.64}, kPa^{-1} \qquad \text{Eq. 3-8}$$

where σ_3' is in kPa, applicable only in the range from 500 kPa to 3500 kPa.

3.7.4. Experimental Results from Triaxial Compression Tests

3.7.4.1. Relationship between Deviatoric Stress and Axial Strain

The deviatoric stress or differential stress is defined as the difference between the confining pressure (σ_3) and the total axial stress (σ_1), which is determined by the axial load divided by the cross-sectional area. The load was measured by the load cell installed in the loading frame of the Instron machine, and the cross-sectional area was calculated using the specimen's initial dimensions and the deformation data.

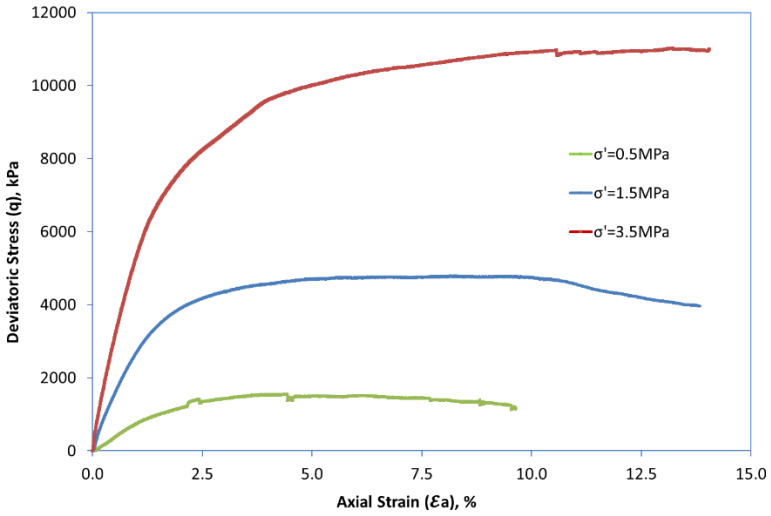

Figure 3-32. Deviatoric stress variation (kPa) versus axial strain (%) for test specimen in the triaxial cell at three different effective stress levels

The confining pressure (σ_3) was equal to the intermediate principal stress (σ_2) under the compressive state. The deviatoric stress is plotted against axial strain (ε_L), which was equal to the change in specimen length (ΔL) divided by its initial length (L_i).

The variation of deviatoric stress (kPa) versus axial strain (%) was exhibited in the following graphs Figure 3-32. Two distinct values for deviatoric stress were supposed to appear in the curves: the peak and the residual values. These two values of deviatoric stress would be used to obtain the shear strength parameters of sands.

Based on Figure 3-32, the deviatoric stress reached the peak value of 1530 kPa at the axial strain around 4.0 %, which reflected the maximum value for deviatoric stress under the effective stress of 500 kPa. Under the effective stress of 1500 kPa, the maximum stress reached 4700 kPa and continued with a very slight decrease starting with the axial strain of around 5.0 %. The deviatoric stress decreased eventually when the axial strain was greater than 10.0 %. As expected, the maximum stress approximated 11000 kPa under the effective stress of 3500 kPa.

The residual stress indicated the amount of deviatoric stress at which the deviatoric stress remained constant. However, the residual values for the deviatoric stress were not as distinct as the declining trend continued with the increasing axial strain, and there were no inflection points until the end of the compression test.

3.7.4.2. The relationship between Volumetric Strain and Axial Strain

The volumetric strain (ε_V) was plotted against axial strain (ε_a), which was equal to the change in specimen length (ΔL) divided by the initial length (L_o). The confining pressure (σ_3) was equal to the intermediate principal stress (σ_2) under the compressive state. The volumetric strain (ε_V) was plotted against axial strain (ε_a) Figure 3-33, which was equal to the change in specimen volume (ΔV) divided by its initial volume (V_o).

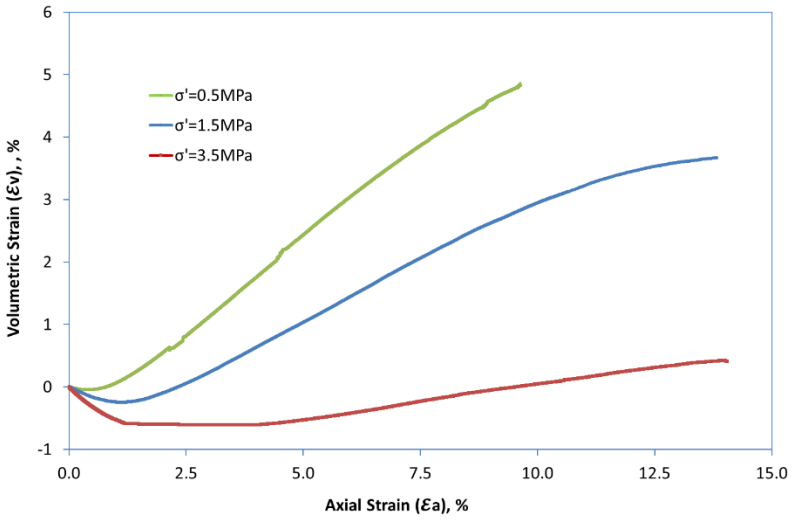

Figure 3-33. The pattern of volumetric strain variation (%) vs. axial strain (%) at three different effective stress levels, during a shearing test on sands specimens

Based on Figure 3-33, the volume of the sands specimen contracted and shrunk slightly when the specimen was compressed at the beginning of the test. Then, the sands specimen dilated, and the volumetric strains increased. Under lower effective stress, the specimen showed bigger volumetric strains. The volumetric strains reached around 2.5 % at the axial strain of around 5.0 %, and the trend kept increasing under the effective stress of 500 kPa. Under the effective stress of 1500 kPa, the volumetric strains reached the bottom point of -0.2 % at the axial strain of around 1.1 %. The volumetric strains kept below zero until the axial strain rose to around 10 %.

3.7.4.3. Frictional Angles

Mohr-Coulomb failure analyses for oil sands were conducted from the results of the three drained triaxial compression tests at the effective stress of 500kPa, 1500 kPa, and 3500 kPa. The stress paths were plotted on a diagram with s'-t coordinates shown in Figure 3-34. The horizontal coordinate is defined as equal to the medium stress s' between maximum and minimum effective stresses:

$$s' = (\sigma_1' + \sigma_3')/2 \qquad \text{Eq. 3-9}$$

Where t is equal to half of the deviatoric stress:

$$t = (\sigma_1' - \sigma_3')/2 \qquad \text{Eq. 3-10}$$

Using peak strength points of stress paths, a linear relationship between shear stress and the normal stress was constructed and depicted as Figure 3-34.

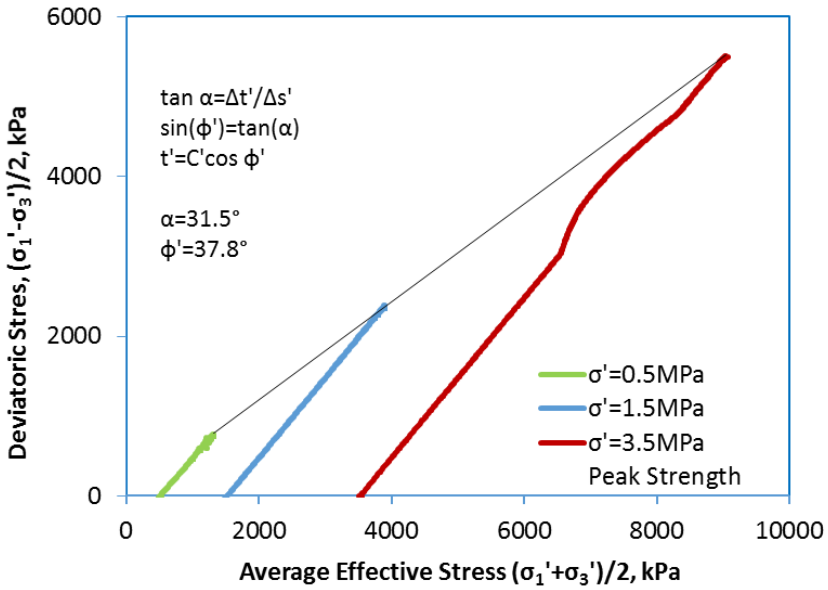

Figure 3-34. Triaxial test – t' vs. s' during compression for the test specimen

The curve of the peak strengths at three different effective stresses can be approximately expressed as the following for the effective σ_3' ranging from 500 kPa to 3500 kPa.

$$t = 0.612s' - 22.012 \quad \text{Eq. 3-11}$$

The slope of the tangential line to this curve can be used to calculate the friction angle. The slope of the curve is 0.612, and the intercept is the cohesion -22.0 kPa, which is close to zero. Oil sands are loose sands, held together by bitumen. However, bitumen does not act as a cementing agent since it is a Newtonian fluid even at 10°C and hence provides no shear resistance at a zero-shear rate. Therefore, it cannot contribute to the static mechanical strength of the material, provided the deformation does not proceed very rapidly (Dusseault, 1977), and the cohesion can be set 0.

Therefore, the angle (α) of the curve against the X- axial is 31.5°.

$$tan(\alpha) = \sin(\psi') \quad \text{Eq. 3-12}$$

Then, the frictional angle (ψ') is: 37.8°

3.7.4.4. Young's modulus and Poisson's Ratio

The Young's modulus values and Poisson's ratios were measured accordingly and the relationships between Young's modulus values and Poisson's ratios were then described. The slopes of deviatoric stress curves shown in Figure 3-32 were used to determine the values of the initial Young's modulus (E) for each oil sand specimen. Due to the strong curvature of the stress-strain curve for sands specimen, Young's modulus (E) was determined as the slope of the secant that passed through the initial point of deviatoric stress and the point on the curve corresponding to 0.25% axial strain. Poisson's ratio (ν) for sand core specimen was determined by

the linear fit to the radial strain (ε_R) versus axial strain (ε_a) curves for the range of axial strains from 0 to 0.25 %.

These values are included in Table 3-6.

Table 3-6 Young's modulus measured in the compression test corresponded with the effective confining stress

Effective Confining Stress σ'_3 (kPa)	*Young's modulus E* (MPa)
500	65.2
1500	345.6
3500	698.4

The relation between Young's modulus and the effective stress was then depicted in Figure 3-35. It can be observed that Young's modulus is also strongly dependent on the applied confining effective stresses, as shown in Figure 3-35.

The relationship between Young's modulus and effective coffining stress at the testing temperature of 10 °C can be described by a power function.

$$E = 95.6 \times 101.3 \times \left(\frac{\sigma_3'}{101.3}\right)^{1.23} \quad \text{Eq. 3-13}$$

where E is expressed in MPa, and σ_3' is expressed in kPa.

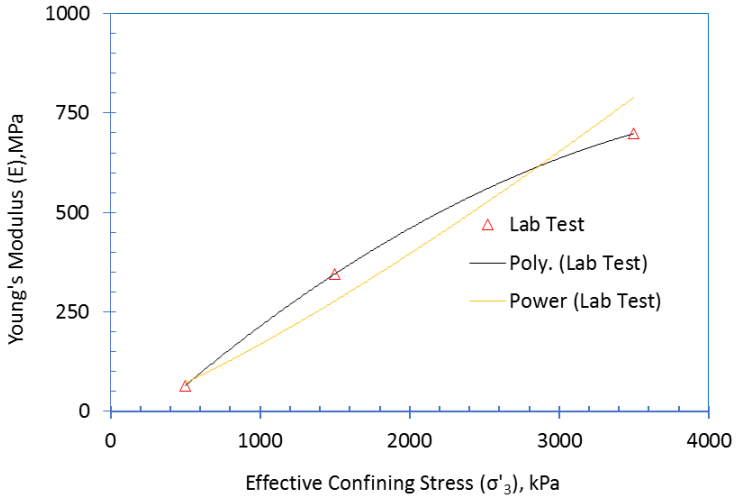

Figure 3-35. Young's modulus during a shearing test on sands specimens

The relationship between Young's modulus and effective confining stress, if expressed as a linear function, is the following.

$$E = 0.206\sigma_3' \qquad \text{Eq. 3-14}$$

Compared with the results of Li et al, plotted in Figure 3-36 the slope of the curve of Young's modulus obtained from the lab measurement was steeper than regression reported by Li et al. (Li, 2006).

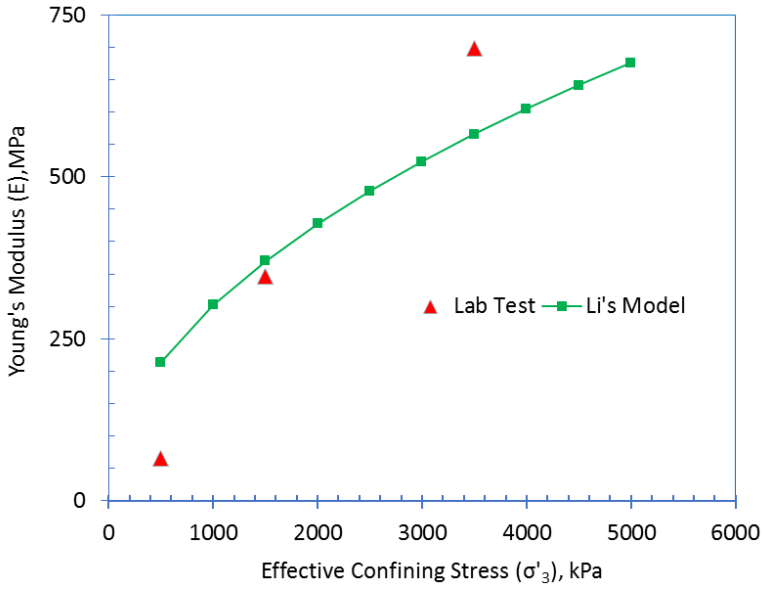

Figure 3-36. Comparison of Young's modulus obtained from the current study for oil-sands core specimen with one from literature

CHAPTER 4. EXPERIMENTAL VERIFICATION ON GEOMECHANICAL DILATION THROUGH COLD-WATER INJECTION[2]

The geomechanical response and multiple phase flow behaviours of geomaterials such as oil sands are required for forecasting and evaluating SAGD performance. These properties' databases are intended not only for use in demonstrating and verifying the concept of geomechanical dilation during the fluid injection but also for input into numerically modelling, which is used in studies of thermal recovery processes including SAGD.

This chapter provides details on the set of triaxial tests on sands specimens.

4.1. Geomechanical Dilation Testing of Oil Sands

4.1.1. Boundary Conditions of Geomechanical Dilation

The following tests were conducted through a set of lab-scale triaxial cell tests on synthetic oil sands cores or bitumen-free sands cores. The effects of initial isotropic stress state, initial anisotropic stress states, type of fluid-saturated, pore pressure, and the injection rate have been evaluated.

Seven test runs were carried out to assess dilation mechanisms associated with four types of stress conditions, as shown in Figure 4-1. Test #1 (sample 2, a water-saturated sand core) and Test #2 (sample 7, a bitumen saturated, water-wet sand core) were carried out under an initial isotropic stress of 3.5 MPa. Both horizontal effective stress and vertical effective stress were maintained at 3.5 MPa during pore pressure injection.

[2] Partial results of the presented work have been published in: (Xinkui Wang *et al.*, 2015) and (Wang et al., 2018): 'Experimental Study on Geomechanical Dilation during Injection'.

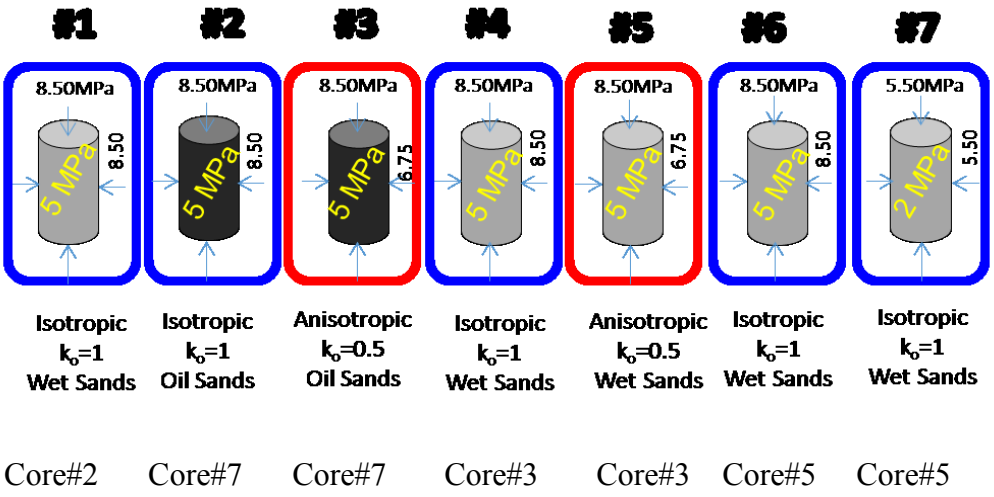

Figure 4-1. Boundary conditions of seven tests on dilation due to pore pressure injection (grey colour indicates brine saturated specimen and black colour indicates bitumen saturated specimen)

Test #3 (sample 7, bitumen saturated specimen) was conducted for pore pressure injection under an anisotropic stress condition. The stress ratio was 0.5; 1.75 MPa horizontal effective stress and 3.5 MPa vertical effective stress. Test #4 repeated the same boundary stress conditions as Test #1 and was designed to confirm the repeatability for a newly packed sands core specimen under the same boundary conditions. Test #5 repeated the same stress boundary conditions as Test #3 to investigate the difference of dilation behaviour for two types of core specimens saturated with a different fluid.

Table 4-1. Petrophysical properties of cores used in the triaxial tests

Test Number	Sand Core Tag	Bulk Volume (cm^3)	Mass of Core (g)	Porosity (%)	Relative Density (%)	Water Saturation (%)	Bitumen Saturation (%)
#1	Core #2	407.4	812.3	34.2	221.6	100.0	0.0
#2 & 3	Core #7	395.7	824.0	32.3	246.2	13.8	86.2
#4 & 5	Core #3	400.4	800.2	32.6	236.3	100.0	0.0
#6 & 7	Core #5	386.7	788.0	32.3	246.2	100.0	0.0

Test #6 and Test #7 were designed to examine the impact of pore pressure on the volumetric strain with the same effective stress. The petrophysical properties of each core specimen used in the testing program can be also found in Table 3-3.

4.1.2. Geomechanical Response under Initial Isotropic Stress State

Test #1, #2, #4, #6 and #7 were designed to investigate the impacts of initial isotropic stress state on geomechanical dilation and multiple phase flow behaviour. Figure 4-2 depicts the relationship between volumetric strains and effective horizontal stresses during water injection under an initial isotropic stress state. All these tests were conducted along a stress path with a reduction in the mean effective stress and a constant of deviatoric stress as shown in Figure 4-3.

After a long period (average of 2 days for water-wet sand cores and 10 days for oil sand cores) of water injection, the effective stress gradually dropped and the sand core expanded slowly. The sand cores including oil sands specimen in Test #1, #2, #3, #4, #5, #6, #7 yielded a limited dilation with only a total volumetric strain of 0.8 % at 500 kPa of effective stress and less than 1.5 % at 100 kPa of effective stress. However, the oil sand core in Test #2 yielded even less volumetric strain at the same level of effective stress, compared with a water-wet sand core. It is important to note that the curves of volumetric strain versus effective stress closely overlap each other for all four tests on the water-wet sand core. It indicates all core specimens possess consistent properties with almost identical porosity.

As can be seen, the volumetric strains display minimal nonlinearity with effective horizontal stress in this series of tests under an initial isotropic stress state. Through the measurement of absolute permeability for a water-wet sand core and effective permeability to water for an oil sands core, the volumetric strain trend is reversible with stress states for both sand core specimens under an initial isotropic stress state. It means that the permeability, which increased due to water injection in a sand core, will return to its initial value once the pore pressure drops to the initial state. Based on this observation, Core #7 was reconsolidated as an initial anisotropic stress state for Test #3 after it was completed in Test #3, and Core #3 was reconsolidated in the same manner in Test #4 and Test #5.

The deviatoric stress is plotted against the mean effective stress in Figure 4-3, which is the stress path followed along during Test #2. Other tests followed along the similar stress paths as Figure 4-3. It is obvious that the deviatoric stress is close to zero, indicating the axial stresses were nearly equal to the confining pressure during water injection under initial isotropic stress. When the mean stress decreases with water injection, the core specimen has a slight dilation and consequently, the modest increase in the cross-sectional area of the specimen results in a small decrease in axial stresses. The confining pressure remains constant during the test.

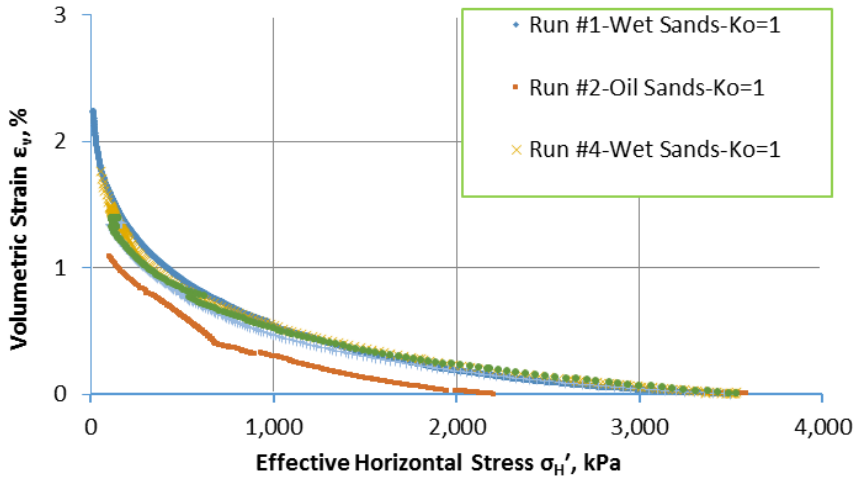

Figure 4-2. Comparison of volumetric strain with effective confining stress during water injection under initial isotropic stress conditions

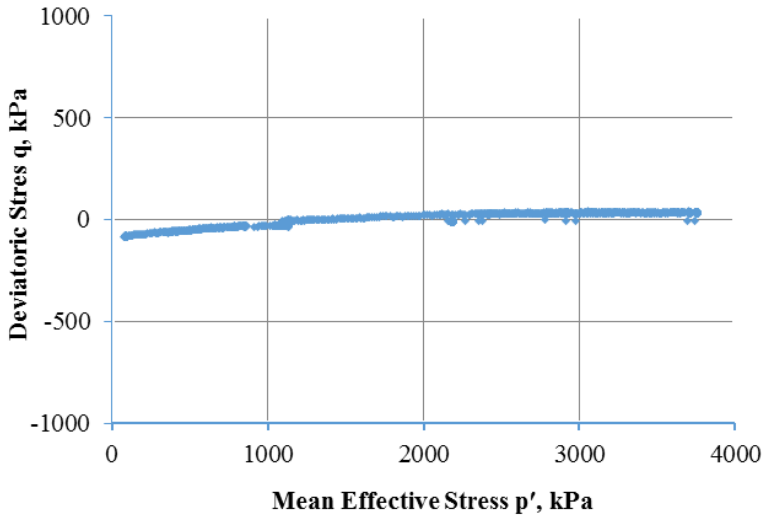

Figure 4-3. Effective stress during pore injection in test #2 under isotropic stress state (K_o=1)

Regarding the impact of bitumen on the volumetric change during cold-water injection, the pressure differentials across the length of the core specimen contribute to the lags for the bitumen-saturated specimen as shown in Figure 4-2. Due to the extremely high viscosity of bitumen, the dispersion of pore pressure presents retardation or delay from the injection port to the farthest one. The average pressures of injection at the bottom and top port overestimate the real pressure in the middle section, which results in a bigger increase than that observed in a brine-saturated core specimen with the same amount of water injected. The pore pressure does not increase linearly along the core length. If cold-water is injected at an extremely low rate, the impact of the differential pressures along the length of the core specimen could be minimized in this set of tests.

4.1.3. Geomechanical Response under Initial Anisotropic Stress State

To examine the effects of initial anisotropic stress, both water-wet and oil sands cores were tested under an initial anisotropic stress state with a stress ratio of 0.5. Test #3 and Test #5 were prepared and conducted to verify the interaction between geomechanical dilation and multiple phase fluid behaviours of a specimen under an initial anisotropic stress state. Test #3 examines the behaviours of an oil sands core while Test #5 examines those of a water-wet sand core. The volumetric strains are plotted versus the effective confining pressure in Figure 4-4.

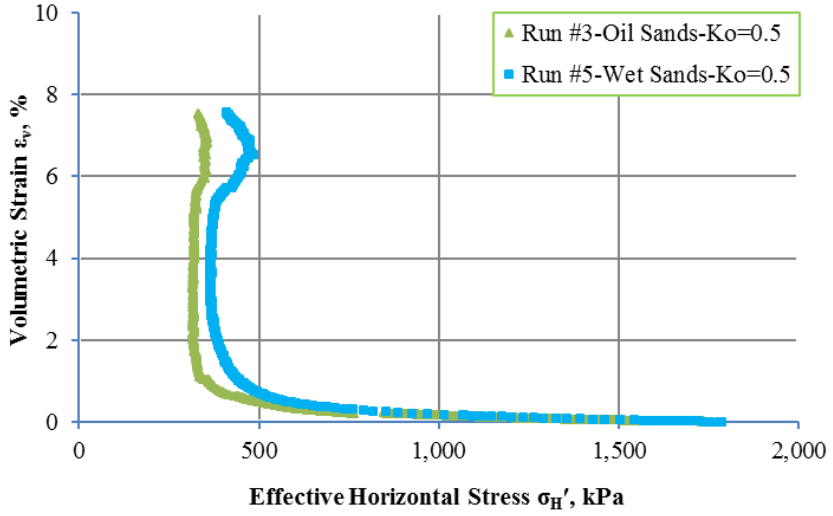

Figure 4-4. Comparison of effects of different fluid-saturated in a specimen on the volumetric strain with effective stress during water injection in Test #3 on oil sands & Test #5 on water-wet sands

It can be seen in Figure 4-4 that the volumetric change increased almost linearly when the effective stress decreased at the beginning of the water injection. However, as a result of the pore pressure increase, the stress ratio (σ_1'/σ_3' or q/p') continuously increases and ultimately leads to shearing failure within the specimen. For the tests shown in Figure 4-4, the volumetric strains exhibited a dramatic increase when the effective horizontal stress (σ_3') dropped below 400 kPa for the water-wet sand specimen in Test #5 and 300 kPa for oil sands specimen in Test #3.

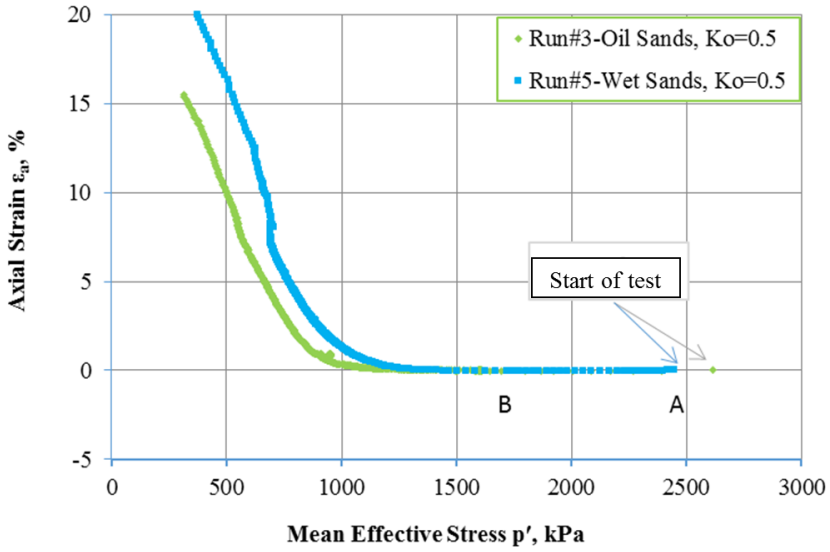

Figure 4-5. Axial strains versus effective mean stress during water injection in Test #3 on oil sands and Test #5 on water-wet sands

Figure 4-4 shows a large dilation of the samples with a total volume increase of 7.6 % at the horizontal effective stress of 320 kPa for the oil sands core and 360 kPa for the clean sands core. A dramatic and permanent increase of effective permeability to water was also observed by Wang et al. (2015) for the oil sands core in Test #3. Both specimens yielded large volumetric strains at failure points. Testing was concluded after a 7.6% volumetric strain due to the limitation of sleeve length and radial LVDT range, as the volumetric strains would have kept increasing if water continued to be injected into the specimen.

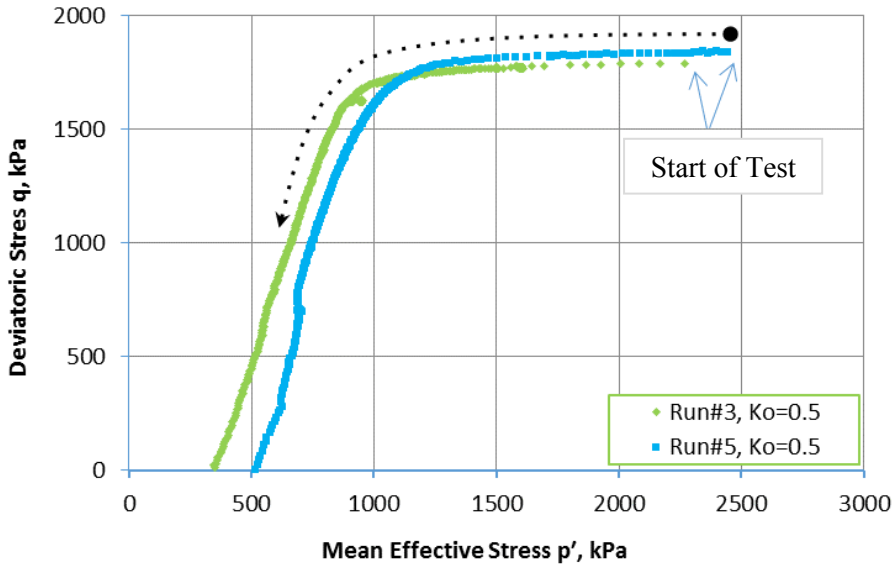

Figure 4-6. Effective stress paths during water injection in Test #3 on oil sands and Test #5 on water-wet sands

The axial strain and deviatoric stress are plotted against the mean stress in Figure 4-5 and Figure 4-6, respectively for Test #3 and Test #5. Figure 4-5 shows that the mean effective stress dropped, as expected, with the increased pore pressure. A very slight extension (~ 0.02%) of the axial strain occurred over the stress path from point A to B. However, for the remainder of the test, both water-wet and oil sands specimens underwent compressive axial strains with decreasing mean effective stress.

4.1.4. Effects of Fluid Saturation on Geomechanical Response

This series of the triaxial test compared the behaviours of brine-saturated and bitumen-saturated cores. Figure 4-2 and Figure 4-4 identify some differences and similarities in terms of volumetric strain versus effective stress. The higher volumetric strain was attained with the brine-saturated core than the oil-saturated core at the same effective stress level, as shown in Figure 4-2. The brine-saturated core generated large plastic strains or reached failure state at lower effective stress than the oil-saturated core.

4.1.5. Effects of Pore Pressure on Geomechanical Response

The dilation test results for two different starting pore pressures of 5.0 MPa in Test #6 and 2.0 MPa in Test #7 are illustrated in Figure 4-7 and Figure 4-8, where volumetric strains are plotted against pore pressure and effective confining pressure, respectively. In Test# 7, pore pressure of 2.0 MPa, vertical stress of 2.1 MPa and a horizontal pressure of 2.1 MPa were applied and left overnight for thawing and re-saturation.

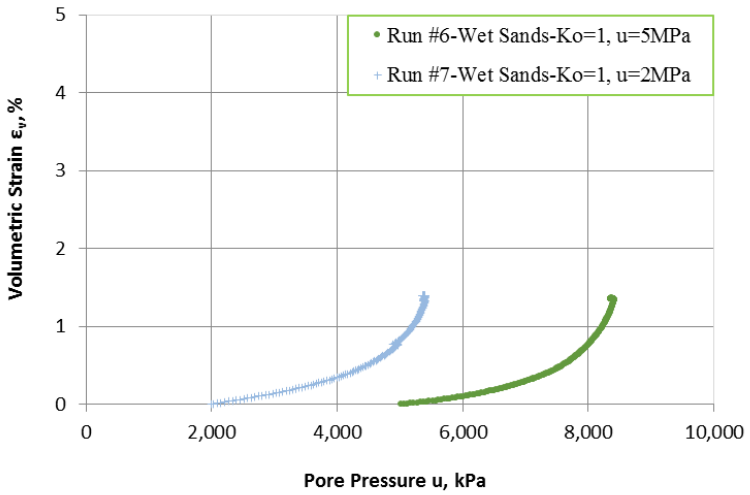

Figure 4-7. Comparison of effects of different pore pressure on volumetric strain during water injection in Test #6 & Test #7

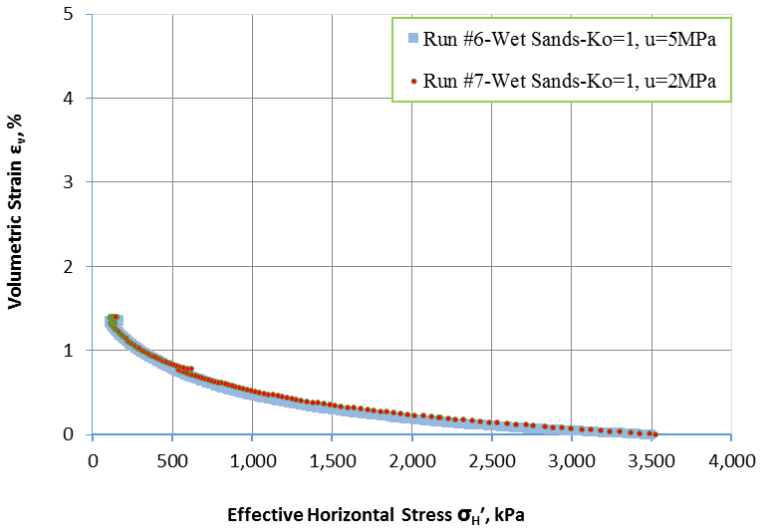

Figure 4-8. Comparison of volumetric strain with the same effective but different pore pressure during water injection in Test #6 & Test #7

Figure 4-8 shows that a core sample achieves the same volumetric strains if it is loaded with the same effective stress level. Both tests performed nearly identical and yielded similar volumetric strains under an initial isotropic stress state. It shows that the effective stress dominates the volumetric strains rather than absolute pore pressure.

4.2.Multiphase Flow Behaviours Due to Cold-water Injection

One enhanced SAGD (Steam-Assisted Gravity Drainage) start-up scheme (Abbate *et al.*, 2013, 2014) has recently been proposed and deployed in a pilot SAGD well pad to shorten SAGD start-up operation time. This accelerated start-up scheme is related to pore pressure injection, which is expected to create a dilation zone vertically connecting two horizontal wells. This dilation zone is expected to increase porosity, effective permeability to water, and water mobility in the inter-well region. There have been several publications on permeability variation associated with shear-induced in unconsolidated sands through a series of triaxial tests (Dusseault, 1977; Agar, 1984; Kosar, 1989; Wong, Barr and Kry, 1993; Oldakowski, 1994; Scott, Proskin and Adhikary, 1994; Touhidi-Baghini, 1998; Khan, 2009).

Most of these studies are conducted through triaxial tests with the following stress path: maintaining confining stress while increasing axial or vertical stress to induce shearing failure. In general, such tests are designed and intended to simulate the stress variation, such as triaxial compression and a radial extension, during the thermal recovery process. They may not fully represent the stress path and deformation that oil sands reservoirs undergo during fluid injection. Yale studied field oil sands samples with interbedded mudstone under fluid injection (Yale, Mayer and Wang, 2010). The triaxial tests were carried out at room temperature under a reservoir boundary condition with only modest levels of stress anisotropy (stress ratio 1.1).

While some geomechanical responses such as volumetric changes associated with in-situ bitumen extraction operations are recognized, it remains unclear how to correlate between volumetric changes and pore pressure increase under the in-situ reservoir conditions in terms of pore pressure, stress state, and reservoir temperature. Laboratory experiments and field practices have not been sufficiently comprehensive to define the physical conditions under which the dilation enhancement scheme is the most effective and feasible to field operation.

This part of the research study aims to understand the mechanism of geomechanical response and multiple phase behaviour during the cold-water injection. A representative core considered as an element of the injection well and the production well was assessed in terms of multiple-phase fluid behaviours during isotropic and anisotropic stress states. A test was carried on both high quality and lower quality (high water content) oil sands specimens by following a specific reservoir stress path.

4.2.1. Measurement Procedure and Boundary Conditions

The procedures for the permeability measurement conducted in a triaxial cell apparatus during geomechanical dilation are similar to those executed in the case of the triaxial compression tests. They mainly include specimen preparation, fluid saturation, consolidation, and geomechanical dilation test. The absolute permeability measurement is conducted in a bitumen-free sands specimen. Due to the same sand-packing methods for both oil sands and bitumen free core specimens, the basic mechanical properties of these core specimens are almost identical, in terms of porosity, dry density, and particle size distribution. The absolute permeability measured from a bitumen-free specimen is expected to be well representative of the other core specimens, which are saturated with either bitumen or water only.

The permeability is first measured by the end of consolidation, which included the effective permeability and the absolute permeability. After consolidation, the stresses are decreased until low effective stress of 50 kPa is reached. Throughout this process, a small pressure gradient between the top and the bottom of the specimen is maintained and monitored by a differential pressure transducer. The flow rate through the specimen is recorded with Quizix pumps. The pressures are changed in steps. At each step, after volumetric changes and flow rates have stabilized, the flow rates and pressure gradients are recorded and later used for the permeability calculations. The detailed procedure of sands preparation, specimen installation, and core consolidation to establish in-situ conditions in terms of pore pressure, stress, and temperature can be found in the previous Section 3.2.3**.**

The permeability tests under the anisotropic stress conditions follow similar procedures as those under isotropic stress conditions. They are measured at the predetermined stress level. In this study, the permeability is to be measured and assessed when 100%, 75%, 50%, 25 %, and 5% of initial effective stress reach, respectively. In the case of the anisotropic stress state, the initial axial stress is set at a value that is approximately equal to the value of the vertical stress. The ratio of vertical and minimum effective principal stresses is equal to the predetermined stress ratio, for example, 2.0 or 0.5. During this geomechanical dilation experiment, while pore pressure was increased in very slow stages, the vertical total stress was kept unchanged until specimen failure occurred. After the failure, the vertical stress decreased while the sample deformed with each additional increase in pore pressure. The permeability measurement under the conditions of the geomechanical dilation also followed a similar procedure.

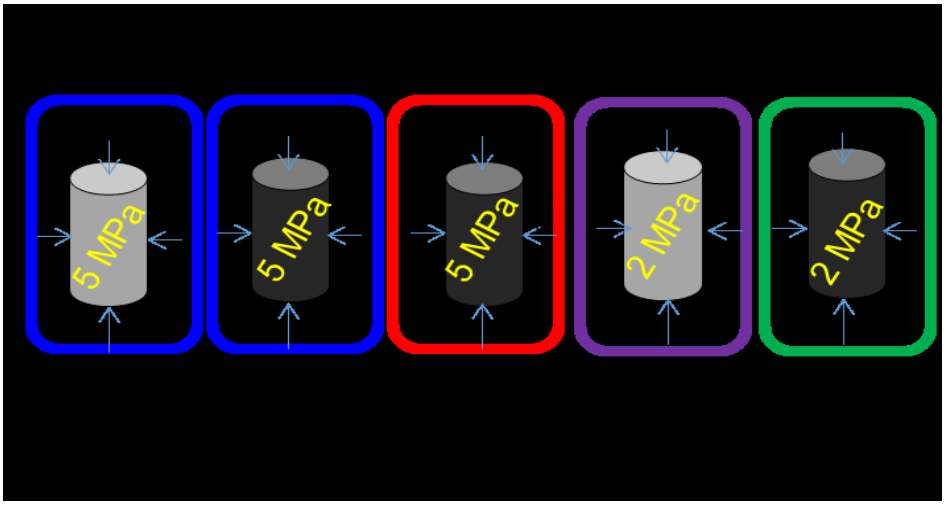

Core#2 Core#7 Core#7 Core#11 Core#8

Figure 4-9. Boundary conditions of three tests on dilation due to pore pressure injection (grey colour indicates brine saturated specimen and black colour indicates bitumen saturated specimen)

Five test results are summarized to assess the multiphase flow behaviour under geomechanical dilation associated with three types of stress conditions, as shown in Figure 4-9. Test #1 (sample 2, a water-saturated sand core) and Test #2 (sample 7, a bitumen saturated, water-wet sand core) were carried out under an initial isotropic stress of 3.5 MPa. Both horizontal effective stress and vertical effective stress were maintained at 3.5 MPa during pore pressure injection.

Test #3 used core sample 7, which was saturated with bitumen. It was conducted for pore pressure injection under an anisotropic stress condition. The stress ratio, the effective horizontal stress over the vertical one, was 0.5. In the test, 1.75 MPa of the horizontal effective stress and 3.5 MPa of the vertical effective stress were applied.

Test #8 (core sample 11, a water-saturated sand core) was carried out under an anisotropic initial stress condition. A stress ratio of 2 was applied, where 7.0 MPa of the horizontal effective stress and 3.5 MPa of the vertical effective stress were maintained during pore pressure injection.

Table 4-2. Petrophysical Properties of Cores Used in the Triaxial Tests

Test Number	Sand Core Tag	Bulk Volume (cm^3)	Mass of Core (g)	Initial Porosity (%)	Relative Density (%)	Initial Water Saturation (%)	Initial Bitumen Saturation (%)
#1	Core #2	407.4	812.3	34.2	221.6	100.0	0.0
#2 & 3	Core #7	395.7	824.0	32.3	246.2	13.8	86.2
#8	Core #11	408.7	831.9	32.2	247.8	100.0	0.0
#9	Core #8	398.5	843.1	32.3	246.2	85.4	14.6

Test #9 (core sample 8, a bitumen-saturated sand core) was carried out under the same stress condition as in Test #8.

The properties of sands core are listed in the following table in terms of the size, weight, density, porosity, and fluid saturation of the sands cores.

4.2.2. Permeability Variation under Initial Isotropic Stresses

Test #1 was conducted for a brine saturated specimen core #2 under initial isotropic stress conditions. At the end of isotropic consolidation, an absolute permeability of approximately 150 millidarcys (mD) was measured, where the maximum and the minimum effective stresses were held at 3500 kPa. The pore pressure increased with water injection at an ambient temperature of 22 °C and effective stress decreased. When the effective stresses reached 75 % of the initial effective stresses of 3500 kPa, which was 2625 kPa of the maximum and the minimum effective stresses, the permeability had a slight decline.

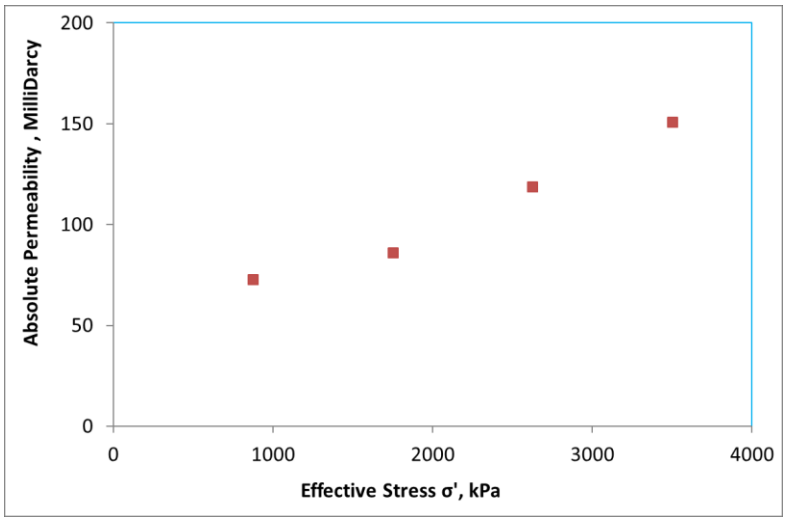

Figure 4-10. Absolute permeability variation during water injection in Test #1 using sands core saturated with brine under isotropic stress state at an ambient temperature of 22°C

The permeability was measured again after more water was injected, where the effective stress has reached 50 % and 25 % of the initial effective stresses of 3500kPa, which were

1750 kPa and 875 kPa, respectively. Figure 4-10 shows a nearly linear decrease in absolute permeability with decreasing effective stress during water injection (increase in pore pressure).

The core specimen in Test #2 had similar petrophysical properties as the one in Test #1, except that it was initially saturated with bitumen. In this case, the flow of brine into the specimen provided a measure of the effective permeability to brine since the bitumen phase was essentially immobile (i.e. viscosity ~ 3 x 10^6 cP at 8°C of operation temperature). For Test #2, the effective permeability to water measured at the end of isotropic consolidation was approximately 6 microdarcys (μD).

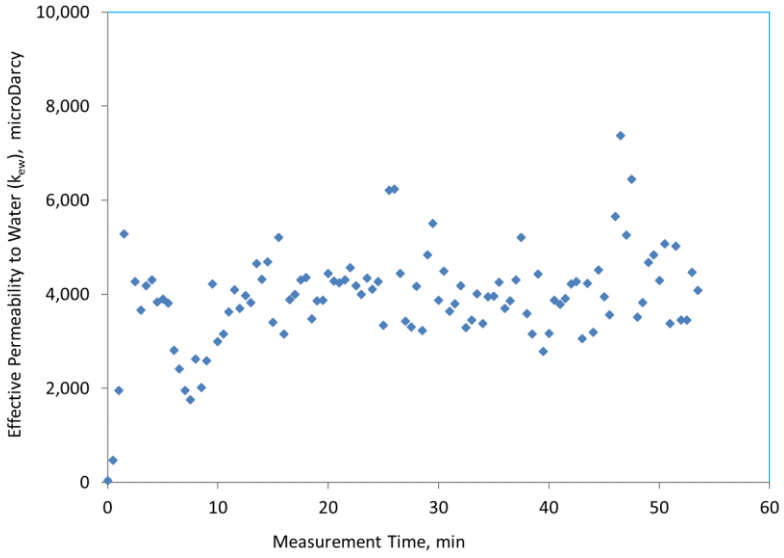

Figure 4-11. Effective permeability to water at the end of injection with pore pressure u= 8.1 MPa, confinement stress $\boldsymbol{\sigma_2 = \sigma_3}$=8.5 MPa and vertical stress $\boldsymbol{\sigma_1}$=8.5 MPa in Test #2

After a long time period (~100 hours) of water injection, both the effective horizontal and vertical stresses dropped to around 400 kPa, which were associated with a pore pressure increase to approximately 8.1 MPa. The effective permeability to water increased significantly at this point to approximately 4,000 μD, as shown in Figure 4-11. However, when the pore pressure was withdrawn back to the initial

state of 5.0 MPa, the effective permeability to water returned to its original value of 6 μD, clearly indicating that the permeability gain was not permanent.

4.2.3. Permeability Variation under Initial Anisotropic Stresses

For accelerated start-up processes in bitumen saturated oil sands, it is important for any permeability changes induced during cold-water injection to be permanent once the injection period is ended. Therefore, Test #3 was conducted to examine whether permanent permeability enhancement can be induced for initial anisotropic stress states. As shown in Test #2, a specimen under isotropic stress state was almost "reversible" in terms of porosity and effective permeability to water, over the water injection (pore pressure injection) stress path. Also, as shown in Figure 4-2, the volumetric strains also illustrate minimal nonlinearity with effective horizontal stress.

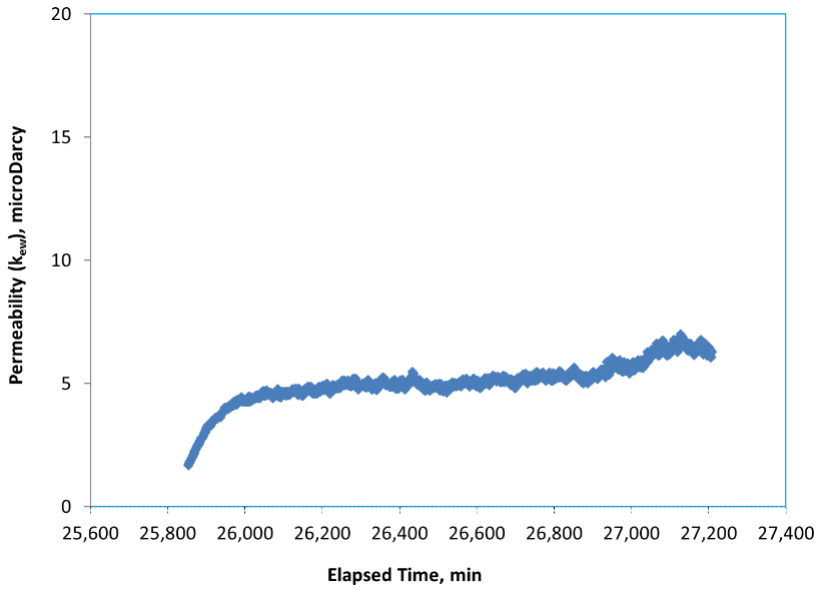

Figure 4-12. Effective permeability to water measured at the end of anisotropic stress consolidation, where pore pressure u=5.0 MPa, confinement stress $\boldsymbol{\sigma_2 = \sigma_3}$= 6.75 MPa, vertical stress $\boldsymbol{\sigma_1}$= 8.5 MPa, in Test #3

For Test #3, oil sand specimen Core #7 was reconsolidated to an initial anisotropic stress state. The effective permeability to water at the end of anisotropic

consolidation was measured to be approximately 6 μD, which is shown in Figure 4-12. The value of the effective permeability to water was close to one measured at the end of isotropic consolidation.

With the increasing pore pressure during water injection, the effective stress is assumed to decrease uniformly along with the entire core.

The variation of the effective permeability to water is shown in Figure 4-13. It can be noted that the effective permeability gradually increased and then dramatically jumped to high values when the effective stresses were approaching 50% of the initial effective stresses, where pore pressure was approximately 6.0 MPa, the confinement pressure was 6.75 MPa, and the vertical stress was 8.5 MPa.

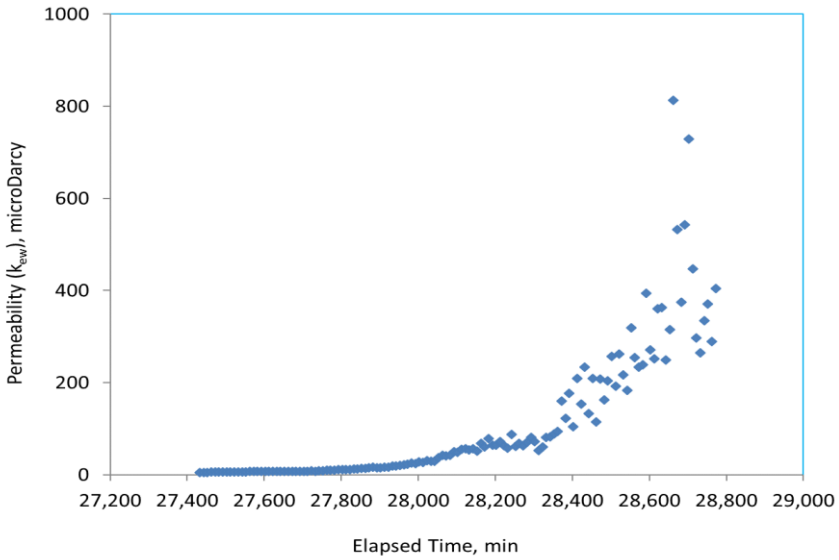

Figure 4-13. Effective permeability to water at the end of anisotropic consolidation, where pore pressure u=6.0 MPa, confinement stress $\boldsymbol{\sigma_2 = \sigma_3}$= 6.75 MPa, vertical stress $\boldsymbol{\sigma_1}$= 8.5 MPa, in Test #3 on an oil sands specimen

Eventually, it increased up to 5000 μD at the end of water injection where the effective horizontal stress was around 400 kPa, shown in Figure 4-14. The test results indicated that there was a significant improvement in effective permeability to water at the end of water injection.

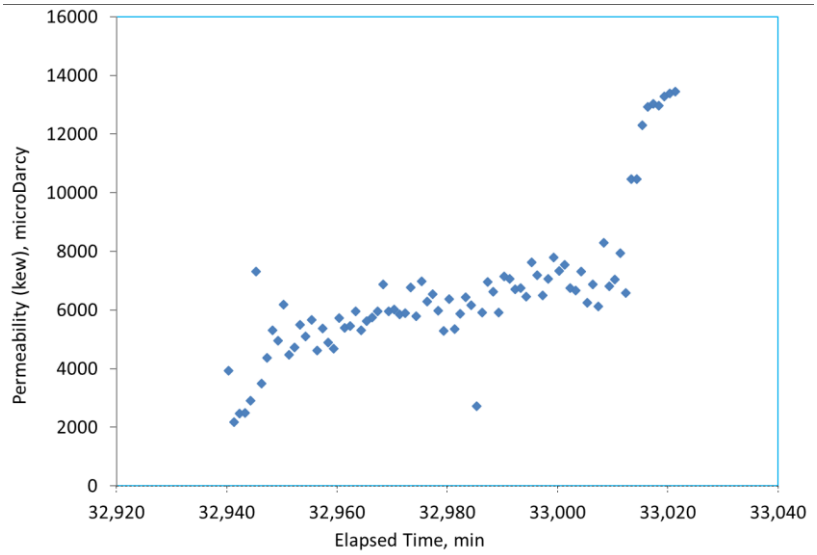

Figure 4-14. Effective permeability to water when the pore pressure was raised to 6.5 MPa at the end of cold-water injection. Confinement stress $\boldsymbol{\sigma_2 = \sigma_3}$= 6.75 MPa, vertical stress $\boldsymbol{\sigma_1}$= 8.5 MPa, in Test #3 on an oil sands specimen

Most importantly, however, the effective permeability to water dropped only slightly and maintained at a constant value of approximately 4000 μD, when the pore pressure was dropped to its initial value of 5.0 MPa, as shown in Figure 4-15. It indicates that the permanent enhancement of permeability was achieved through water injection.

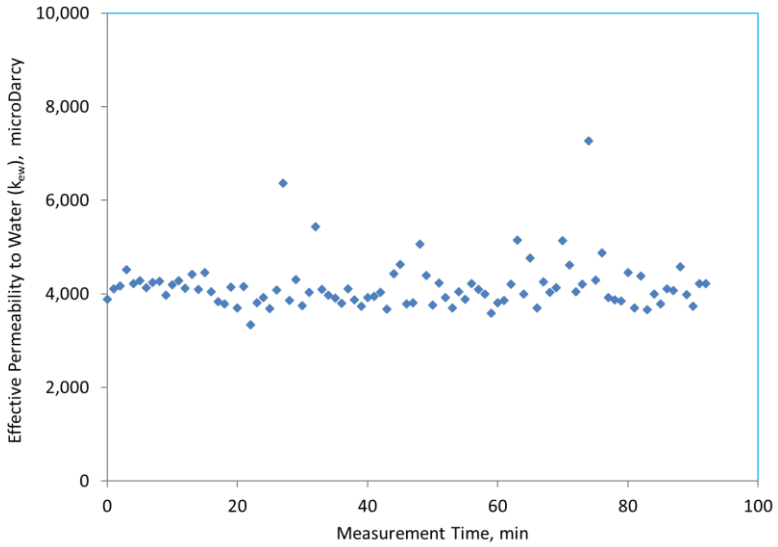

Figure 4-15. Effective permeability to water when the pore pressure was drawn back to the initial value (5.0 MPa), after cold-water injection. Pore pressure u= 5.0 MPa, confinement pressure $\boldsymbol{\sigma_2 = \sigma_3}$= 6.75 MPa, vertical stress $\boldsymbol{\sigma_1}$ = 8.5 MPa, in Test #3 on an oil sands specimen

As noted above, Test# 3 was tested to examine the variation of the effective permeability to water under an anisotropy stress state, where the stress ratio is 0.5, the initial effective horizontal stress over the initial effective vertical stress. Test #8 and #9 were designed to examine the variation of the effective permeability to water under a different stress ratio greater than 1.0, where the initial effective horizontal stress was greater than the initial effective vertical stress.

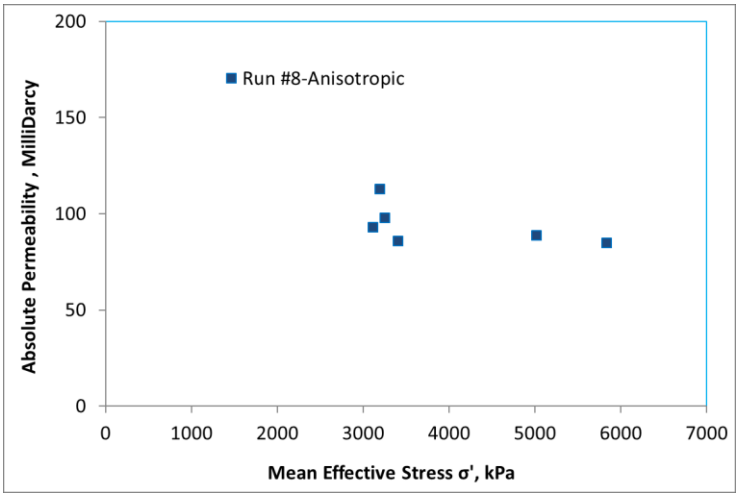

Figure 4-16. Absolute permeability variation during cold-water (9°C) injection under anisotropic stress state (k_o=2) in Test #8 using sands core saturated with brine; Pore pressure u= 2.0 MPa, confinement pressure $\boldsymbol{\sigma_1 = \sigma_2}$= 9.0 MPa, vertical stress $\boldsymbol{\sigma_3}$ = 5.5 MPa,

Test# 8 was carried on the measurement of absolute permeability variation during cold-water (9°C) injection under an anisotropic stress state (k_o=2) using the sands core saturated with brine. The oil sand specimen Core #11 was reconsolidated to an initial anisotropic stress state. The absolute permeability at the end of anisotropic consolidation was then measured, which is shown in Figure 4-16.

Based on the test results on a water-saturated sands core specimen in Test# 8, the absolute permeability had a slight change when the effective stress decrease during water injection, which can be noted in Figure 4-16. The absolute permeability of the sands core was measured at around 85 millidarcies before water injection when the mean effective stress was 5800 kPa. During the cold-water injection, the absolute permeability remained unchanged until the effective mean stress decreased to 3200 kPa. Then, the absolute permeability was measured with a minor increase from 80 millidarcies to 110 millidarcies.

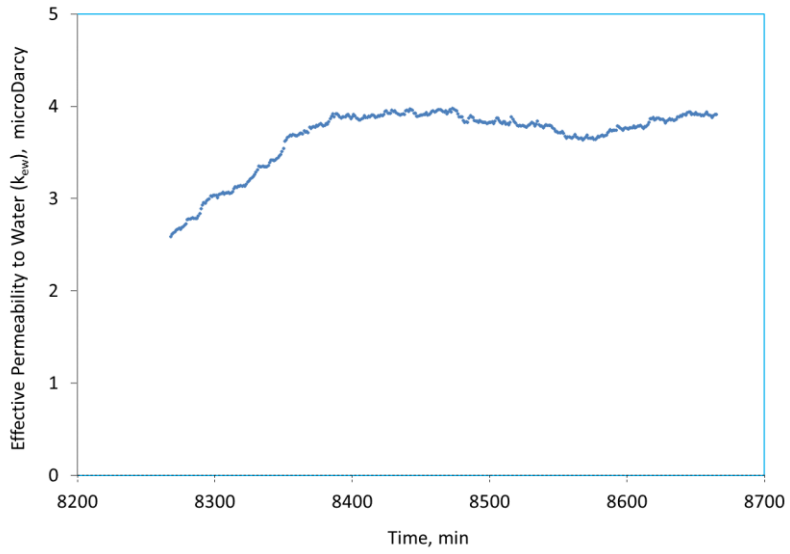

Figure 4-17. Effective permeability to water starting at the end of consolidation, after which pore pressure rose from 2.2MPa to 2.7 MPa, confinement pressure=9.0MPa, vertical stress=5.7MPa under anisotropic stress state (k_o=2) in Test #9 on oil sands specimen

After the oils sands specimens were consolidated under an anisotropic stress state, cold-water was injected at a relatively low rate (0.05ml/hr). The pore pressure gradually rose from 2.2MPa to 2.7 MPa, while the confinement pressure and vertical stress maintained at 9.0MPa and 5.6MPa, respectively. The effective permeability to water was measured and shown in Figure 4-17. It can be noted that the effective permeability remained unchanged with the elapsed time and decreasing mean effective stress. During this injection time, both the effective confinement (horizontal) stress and the effective axial (vertical) stress decreased with the increased pore pressure. It is obvious that if the core specimens experienced inelastic strain, the corresponding effective permeability exhibited limited variation during this period.

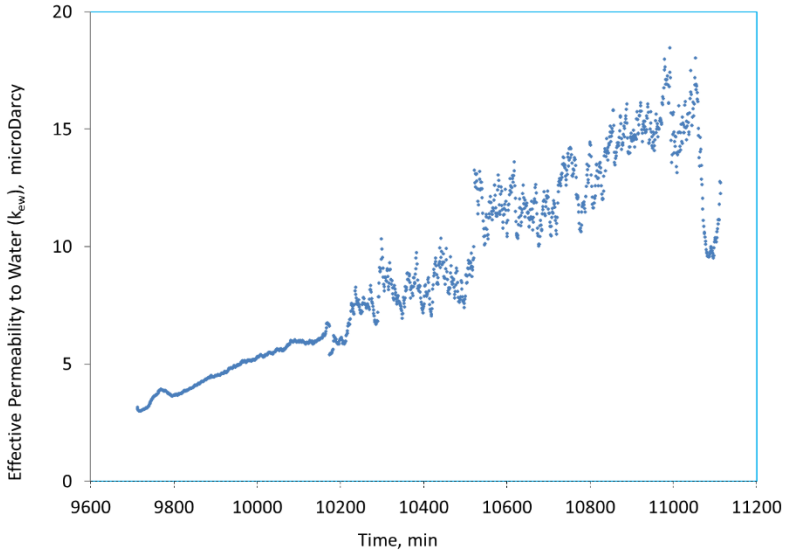

Figure 4-18. Effective permeability to water during the first cycle of pore pressure injection, where pore pressure rose from 4.0 MPa to 4.4 MPa, confinement pressure=9.0MPa, vertical stress=5.7MPa under anisotropic stress state (k_o=2) in Test #9 on oil sands specimen

With cold-water injection continuing, the effective stresses decreased slowly when the pore pressure kept rising. The effective permeability to water was nearly linear increasing from 5 microdarcies to 18 microdarcies when the effective confinement (horizontal) stress dropped from 5.1 to 4.6 MPa, and the effective axial (vertical) stress dropped from 1.8 to 1.3MPa. The variation of the effective permeability versus elapsed time was plotted in Figure 4-18 and Figure 4-19. It can be noted that the effective permeability to water was modestly non-linear with decreasing mean effective stress.

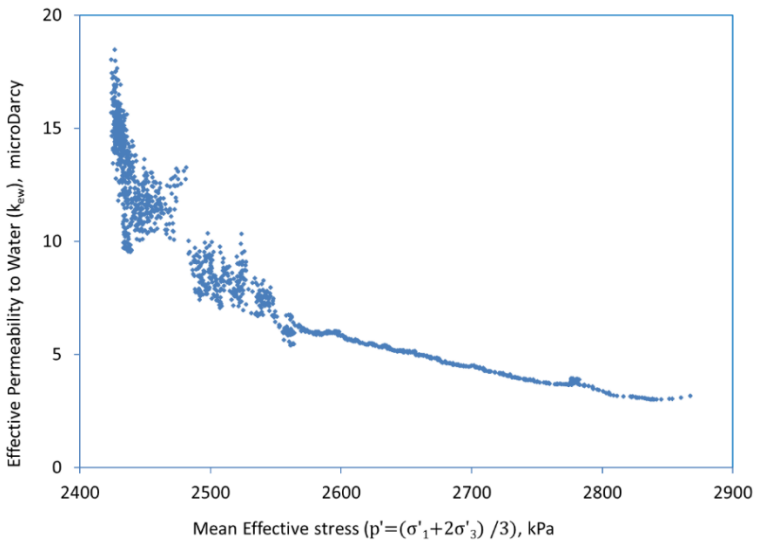

Figure 4-19. Effective permeability to water during the first cycle of pore pressure injection while the pore pressure increased to 4.4 MPa from 4.0 MPa, confinement pressure dropped from 5.1 to 4.6 MPa, vertical stress from 1.8 to 1.3MPa under anisotropic stress state (k_o=2) in Test #9 on oil sands specimen

With more water penetrating the core specimen, the porosity of the core specimen increased gradually, though it increased slightly during this injection span. Figure 4-20 depicts the relationship between the effective permeability to water and the porosity of the core specimen. It can be noted that the effective permeability to water increased modestly in a linear fashion with the increasing porosity of the core plug. The porosity was calculated based on the cumulative amount of water injected. It was assumed to be uniform along the length of the core. Prior to geomechanical dilation, where the averaged porosity was less than 30.9%, the effective permeability to water varied in a very small range and there was little variation. However, upon the onset of dilation, the effective permeability to water increases dramatically.

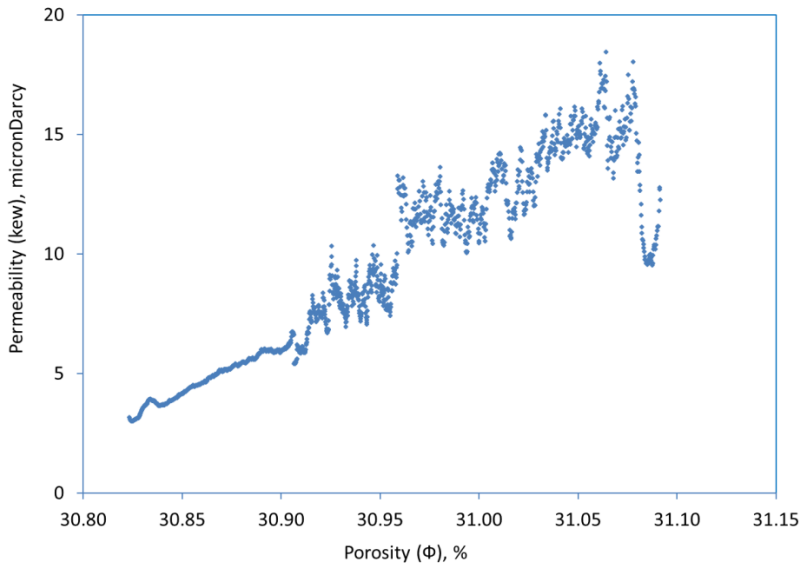

Figure 4-20. Effective permeability to water during the first cycle of pore pressure injection while the pore pressure increased to 4.4 MPa from 4.0 MPa, confinement pressure dropped from 5.1 to 4.6 MPa, vertical stress from 1.8 to 1.3MPa under anisotropic stress state (k_o=2) in Test #9 on oil sands specimen

It can be noted that the effective permeability to water had some degree of enhancement after the first cycle of water injection. A second cycle was repeated, where the pore pressure was brought down to 4.0 MPa from 4.4 MPa prior to commencing the second cycle of water injection. It can be noted in Figure 4-21 and In terms of the correlation between the effective permeability and the porosity variation during water injection, Figure 4-23 displays the increasing trends of the effective permeability versus the porosity of the core specimen. The effective permeability had reached its peak value of approximately 150 μD in the dilated zone with a corresponding porosity of 31.16%. The results seem to support the conclusion that a dramatic enhancement in the effective permeability to water is plausible when the core specimen sustained shearing failure and permanent dilation.

that the effective permeability to water was reduced to 8 μD and fluctuated slowly when the pore pressure started increasing, similar to what was observed during the first cycle of water injection as shown in Figure 4-18 and Figure 4-19. However, the effective permeability jumped to approximately 150 microdarcies in the second cycle, as opposed to the15 microdarcies in the first cycle at the same mean effective stress of 2420 kPa. It was almost 10 times higher than that in the first cycle of water injection.

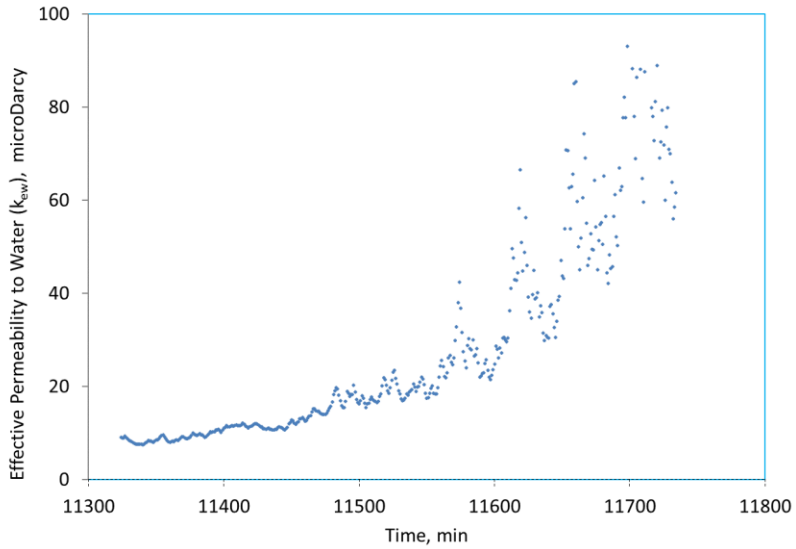

Figure 4-21. Effective permeability to water during the 2nd cycle of pore pressure injection while the pore pressure increased to 4.4 MPa from 4.0 MPa, the confinement pressure dropped from 5.1 to 4.6 MPa, vertical stress from 1.8 to 1.3MPa under anisotropic stress state (k_o=2) in Test #9 on oil sands specimen

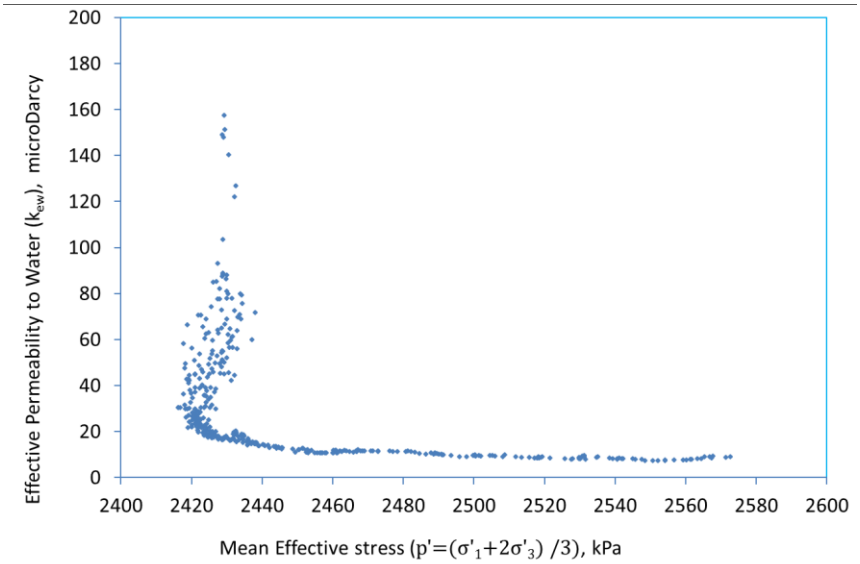

Figure 4-22. Effective permeability to water during the 2nd cycle of pore pressure injection while the pore pressure increased to 4.4 MPa from 4.0 MPa, while the confinement pressure dropped from 5.1 to 4.6 MPa, vertical stress from 1.8 to 1.3MPa under anisotropic stress state (k_o=2) in Test #9 on oil sands specimen

In terms of the correlation between the effective permeability and the porosity variation during water injection, Figure 4-23 displays the increasing trends of the effective permeability versus the porosity of the core specimen. The effective permeability had reached its peak value of approximately 150 μD in the dilated zone with a corresponding porosity of 31.16%. The results seem to support the conclusion that a dramatic enhancement in the effective permeability to water is plausible when the core specimen sustained shearing failure and permanent dilation.

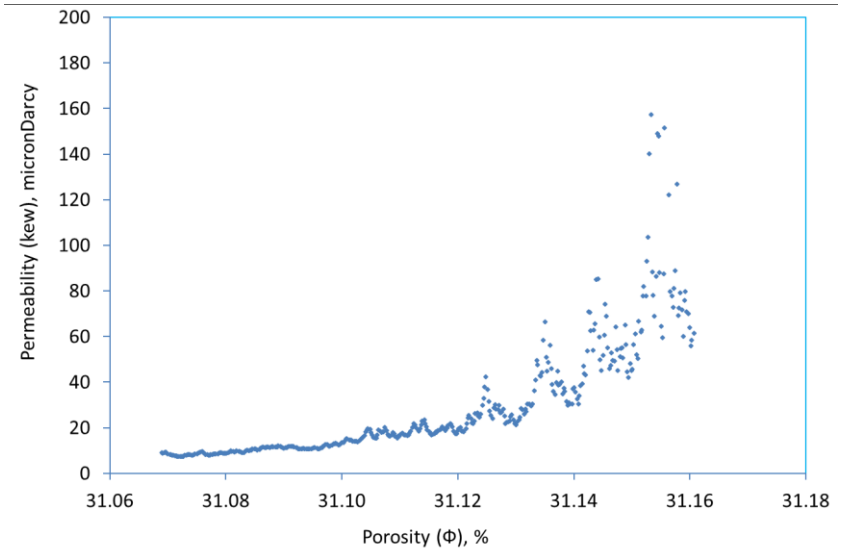

Figure 4-23. Effective permeability to water during the 2nd cycle of pore pressure injection while the pore pressure increased to 4.4 MPa from 4.0 MPa, while the confinement pressure dropped from 5.1 to 4.6 MPa, vertical stress from 1.8 to 1.3MPa in Test #9

4.2.4. Discussion of Experimental Findings & Results of Permeability Variation with Geomechanical Dilation

A set of the triaxial experimental tests has been conducted to evaluate the geomechanical dilation in very dense, reconstituted water-wet and bitumen sand specimens for a pore pressure injection.

A representative core, which was considered as an element between the injection well and the production well, was assessed in terms of multiple-phase fluid behaviours during isotropic and anisotropic stress states. The experimental results demonstrated that a dilation zone could be created through pore pressure injection. All tests were carried on both water-wet and bitumen sands specimens by following a specific reservoir stress path.

Under initial isotropic stress states, the dense sand specimens (water or bitumen saturated) yielded non-permanent or reversible volume changes (porosity). Meanwhile, little to no changes occurred in the absolute permeability for a water-

wet sand core, and in the effective permeability to water for an oil sands core. Under the isotropic initial stress states, the relationship between volumetric strain and effective stress was only modestly non-linear. Through the measurement of absolute permeability for a water-wet sand core and effective permeability to water for an oil sands core, it was concluded that initial isotropic stress states provide only a temporary improvement on permeability, which returned to the original measured value once the injection is stopped.

Under an initial anisotropic stress state (K_o = 0.5), the volumetric strain remains relatively small, matching the volume changes for the isotropic case closely, until the shear failure point is reached. At this point, the samples undergo a dramatic increase in volume strain and clearly demonstrate the potential to permanently enhance the porosity in a dilated zone, which results in permanent effective permeability enhancement.

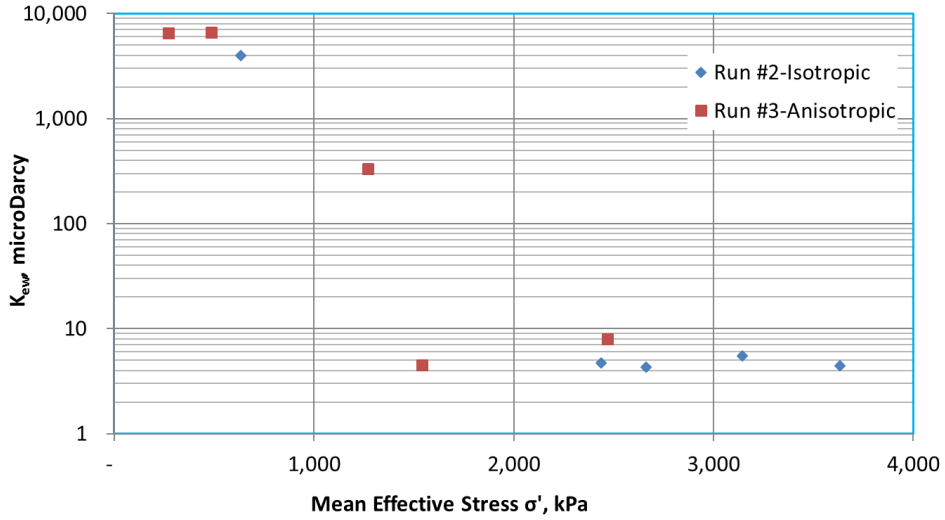

Figure 4-24. Effective permeability to water varying with mean effective stress during Injection in Test #2 under initial isotropic stress & test #3 under initial anisotropic stress state

Permeability variations are highly sensitive to stress state evolution along the pore pressure injection stress path. Temporary permeability enhancement is mainly attributed to the increase in porous volume achieved through pore pressure injection under isotropic stress states. Permanent permeability enhancement can only be achieved through pore pressure injection under initial anisotropic stress states. Experimental results show that the effective confining stress dominates the volumetric strains rather than absolute pore pressure.

Permeability change under pore pressure injection conditions was measured for isotropic and anisotropic initial stress states. For the isotropic stress conditions, three tests (Test #1, #4, and #7) were conducted on a brine-saturated specimen and one more test (Test #2) was conducted on a bitumen saturated specimen. Three tests (Test #5, #6, and #8) were conducted on a brine-saturated specimen and two more tests (Test #3 and #9) were conducted on a bitumen saturated specimen under the anisotropic stress conditions.

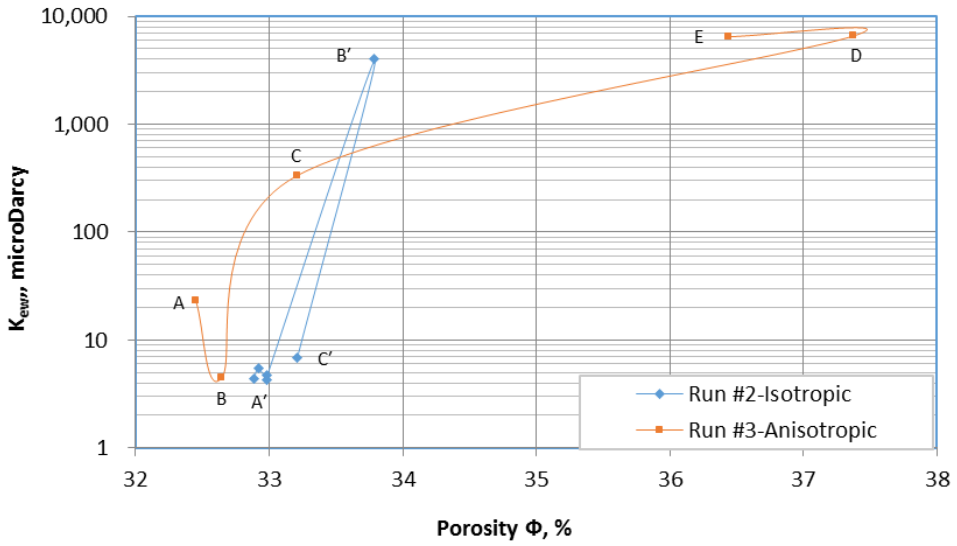

Figure 4-25. Effective permeability to water varying with porosity during injection in Test #2 under initial isotropic stress & Test #3 under initial anisotropic stress state

The experimental results for Test #1, #2, and #3, suggested a strong correlation between permeability enhancement and geomechanical dilation under initial stress state.

Figure 4-25 depicts the correlation between the effective permeability to water and porosity during pore pressure in Test #2 under initial isotropic stress and Test #3 under the initial anisotropic stress state. It intends to examine the intrinsic natures of McMurray Formation oil sands during geomechanical dilation due to pore pressure injection.

Point A′ represents the initial state at the end of isotropic consolidation and onset of water injection in Test #2, as shown in Figure 4-25. Similar values of effective permeability to water were recorded near point A′, where only slight changes in porosities were measured during the water injection phase in Test #2. The end of the water injection phase is marked as B′, where the effective permeability to water was enhanced dramatically corresponding to an increase in porosity from point A′ to point B′. As mentioned earlier, the porosity returned to the initial point A′ when the pore pressure was decreased to the initial state of 5.0 MPa.

The oil sands specimen was then anisotropically reconsolidated starting at the point C′ and ending at A. Then, the effective permeability to water was remeasured, which is shown as point A. The specimen experienced a decreasing porosity due to anisotropic reconsolidation. Starting from point A in Figure 4-25, water was injected and effective permeability was measured at elevated pore pressures. The effective permeabilities increased abruptly with the increasing porosities from point B to C and then to D. When the pore pressure was brought back to the initial pore pressure of 5.0 MPa, a slight decrease in porosity from 37.4% at point D to 36.3% at point E was observed. Meanwhile, there was no observable decrease in the effective permeability to water, suggesting that a permanent enhancement was achieved during water injection under the initial anisotropic stress state.

From the viewpoint of stress ratio, as shown in Figure 4-26, the effective permeability to water of the oil sands core sample is reversible when the stress ratio

increased from 0 to 0.8, and then back to 0 under initial isotropic stress state. However, during water injection at Test #3, the oil sands specimen experienced shearing failure and resulted in a significant increase of effective permeability to water when the stress ratio started from 0.75 at point A to point E.

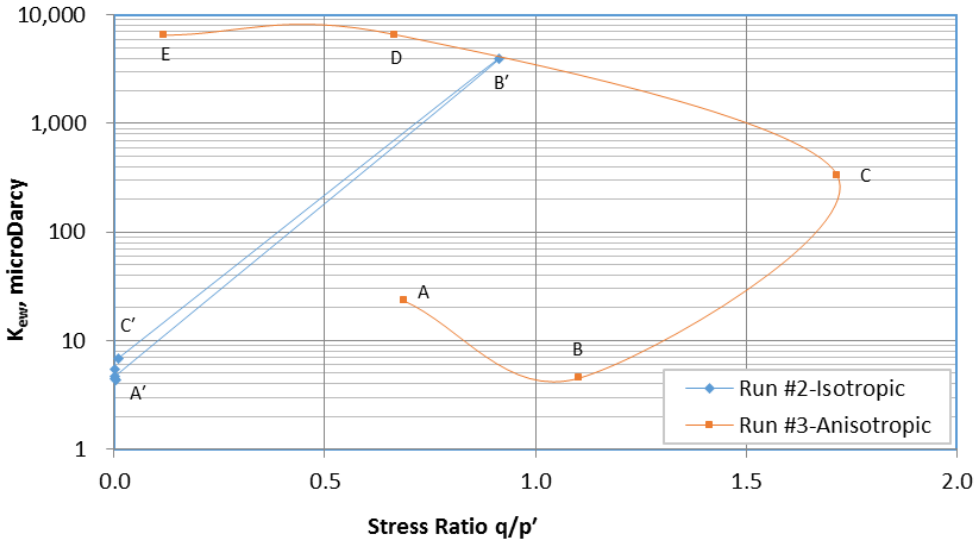

Figure 4-26. Correlations between effective permeability to water and stress ratio during injection in test #2 under initial isotropic stress & test #3 under initial anisotropic stress state

It can be noted that the effective permeability was only measured at elevated stress ratios. While the results of the test illustrated in Figure 4-26 suggest a q/p' failure ratio of 1.7, additional research is ongoing to confirm this as the peak shear strength point. These results clearly illustrate that permanent shear yield zones are required to produce permanent increases in effective fluid mobility with a bitumen-saturated specimen.

4.3.Critical Injection Pressure Based on Failure Envelopes

At the end of consolidation (point A for the case K_o<1 and point A' for the case K_o>1), water injection followed the horizontal paths, which are shown as green lines in Figure 4-27. The mean effective stress decreased due to the increase in pore pressure. The deviatoric stress can be determined by Eq. 4-1. When the mean effective stress approached the failure envelope lines at point B for the case K_o<1 and point B' for the case K_o>1, the specimen failed due to reaching the yielding strengths. The failure envelopes shown in black lines with functions in Figure 4-27 can be expressed as the following:

$$t = f(s') \qquad \text{Eq. 4-1}$$

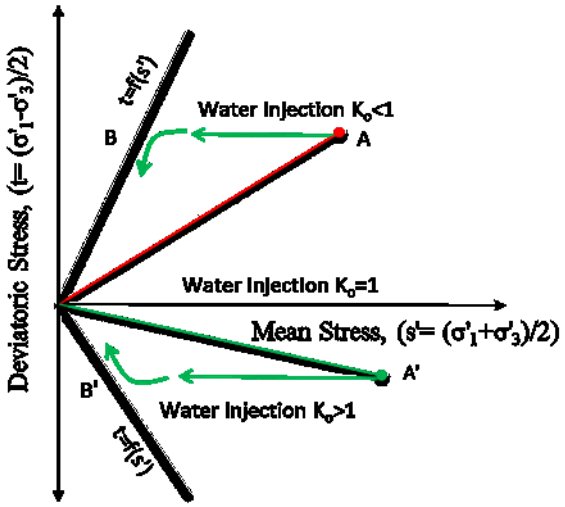

Figure 4-27. Stress paths and failure envelopes

The critical mean effective stress can be expressed by the following:

$$s' = \frac{\sigma_1' + \sigma_3'}{2} \qquad \text{Eq. 4-2}$$

and

$$u = \frac{\sigma_1 + \sigma_3}{2} - s' \qquad \text{Eq. 4-3}$$

Assume the failure envelopes can be simplified polynomial curves, and then Eq. 4-1 can be expressed as the following:

$$t_c = f(s_c') = a(s_c')^3 + b(s_c')^2 + cs_c' + d \qquad \text{Eq. 4-4}$$

where, a, b, c, d are independent constants. Then, the critical injection pressure can be estimated through the following expression:

$$u_c = \frac{\sigma_1 + \sigma_3}{2} - s_c' \qquad \text{Eq. 4-5}$$

The Mohr-Coulomb failure analysis for brine-saturated sand was conducted and obtained through a set of compression tests under a drained condition. The stress-strain relationships are plotted at three elevated effective stresses of 500, 1500, and 3500 kPa, respectively, as shown in Figure 4-28.

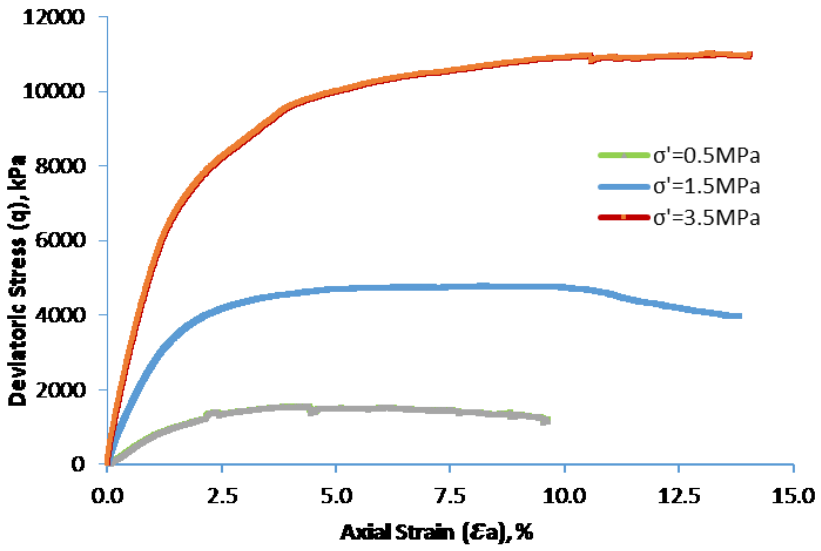

Figure 4-28. Deviatoric stress versus axial strain during compression (σ'=0.5, 1.5, 3.5 MPa, u=2 MPa)

The coordinates of the top points of the Mohr-Coulomb circles are drawn in Figure 4-29. The horizontal coordinate is defined as mean effective stress, which is equal to the mean stress between the maximum and the minimum effective stresses ($p'=(\sigma_1'+2\sigma_3')/3$). The vertical coordinate is equal to deviatoric stress ($q=\sigma'_1-\sigma'_3$). Using peak strength points of stress paths, Mohr-Coulomb circles are constructed, and the nonlinear Mohr-Coulomb failure envelope is fit to the circles at the blue lines in Figure 4-29.

Using experimental parameters from the set of triaxial tests on synthetic core specimens, an example is given to express an estimate of the critical injection pressure where the dramatic volumetric strain and effective permeability enhancement begin.

Based on a simple linear regression analysis of the measurement in the compression test, the failure envelopes can be expressed by the following equation:

$$t = -4 \times 10^{-6} \cdot (s')^2 + 0.8123(s') \qquad \text{Eq. 4-6}$$

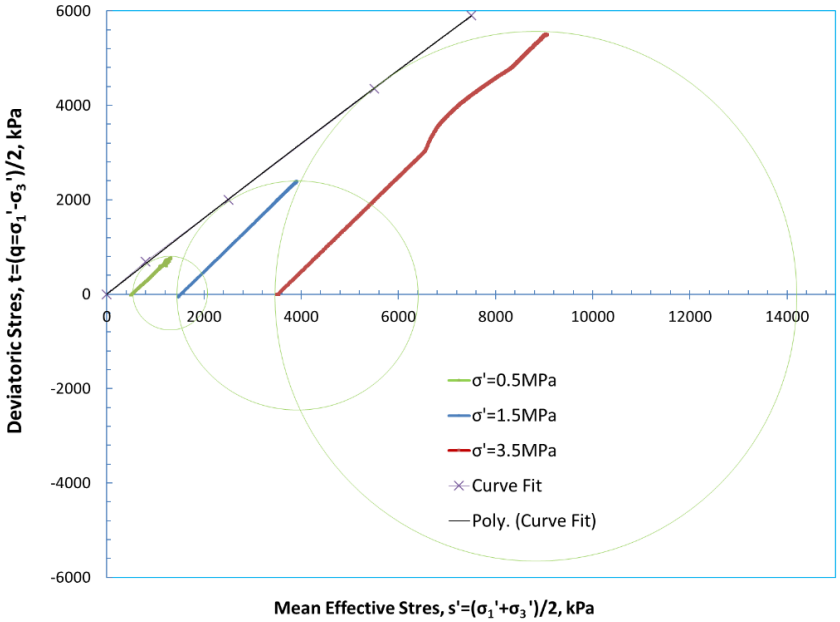

Figure 4-29. Mohr-Coulomb failure envelopes and deviatoric stress versus mean effective stress during compression (σ'=0.5, 1.5, 3.5 MPa, u=2 MPa),

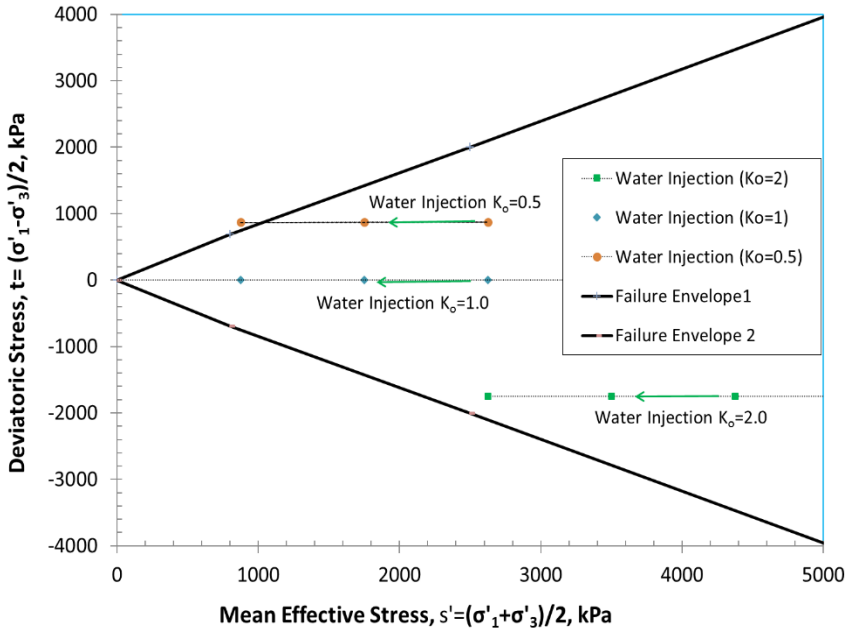

Figure 4-30. Stress path during consolidation and water injection under three stress ratios

During testing, axial stress and horizontal confinement pressure were maintained at 8.50 MPa and 6.75 MPa, respectively. The initial pore pressure was approximately 5.00 MPa. Assuming these confinement stresses were constant, the following applies:

$$\sigma_1 = 8.50\ MPa;\ \ \sigma_3 = 6.75\ MPa;\ u_i = 5.00 MPa \qquad \text{Eq. 4-7}$$

And,

$$\sigma_1' = 3.50\ MPa;\ \ \sigma_3' = 1.75\ MPa;\ k_o = 0.5 \qquad \text{Eq. 4-8}$$

Then, the failure envelopes are expressed as:

$$t = \frac{\sigma_1 - \sigma_3}{2} = 0.825 \text{ MPa} \qquad \text{Eq. 4-9}$$

According to Eq. 4-6, the mean effective stress (s') during the entire test can be easily calculated and obtained by the following equation:

$$s' = 1.016\ MPa = 1016\ kPa \qquad \text{Eq. 4-10}$$

Combined with the Mohr-Coulomb failure envelopes expressed in Eq. 4-1, the mean effective stress (s_c') at the failure point can be solved and determined:

$$s_c' = 1.016\ MPa = 1016\ kPa \qquad \text{Eq. 4-11}$$

Based on Eq. 4-11, the critical pore pressure at the failure point can be estimated with Eq. 4-12:

$$u_c = \frac{\sigma_1 + \sigma_3}{2} - s_c' = 6{,}609\ kPa \qquad \text{Eq. 4-12}$$

Obviously, the critical injection pressure (u_c) to yield shearing failure is less than the initial mean stress and the maximum principal stress. This indicates that it is not necessary to operate at a high injection pressure exceeding the maximum principal stress to achieve geomechanical dilation, provided that the deviatoric stress reaches

yielding strength. The critical injection pressure (u_c) could be estimated through the failure envelopes of the geomaterials in the formation.

4.4. Discussion

The investigation of the absolute permeability of oil sands was carried out using specimen cores #2 and #11 in Test #1 and Test#8, respectively. The effect of changing effective stresses was examined for both the isotropic and anisotropic conditions. The tests were run at room temperature and at the in-situ reservoir temperature of 10 °C. The effective permeability of oil sands to brine was measured using specimen Core #7 in Test #2 and Test #3, and Core #8 in Test #9.

For isotropic initial stress states, the relationship between volumetric strain and effective stress was only modestly non-linear, as shown in Figure 4-2. The total volumetric strains are less than 2% before the effective stress dropped below 200 kPa both for brine saturated sands and oil sands specimens. There was no definitive inflection point to identify the transition from pre-failure to post-failure behaviour. Consequently, the initial isotropic stress states provided only a temporary improvement in permeability, returning to the original measured value once the injection was stopped.

Yale observed a similar relationship between the volumetric strains and the mean effective stress (Yale, Mayer and Wang, 2010). However, as a stress ratio of 1.1 was used in their testing, the relationship looks much closer to the isotropic stress state testing conducted in Test #1 and #2. The cumulative volumetric strains are less than 2% before the effective stress drops below 400 kPa (considering 200 psi of mean effective stress, and stress ratio 1.1). He also observed that the transition windows from pre-failure to post-failure were relatively wide. Since the bitumen is immobile, any increase in the effective permeability to water in Test #3 is attributed to the increase in the pore space available for water flow.

Under the anisotropic stress state with stress ratio 0.5 in Test #3, the volumetric strain increased closely linearly when the effective stress decreased at the beginning of the water injection. However, as a result of the pore pressure increase, the stress

ratio continuously changed, and thus resulted in sample shearing. When the effective stress dropped below 400 kPa, the volumetric strains had a dramatic increase and the effective stress remained at almost the same level. It showed the promising potential to permanently enhance the effective permeability and the porosity in the dilated zone under the deviatoric stress state.

The preliminary experimental results delivered some fundamental constitutive data linking the geomechanical behaviour of wet/oil sands to its hydraulic-mechanical behaviour under two stress states. This also provided verification data for the development of a numerical model, which can be used to help improve the industry's ability to understand the behaviour during fluid injection. Further work is still needed to confirm the observations above and determine the potential impact of stress ratio on geomechanical dilation of oil sands underwater injection scenarios.

4.5.Summary and Conclusions

High fluid injectivity between the injection well and the production well in oil sands formation is essential for quick communication and fast SAGD start-up. One potential benefit of high injectivity is the resulting high convective heat flux, which shortens the time for steam initialization in SAGD.

This chapter presents an improved technique and method to prepare a reliable representative water wet/oil sands specimen for laboratory analysis. A series of synthetic wet/oil sands core specimens were prepared with different fluid saturation using reclaimed/cleaned tailings sand from oil sands mining operations, which ensured they were representative of McMurray Formation oil sands. The updated approach of sand packing greatly enhances the capability to study fundamentals related to reservoir engineering and geomechanical engineering.

Promising experimental results from triaxial cell tests explored the potential for enhancing fluid injectivity by inducing geomechanical dilation via cold-water injection. Triaxial testing was conducted to evaluate the mechanisms and impacts of geomechanical dilation in a set of very dense, reconstituted brine-saturated or bitumen-saturated sand specimens during pore pressure injection.

Experimental data, presented and discussed in this chapter, demonstrate that McMurray Formation oil sands can yield large geomechanical dilation under an anisotropic stress state.

The experimental results deliver some fundamental constitutive data linking the geomechanical behaviour of wet/oil sands to its hydraulic-mechanical behaviour under two stress states. This provides verification data for the development of a numerical model and helps to improve the industry's ability to understand the behaviour during fluid injection. Further work is still needed to confirm observations above and determine the potential impact of stress ratio on geomechanical dilation of oil sands under the water injection scenarios.

Although only reconstituted sands cores were employed, the experimental set-up mimicked realistic in-situ reservoir conditions, in terms of temperature, pore pressure, and stress state. The grain size distribution of material tested is also representative of the McMurray oil sands.

Experimental results show a consistent relationship between volumetric strain and effective confining stress. Under an initial isotropic stress state, the relationships between porosity and absolute permeability with effective confining stress appear to be roughly reversible for a clean sand core. Similar conclusions can be attained regarding effective permeability to water for an oil sands core.

Next, the operating conditions favouring dilation are explored. The experimental results identified the presence of a critical injection pressure that yields plastic volumetric change, as evidenced by the analysis of variations in porosity and permeability along various stress paths within an oil sands core specimen. The experimental data presented in this chapter has been analyzed for identifying the critical injection pressure required to trigger the dramatic volumetric strain as a result of dilation. The results demonstrated that water injectivity on a synthetic core specimen can be enhanced under certain favourable conditions, which include a modest level of stress anisotropy.

Given parameters such as the initial stress state, initial pore pressure, and peak strengths of materials, the critical operating pressure was estimated, which enabled the generation of a positive geomechanical response and enhanced water injectivity. The critical injection pressure, based on the analysis of the critical injection pressure, matched reasonably with the observed lab-scale tests. The expression of failure envelopes, however, needs further calibration. Further work is also still required to confirm the observations above and determine the potential impact of the stress ratio on geomechanical dilation of oil sands underwater injection scenarios.

Based on laboratory observations, geomechanical dilation could greatly increase porosity and enhance fluid injectivity in the dilated zone, while the operating pressure is kept below the maximum principal stress. This is achievable through cold-water injection, where the operating pressure rises with increases in flow resistance in the formation. The local effective stress on the formation will decrease accordingly. Once it approaches the strength of the formation, shearing failure occurs. Based on the strength theories of geomaterials, it is not necessary to operate at a high injection pressure exceeding the maximum principal stress to achieve geomechanical dilation, provided that the deviatoric stresses reach the yielding strength.

Study results showed that it is not necessary to operate at a high injection pressure exceeding the maximum principal stress to create geomechanical dilation and consequently enhance the effective permeability to water. The study will help industry actors to further understand the behaviour of oil sands and to explore potential fluid injectivity enhancement in oil sands formations through cold-water injection.

CHAPTER 5. NUMERICAL MODELLING ON ASSESSING SAGD PERFORMANCE DUE TO GEOMECHANICAL DILATION START-UP

5.1. Introduction

One of the main objectives of this study is to evaluate the SAGD performance due to the enhanced start-up operation. A lab-scale test has its limitations and has high costs for one single setup and test. Specifically, a lab-scale test related to the thermal recovery process involves high temperature and high pressure. This is challenging as it requires. This study is not intended to assess the impacts on SAGD performance directly through a lab-scale test; that is beyond the scope of this study. Numerical simulations are to be carried out to study the behaviour of oil sands and evaluate SAGD performance, in terms of steam chamber development, water and oil production, and steam oil ratio (SOR).

The chapter established and verified a geomechanical model based on experimental results from a set of the lab-scale test. The model was then adopted as a field-size simulation to mimic the SAGD process, which combined fluid flow, heat transfer, and geomechanics under reservoir conditions. The numerical model used the results from laboratory testing and incorporated accurate physics and constitutive equations.

A geomechanical constitutive model and a single-phase-flow model were established respectively using Itasca's FLAC3D software, in which the solutions to the flow and stress equations were coupled sequentially. Pore- pressure-increase-injection was modelled to simulate the dilation start-up process and the enhancement in porosity and permeability using a Cartesian mesh. The triaxial compression tests (Chapter 4) under three different effective stresses were used to tune the geomechanical properties of oil sands (i.e., Young's Modulus, frictional angles, dilation angles) in the geomechanical models. The relationship between

permeability enhancement and effective confinement stress was calibrated based on the results of the dilation experiments. The calibrated model was then used to simulate a field-scale dilation start-up process using FLAC3D, via cold-water injection for a SAGD well pair at reservoir conditions. Results from this field-scale FLAC3D model are representative of the end state of the start-up process. These results were then used to initialize a flow model for simulating the full phase of SAGD performance. Available geological and petrophysical data were also incorporated in the model. The flow simulation results were analyzed to assess the impacts on SAGD recovery due to the dilation enhanced start-up operation, made possible by applying proper injection pressures in specific formations.

Oil sands dilation behaviour and post-peak material softening/hardening behaviour were reasonably represented in the coupled simulation. A computational model of a 330-meter-deep synthetic Athabasca oil sands reservoir was set up. Some of the flow and geomechanical material properties were populated based on the latest public information and field data available.

5.2. Coupled Hydrodynamic-Geomechanical Simulations of Lab-Scale Experiments

The conservation of mass and linear momentum, and the effective stress law formed the governing equations of the model. These equations led to partially differential relationships that are solved for displacements and fluid pressure by FLAC3D.

The following assumptions were made to develop a numerical model

1) Due to the extremely high viscosity of bitumen, the low in-situ temperature (10 °C) allows quite low bitumen mobility. Therefore, bitumen can be assumed to be immobile, such that water is the only flow phase in the porous media. The problem was simplified to a single-phase Darcy model.

2) Therefore, bitumen in the porous media is considered part of solids for the flow model during cold-water injection as a start-up operation.

3) The temperature is constant throughout the water injection, which was reasonable.

4) The materials (sands, bitumen, brine) tested in the lab are elements and can represent for oil sands well in the reservoir formation.

5) The geo-materials (sands, bitumen, brine) were well distributed homogeneously and isotopically within the reservoir formation prior to cold-water injection.

5.2.1. Overall Modelling Approach

First, a constitutive model was established for the oil sands. Experimental measurements, in terms of deviatoric stress and volumetric strain against the axial strain, obtained experimentally in Chapter 4 were used to tune the unknown geomechanical parameters (E, ν, c, ϕ, ψ).

Next, the permeability and porosity update models were calibrated according to the geomechanical dilation results (i.e., the correlation of Eqs. 5-17 and 5-18 between the effective permeability to water and volumetric strain/dilation). The permeability enhancement is attributed to both elastic and plastic dilation: increases in pore pressure (reduction in effective stress) result in a change in volumetric strain; part of the strain was elastic and reversible, while the remaining is plastic and irreversible (permanent after the failure of oil sands).

Several lab-scale coupled models were developed in FLAC3D to simulate the dilation start-up injection process and to capture the following key physical phenomena:

- Effective permeability enhancements;
- Porosity enhancements;

- Strain softening/hardening constitutive model for oil sands;
- Stress-dependent modulus for oil sands;
- Volumetric-strain-dependent modulus for frictional and dilation angles of oil sands;
- Flow mechanics related to the pore-pressure-increase model.

The unknown model parameters were tuned against the aforementioned experimental data. The final calibrated model parameters were then used to construct a field-size model. The porosity, fluid saturations, and other petrophysical parameters were calculated and updated in the geomechanical simulator FLAC3D. All these properties were assigned to the grids in the reservoir model with a field SAGD size through SKUA-GOCAD. A data file was exported in a CMG format, which contained basic and initial petrophysical parameters of the interested reservoir.

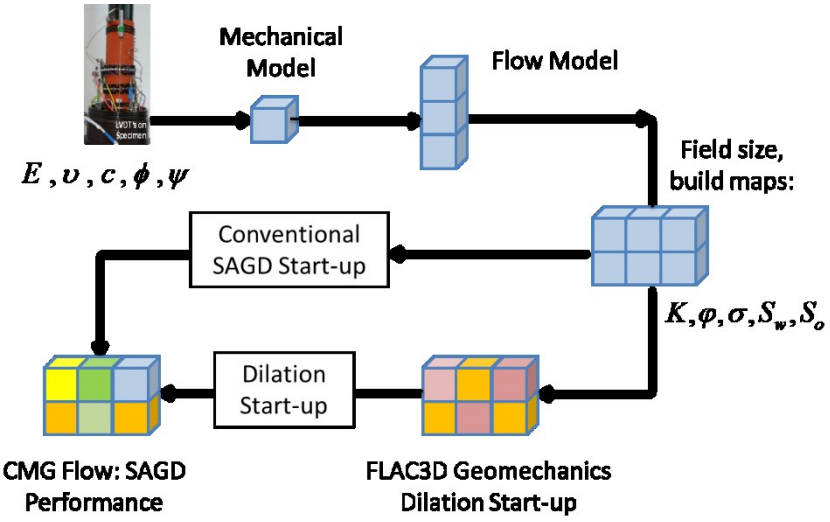

Figure 5-1. Workflow of the numerical simulation with geomechanical simulator FLAC3D and reservoir simulator CMG STARS

Finally, the full SAGD phase was simulated using the reservoir simulator CMG STARS. The entire workflow was depicted in CMG STARS. The workflow was depicted in the chart as shown in Figure 5-1. To ensure compatibility between the

two modelling steps, the same discretization mesh in FLAC3D is also employed in CMG STARS.

Three specific aspects of the constitutive models of the oil sands were modelled in this thesis, which is detailed in the next section.

5.2.2. Stress-Dependent Volumetric Strain of Oil Sands Due to Injection

Bulk volume and pore volume compressibility of Athabasca oil sands have been studied and measured either by confined compression in an oedometer or by isotropic compression in a triaxial cell. The important finding is that, under an isotropic cyclic stress condition, the oil sands behave elastically. Agar found that the relationship between effective confining stress and volumetric strain upon unloading and reloading in isotropic cyclic consolidation is repeatable (Agar, 1984). Kosar carried out a series of constrained compression tests and isotropic compression tests with Athabasca McMurray Formation oil sands and Athabasca Clearwater Formation oil sands (Kosar, 1989). The repeatability of the results indicated the elastic behaviour of the oil sand in stress cycling.

The bulk compressibility of the oil sands core ($\boldsymbol{C_{bp}}$), representing the effect of effective-stress variations on the total bulk volume of the oil sands specimen under constant confining pressure (Zimmerman, Somerton and King, 1986), can be expressed as follows.

$$C_{bp} = \frac{1}{V_b}\left(\frac{\partial V_b}{\partial P_p}\right)_{P_c} \qquad \text{Eq. 5-1}$$

Similarly, the pore compressibility ($\boldsymbol{C_{pp}}$), representing the effect of pore pressure variations on the total pore volume in the oil sands specimen under constant confining pressure, can be expressed by Eq. 5-2.

$$C_{pp} = \frac{1}{\emptyset V_b}\left(\frac{\partial V_p}{\partial P_p}\right)_{P_c} \qquad \text{Eq. 5-2}$$

The pore volume is filled with water, oil, and gas for an oil sands core. The compressibility of water ($\boldsymbol{C_{wp}}$), oil ($\boldsymbol{C_{op}}$), and gas ($\boldsymbol{C_{gp}}$) with varying pore pressure (P_p) and constant confining pressure can be defined in the same manner.

For water,

$$C_{wp} = \frac{1}{\emptyset V_b S_w}\left(\frac{\partial V_w}{\partial P_p}\right)_{P_c} \quad \text{Eq. 5-3}$$

For oil,

$$C_{op} = \frac{1}{\emptyset V_b S_W}\left(\frac{\partial V_o)}{\partial P_p}\right)_{P_c} \quad \text{Eq. 5-4}$$

For gas,

$$C_{gp} = \frac{1}{\emptyset V_b S_g}\left(\frac{\partial V_g)}{\partial P_p}\right)_{P_c} \quad \text{Eq. 5-5}$$

For solid grains ($\boldsymbol{C_{sp}}$), its compressibility with varying pore pressure can also similarly expressed the following.

$$C_{sp} = \frac{1}{(1-\emptyset)V_b}\left(\frac{\partial V_s)}{\partial P_p}\right)_{P_c} \quad \text{Eq. 5-6}$$

Considering that the volumetric strain of the sand skeleton is the total sum of the solid grains and the liquid water and oil, it can be written as follows:

$$\partial V_b = \partial V_p + \partial V_s = (\partial V_w + \partial V_o + \partial V_g) + \partial V_s \quad \text{Eq. 5-7}$$

Then, substituting the expressions Eq. 5-1 through **Error! Reference source not found.** into Eq. 5-7 to yield Eq. 5-8.

$$-C_{bp}\partial\sigma' = (C_{wp}S_w + C_{op}S_o + C_{gp}S_g)\varphi\partial u + C_{sp}(1-\emptyset)\partial u \quad \text{Eq. 5-8}$$

When the confining pressure is maintained as constant, effective stress becomes as follows.

$$\partial\sigma' = \partial\sigma - \partial P_p = -\partial P_p \qquad \text{Eq. 5-9}$$

Then Eq. 5-8 can be rewritten as the following.

$$C_{bp} = (C_{wp}S_w + C_{op}S_o + C_{gp}S_g)\emptyset + C_{sp}(1-\emptyset) \qquad \text{Eq. 5-10}$$

Therefore, the volumetric strain prior to failure under the constant confining pressure can be expressed by the following.

$$\varepsilon_v = \frac{\Delta V_b}{V_b} = \Delta\sigma'\left[(C_{wp}S_w + C_{op}S_o + C_{gp}S_g)\emptyset + C_{sp}(1-\emptyset)\right] \qquad \text{Eq. 5-11}$$

where, $$S_w + S_o + S_g = 1 \qquad \text{Eq. 5-12}$$

It can be noted that the bulk volume change under the constant confining pressure is related to the petrophysical properties in terms of porosity and volume of the core, pore compressibility of each phase in the core, and effective stress variation. To determine the bulk volume change during pore pressure injection, it is critical to have good control of the porosity and the saturation of each phase in the core.

In this study, gas saturation (S_g) is zero.

5.2.3. Stress-Dependent Young's Modulus

Three geomechanical compression tests were conducted on the sands specimen under there different effective stresses. All three synthetic sands specimens were prepared with the same packing methods as those tested on geomechanical dilation. As discussed above, all these sands specimens possessed almost identical geomechanical properties in terms of porosity, void ratio, fluid saturation, and dry

density. Thus, the mechanical properties generated from the compression tests could be compared across the sands specimens reasonably. The geomechanical properties measured through the compression tests were well represented by the properties in the geomechanical dilation testing. As a part of the compression test results, Young's modulus of the oil sands is shown to be dependent on the minimum effective stress as Figure 5-2.

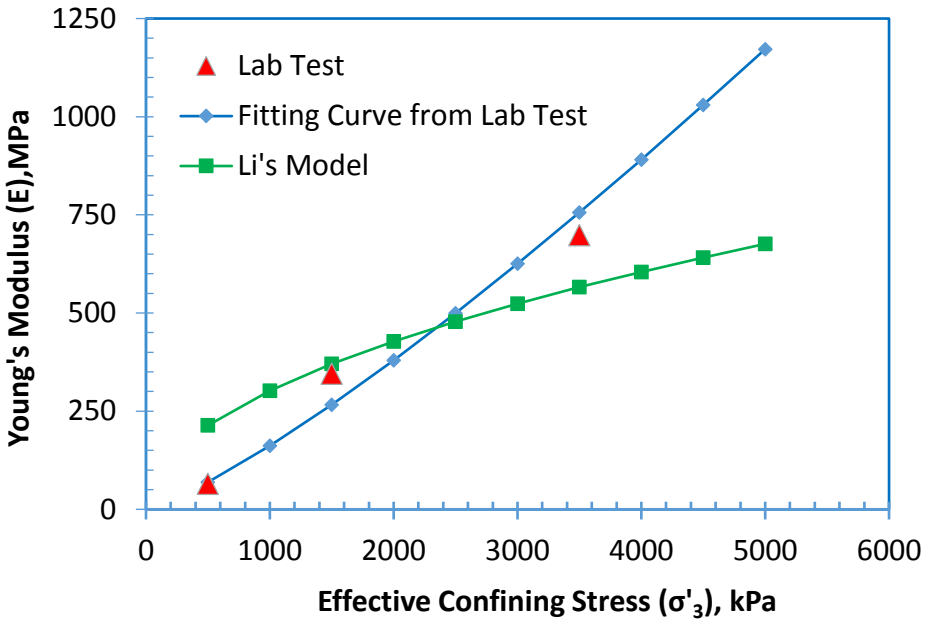

Figure 5-2. Young's modulus versus effective stress

Young's modulus (E) of oil sands could be reasonably assumed to have a non-linear elastic behaviour with minimum effective confining stress. The trend line could be regressed to an exponential function as the following equation.

$$E = 95.6 \times P_{atm} \times \left(\frac{\sigma_3'}{P_{atm}}\right)^{1.23} \qquad \text{Eq. 5-13}$$

The unit of Young's modulus and minimum effective stress kPa. P_{atm} , the atmospheric pressure, was set to 101.325 kPa and was used only for normalizing purposes in this equation.

Similarly, this non-linear elastic behaviour of the constitutive model was first developed and expressed in the exponential function by Li and Chalaturnyk (Li and Chalaturnyk, 2009).

$$E = 950 \times P_{atm} \times (\frac{\sigma_3'}{P_{atm}})^{0.5} \quad \text{Eq. 5-14}$$

It can be noted that Young's Modulus increased in the magnitude of exponent with the increasing of minimum effective stress. In this numerical simulation, a linear function was used as the following.

$$E = 206 \times \sigma_3' \quad \text{Eq. 5-15}$$

5.2.4. Strain-Dependent Frictional Angles

The pre-failure cohesion and tension were set to 100 kPa and the pre-failure friction and dilation were 36 and 16 degrees, respectively. The pre-failure cohesion and tension values were usually measured as zero for clean, bitumen free oil sands. In this case, the oil sands were modelled with a low cohesion and tension value to represent the slight effects of immobile bitumen. Once a failure occurred, the cohesion and tension were reduced to zero. The equations used for frictional angle (ψ) modelling shown in Figure 5-3 was expressed by the following function:

$$\psi = 23.3 + 13 \times (1 - e^{-132\epsilon_{vol}}) \quad \text{Eq. 5-16}$$

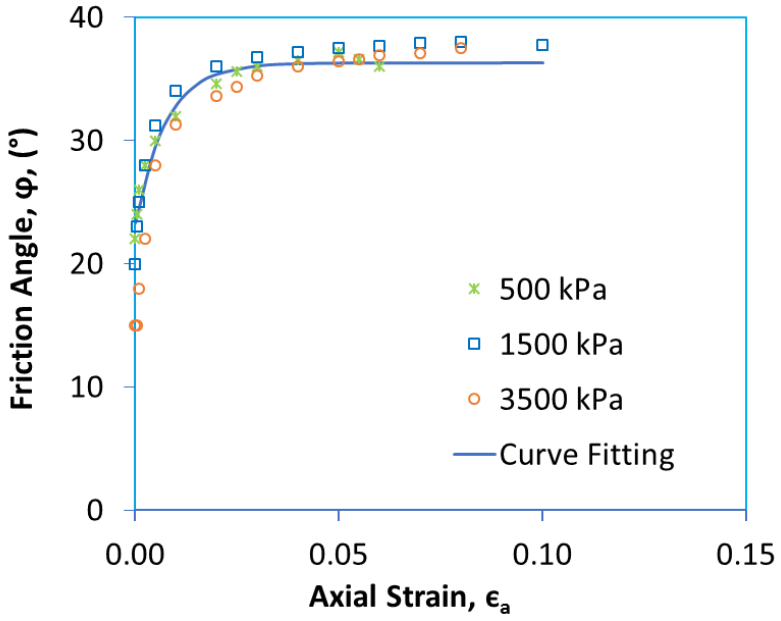

Figure 5-3. Frictional angles obtained from the lab data matching

It can be noted that the friction angles remained unchanged after reaching 36.6 degrees in three different compression tests. In the oil sands strain softening/hardening models, the friction angles were set to 36.6 degrees for the post-failure stages. The dilation angles were set constant 16.0 degrees for the numerical simulation.

5.2.5. Geomechanical Model

Three types of cell models were used to verify the proposed geomechanical, fluid flow, and permeability update models inside of FLAC3D, shown in Figure 5-4.

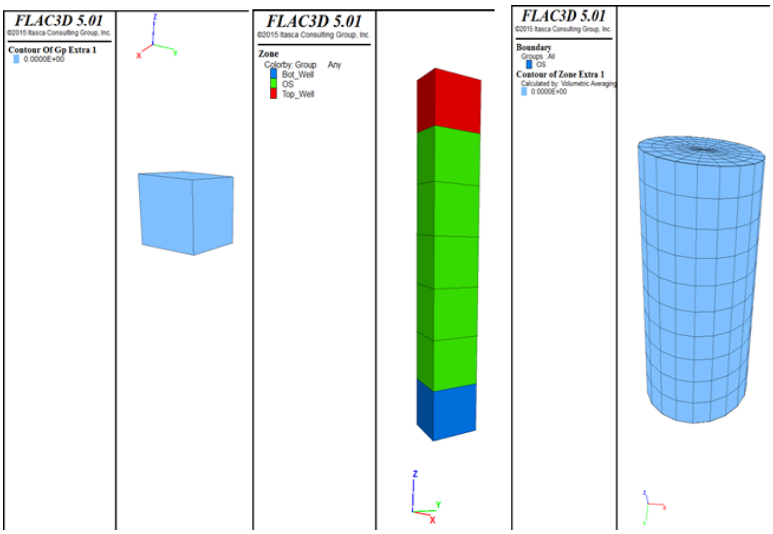

Figure 5-4. Three types of cell model: one-cell model, seven-cell model, and cylinder model used in the FLAC3D simulation

A simple single-cell model was used to test the mechanical model, the permeability update model, and the pore pressure injection model. This simple type of model could save the computing time needed to reach equilibrium. A seven-block stacked model was used to simulate fluid flow across several zones. A cylinder model was used as a comparison for the results in the simple single cell.

In each model, the bottom was fixed. Stress and boundary conditions were applied where required, shown in Figure 5-5.

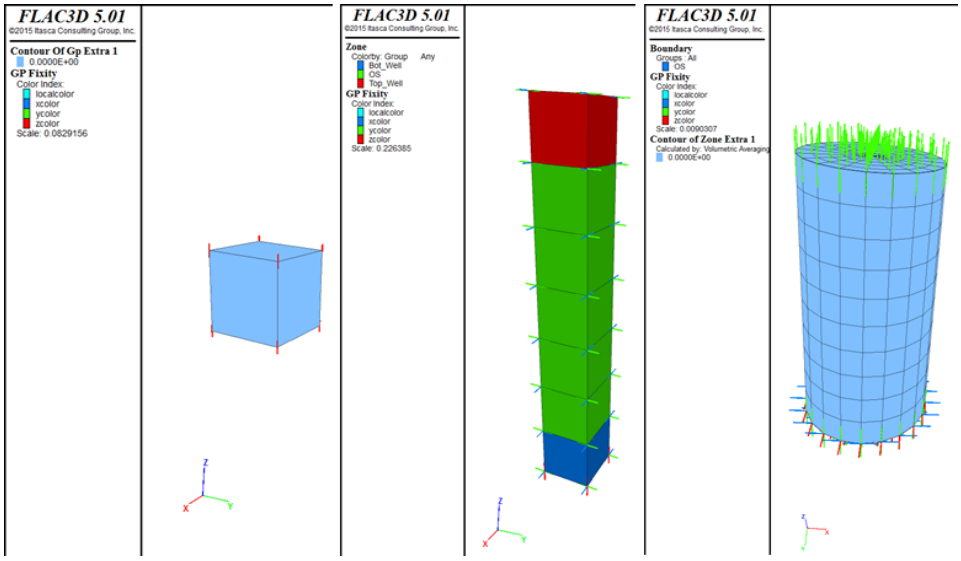

Figure 5-5. The displacement boundary condition in three types of model: the fixed bottom of the model

Oil-sands strength increases after failure and after a plastic strain is developed, they slightly decrease after reaching their peak values. The properties of oil sands used in the FLAC3D simulation are summarized in the following table (**Table 5-1**).

Table 5-1. Properties of oil sands used in the FLAC3D simulation

Material	Model	Property	Units	Value
Oil Sands	Strain Softening	Bulk Modulus	kPa	Eq. 5-15
		Shear	MPa	113
		Tension	kPa	100
		Cohesion	kPa	100
		Density	kg/m3	2250
		Friction	Degree	36°
		Dilation	Degrees	16°

5.2.6. Flow Model

The water injection rate during geomechanical dilation tests induced by cold-water injection was maintained at a very low level so the differential pore pressure along the length of the specimen also remained low. These values ranged between 5 kPa, for an oil-free sand specimen, and 100 kPa for an oil sands specimen.

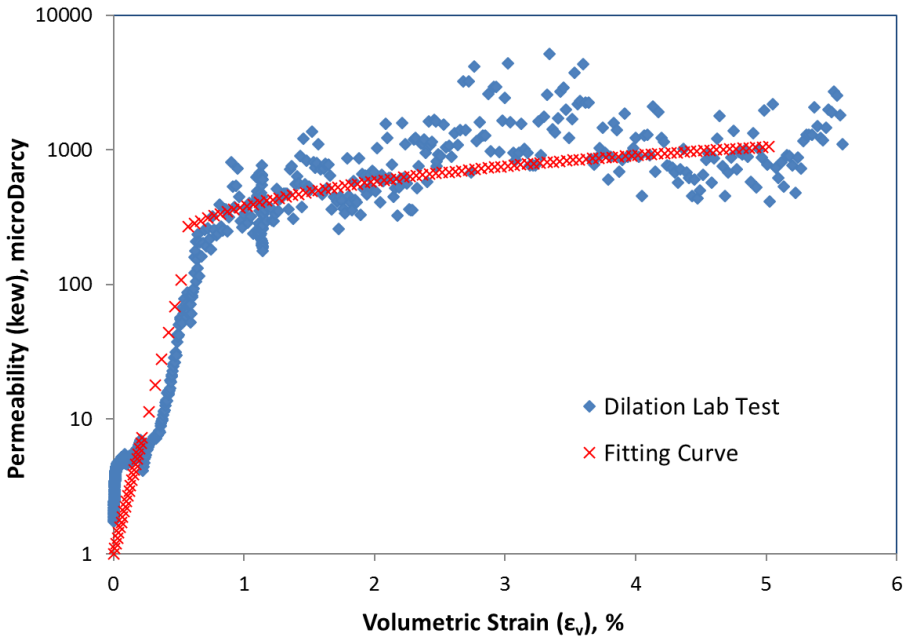

Figure 5-6. Regression curves for the effective permeability to water versus volumetric strain during geomechanical dilation test

The model for single-phase Darcy's law was used to compute the effective permeability to water, as shown in Figure 5-6. Measurements of the effective permeability, as a function of volumetric strain from Chapter 4, were also compared. As mentioned in the previous section, the total volumetric volume (ϵ_v) can be represented as the sum of two components: elastic (ε_v^e) and plastic (ε_v^p) responses.

$$\varepsilon_v = \varepsilon_v{}^e + \varepsilon_v{}^p \qquad \text{Eq. 5-17}$$

Therefore, the experimental data is fitted with two distinct regression functions, as shown in Figure 5-6. The fitting curves are regressed as two sections and can be simply expressed by two functions. The first function is the following.

$$k_{ew} = k_{ewi} \times Exp(900\varepsilon_v) \qquad \text{Eq. 5-18}$$

In which, $(k_{ew})\ and\ (k_{ewi})$ are the transient and the initial effective permeability to water, respectively, with a unit of millidarcy, and (ε_v) is the volumetric strain. An empirical constant of 900 is used for normalizing purposes. The second segment is expressed as a power function:

$$k_{ew} = 360 \times (100\varepsilon_v)^{0.66} \times k_{ewi} \qquad \text{Eq. 5-19}$$

The expressions of Eqs. 5-18 and 5-19 capture the dilation experienced by the core sample during cold-water injection under anisotropic stress states, as well as the effective permeability increase due to an increase in porosity. They capture both the reversible and irreversible behaviours associated with elastic and plastic deformation described in Chapter 4.

It should be noted that a positive sign represents an increasing volumetric strain and a negative sign denotes compaction in volumetric strain. The elastic response reflects reversible compaction or expansion of the material. In contrast, the plastic geomechanical response occurs due to the failure and plastic behaviour of the

material. It can be shown that porosity changes ($\emptyset_w^{new}$) with the volumetric strain (ε_v) according to the following equation.

$$\emptyset_w^{new} = \frac{\emptyset_{wi} + \epsilon_v}{1 + \epsilon_v} \qquad \text{Eq. 5-20}$$

Eq. 5-20 can be used to update the porosity values due to volumetric strain in the numerical simulation. Both elastic and plastic volumetric strain changes the effective water porosity ($\emptyset_w = \emptyset_{wi} * S_w$), which is the product of local average porosity ($\emptyset_{wi}$) and water saturation (S_w) in the porous media. The experimental results demonstrate that the impacts of elastic and plastic volumetric strains on the effective permeability to water are different. It is expected that a permanent permeability enhancement occurred due to shearing dilation while the reversible permeability and volume change occurred due to elastic compression/expansion. The elastic response is deemed as only a change in pore volume without grain rearrangement.

5.2.7. Pressure Injection for Failure

The oil sands in the dilation start-up simulations were represented with a strain-softening model. Prior to failure, the sands follow a simple Mohr-Coulomb strength envelope represented by Eq. 5-21 which requires: initial reservoir pressure (P_{ini}), maximum (σ_1) and minimum (σ_3) total stress, friction (ϕ), and cohesion (c) of the sand.

$$(\sigma_1 - P_{ini}) = (\sigma_3 - P_{ini}) \times t^2 + 2c \times t \qquad \text{Eq. 5-21}$$

where $t = tan(45 + \frac{\varphi}{2})$ Eq. 5-22

Therefore, the reservoir pressure required for failure (P_f) can be determined by solving Eq. 5-21 for pressure, resulting in Eq. 5-23:

$$P_f = \frac{1}{t^2 - 1}(2c \times t + \sigma_3 \times t^2 - \sigma_1) \quad \text{Eq. 5-23}$$

From the Mohr-Coulomb failure criterion and the stress field at both wells, the increase in pressure required to create failure was determined. Based on each of these values, the injection pressure for each stress field case was set to 50%, 100%, and 150% of the pressure required for failure, respectively.

For each model, the wellbore pressure was initialized at the reservoir pressure and then increased linearly to the maximum wellbore injection pressure over a five-minute period.

The equation represents the pressure required to initiate failure in the oil sands. However, the pressure needed to be propagated at a reasonable rate and therefore, a pressure injection factor (f) is added to determine the injection pressure for each simulation (Eq. 5-24).

$$P_{inj} = f \times P_f \quad \text{Eq. 5-24}$$

5.2.8. FLAC3D Verification Results

After the constitutive model was established and tested for oil sands using a simple one cell model in FLAC3D, this model was validated by comparison with the laboratory testing data in terms of deviatoric stress and volumetric strain. All these triaxial compression results were obtained from the geomechanical compression test on cylinder cores.

The relationships of deviatoric stress with the effective confining stress of 500, 1500, and 3500 kPa, respectively, are shown in Figure 5-7.

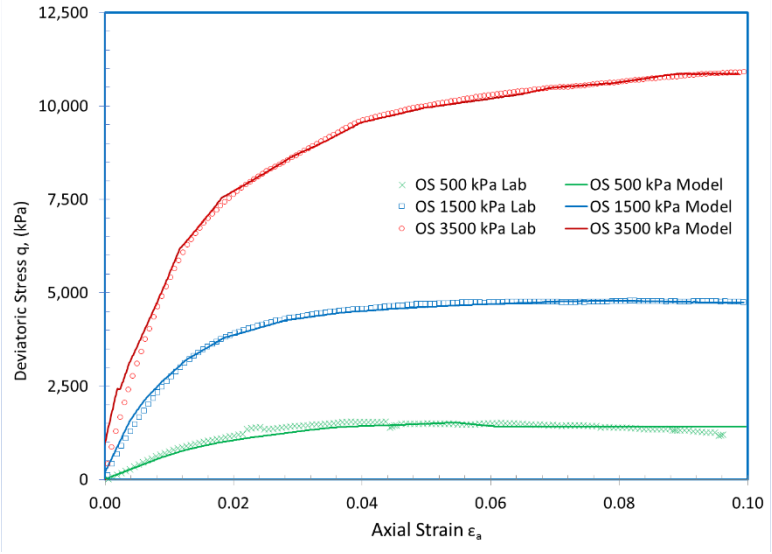

Figure 5-7. Oil sands constitutive model axial strain versus deviatoric stress for effective confining stresses of 500, 1500, and 3500 kPa

The strain softening/hardening model parameters and Young's modulus function described in Table 5-1 were tested in the simple one cell model to ensure that correct strain-softening behaviour was captured by FLAC3D. The Young's modulus function was applied at every equilibrium step of FLAC3D. The bottom of the single cell was fixed. Stress boundary conditions were applied and allowed to reach equilibrium, which is shown in Figure 5-5. Once the model was at equilibrium, a velocity boundary condition was applied to the top of the specimen to simulate an axial loading test. The specimen was tested at 500, 1500, and 3500 kPa of effective confining stress in terms of deviatoric stress and volumetric strain, shown in Figure 5-7 and Figure 5-8.

The solid continuous curves were generated from the FLAC3D while the dotted curves reflected the experimental triaxial tests. It can be noted that the deviatoric stress curves from the simulation results (the constitutive model) almost perfectly lie above those obtained from the lab-scale tests.

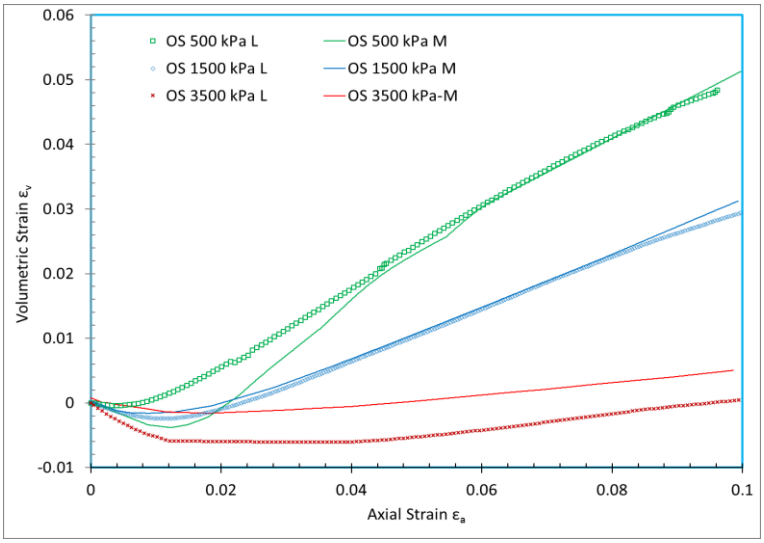

Figure 5-8. Oil sands constitutive model axial strain versus volumetric strain for effective confining stresses of 500, 1500, and 3500 kPa

Therefore, the constitutive model reasonably matched the main mechanisms during the geomechanical compression test.

The constitutive model was executed in three different cell models: one-cell, seven-cell, and cylinder-cell models. No different volumetric strain and deviatoric stress curves were obtained from these three different cell models. It indicated that the constitutive model could be run on any of these cell models; the same simulation could be obtained no matter the amount and the shape of the cell. One of the main reasons is there were no boundary effects in this numerical simulation, unlike in lab-scale compression tests. Also, the properties of the materials were perfectly identical, isotropic, and uniform across the cell in the numerical simulation.

The minimum effective stress-dependent Young's modulus function was also tested and is shown in Figure 5-9.

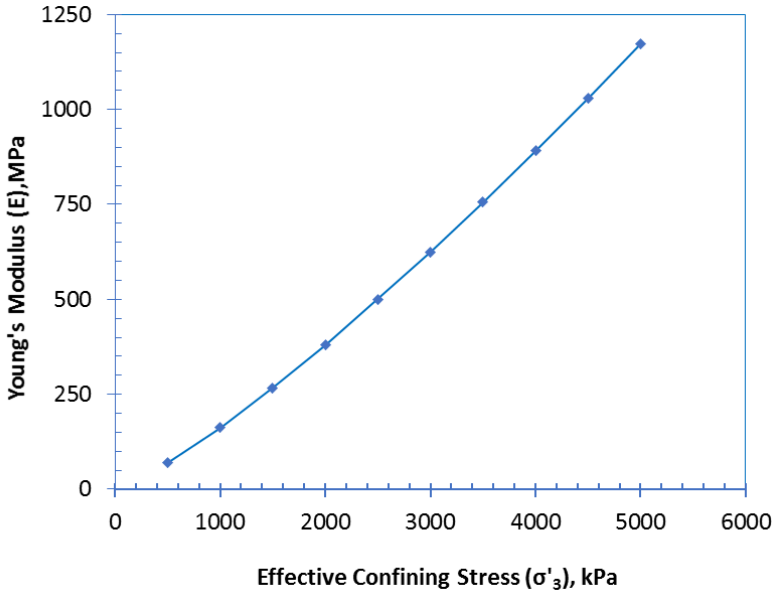

Figure 5-9. Minimum effective stress-dependent Young's modulus model results from FLAC3D testing.

5.3. Numerical Simulation of Field-Scale Dilation Process

A field-size model was constructed to examine the geomechanical response due to an enhanced SAGD start-up operation. Model parameters calibrated from the lab-scale set-up in Section 5.2 were used here.

5.3.1. Geological Model

A synthetic model of a medium-to-deep oil sands reservoir was employed in this study. Reservoir and fluid properties representative of a typical Athabasca deposit is assigned. In the simulation, the reservoir was located 330 meters under the surface ground (Cenovus, 2014), which is elevated at a sea level of 600 meters (see Figure 5-10). The oil sands reservoir was 25 meters in height and 100 meters in width. In addition, 20 meters of overburden and 55 meters of under-burden were included in the grid. The well spacing was designed to be 100 m and the wells were placed in the middle of the model. Both the horizontal injection and production wells used for SAGD operations had lengths of 800 m.

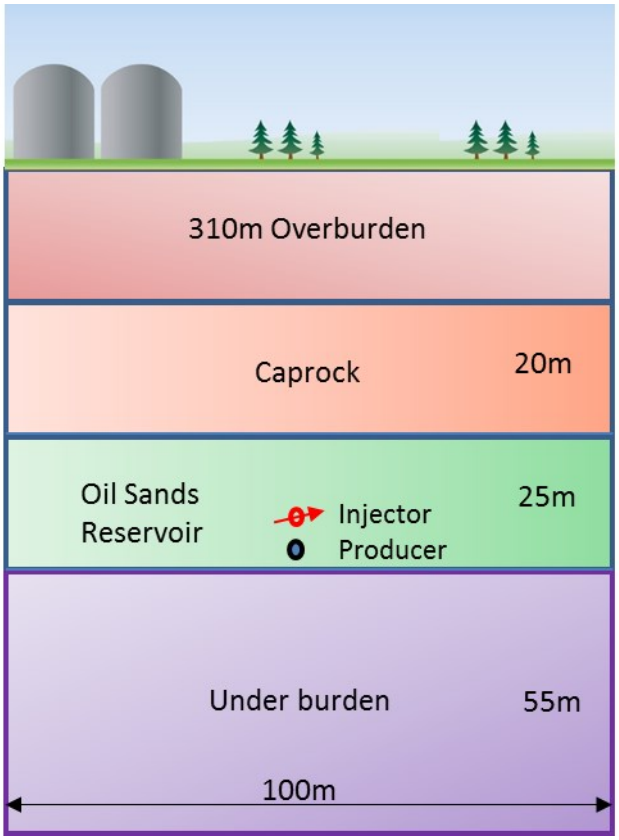

Figure 5-10. Model geometry

The grid size of the dilation start-up model in FLAC3D was 100 meters by100 meters in x and z directions, and 0.2 meters in the y-direction. Therefore, a two-dimensional geometry was considered for modelling the problem. A plane strain solution was used for geomechanical modelling and no strain was allowed in the direction normal to the two-dimensional cross-section. Similarly, no fluid flow and heat transfer were allowed in this direction.

The reservoir zone was 25 meters thick and was placed between the overburden and under-burden shale formations. The depth of the formations and well locations were taken from data listed in Table 5-2, which provides the initial model geometry and the geometrical parameters of the dilation start-up model.

Table 5-2. Dilation Start-up model geometrical parameters

Parameter	Elevation (m)	Depth (m)
Ground Surface	600	0
Water Table	570	30
Oil Sands	270	330
Top Well	252	348
Bottom Well	247	353
Bottom Shale	245	355
Total Model Height (m)	100	
Total Model Width (m)	100	
Well Spacing (m)	5	
Well Radius (m)	0.075	

In total, 90 horizontal layers of grid blocks with variable vertical sizes were considered in the model and the entire width was divided into 100 grid blocks with equal horizontal widths. To capture the failure and post-failure states of the oil sands around the well pair during water injection, a finer mesh was used to discretize the inter-well region. Figure 5-11 illustrates a part of the mesh used in this model. The grid sizes are smallest near the wellbores and gradually increase further away. The grid sizes between the well pair varied between 2 and 13 centimetres.

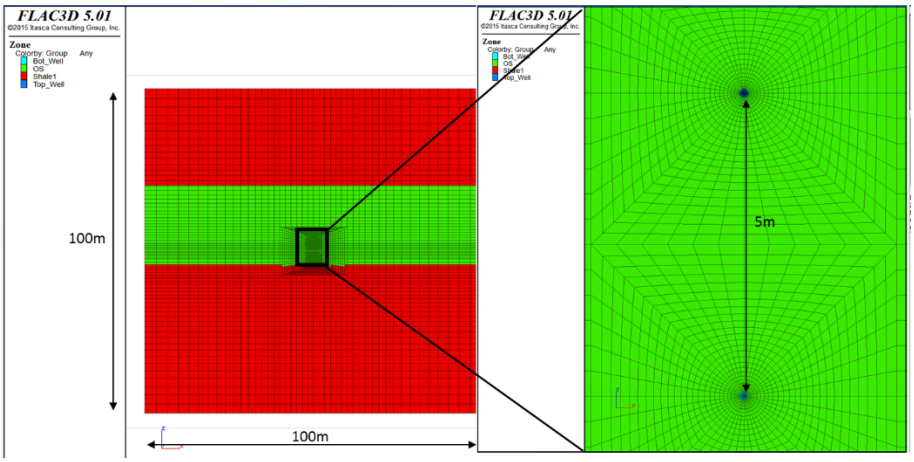

Figure 5-11. FLAC3D geometry for dilation start-up modelling: Red is Shale, Green is Reservoir

Figure 5-11 illustrates the geometry of the model along with the locations of the reservoir, the regions of under/overburdens and the well pair region. The details of the grid shape and sizes are indicated around the well pair region.

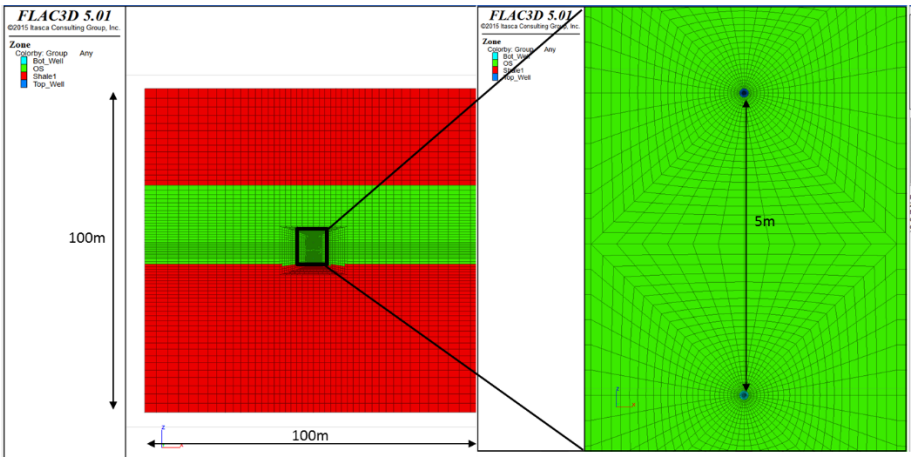

Figure 5-11. FLAC3D geometry for dilation start-up modelling: Red is Shale, Green is Reservoir

5.3.2. Petrophysical, Fluid, and Thermal Properties

The flow properties used for the simulation were averaged and converted to single-phase water permeability values using the process described above. The properties are listed in Table 5-3. The resulting effective horizontal water permeability was equal to 60 mD, similar in the x and y-direction. The resulting effective vertical water permeability was 60 mD. The petrophysical, fluid, thermal, and geomechanical properties for overburden, Caprock, reservoir, and under-burden were obtained from public domain information and field SAGD projects (e.g., AER reports). The detailed petrophysical, fluid and thermal properties are listed in Table 5-3.

Effective water porosity is used to model flow and calibrated using fluid saturations. It can be defined as the product of the local porosity ($\emptyset_{wi}$) and its relevant water saturation (S_w) in the reservoir, which can be expressed as the following.

$$\emptyset_w = S_w \cdot \emptyset_{wi} \qquad \text{Eq. 5-25}$$

When cold-water is injected into the formation, the geomechanical response reflects in terms of the porosity change. Thus, the effective water porosity is 0.07 for oil sands. The effective permeability to water for the shale in both over-burden and under-burden was 0.001 mD in both horizontal and vertical directions. The effective water porosity of the shales was 0.01 as water saturation is 100% inside of the shale.

Table 5-3. Flow properties used in field-size FLAC3D Models

Formation	Property	Units	Original Value	Effective to Water
	Porosity	(Dimensionless)	0.07	0.07
	Saturation	(Dimensionless)	1.0	
Wellbores	kx	mD	1000	1000
	ky	mD	1000	1000
	kz	mD	1000	1000

Overburden and Underburden	Porosity	(Dimensionless)	0.01	0.01
	Saturation	(Dimensionless)	1.0	
	kx	mD	1	1
	ky	mD	1	1
	kz	mD	1	1
Oil Sands	Porosity	(Dimensionless)	0.3	0.07
	Saturation	(Dimensionless)	1.0	
	kx	mD	3000	60
	ky	mD	3000	60
	kz	mD	1500	30

Heterogeneity and isotropy were assumed across the net pay zone in the reservoir. The horizontal permeabilities k_x and k_y were set to 3000 mD and the vertical permeability, k_z, was set to 1500 mD.

The temperature of the injected water was set 10°C, giving a fluid viscosity of 1 cp and a density of 993 kg/m^3. It was assumed that the reservoir water is at the same temperature of the injected water neglecting any effects of 20 °C water from the surface being injected into a warmer/cooler reservoir fluid.

The petrophysical, fluid, thermal, and geomechanical properties for overburden, Caprock, reservoir, and under-burden are obtained from public domain information and from some field SAGD projects (e.g., AER reports).

The reservoir is considered typical Athabasca oil sands with a porosity of 30% and an initial permeability of 3000 mD horizontally and 1500 mD vertically. The detailed petrophysical, fluid and thermal properties are listed in Table 5-3.

To enhance the accuracy of the predictions, the grid sizes in the model were chosen to be small. Due to the high refinement of the grids, the model was run in quasi 2D, with the y-direction being fixed and the model allowed to translate in the x and z-direction.

5.3.3. Geomechanical Properties and In-situ Stresses

The modelling of the dilation start-up requires three types of material constitutive models, each for wellbores, shale, and oil sands. The wellbores mechanical model is elastic, and the flow is isotropic. The shale and oil sands were both mechanically modelled using a Strain Softening model, however, the shale was set to behave like a perfectly plastic material. Additionally, the oil sands use a stress-dependent Young's modulus model. An anisotropic flow model was used for both the shales and the oil sands. The properties used are shown in Table 5-4.

The caprock was assumed to behave according to a strain-softening plasticity-constitutive model. Partial parameters for this model were obtained from Cenovus's Christina Lake SAGD project (Yuan, Xu and Palmgren, 2013) and the UTF project (Li and Chalaturnyk, 2006). Linear elastic behaviour was assumed for overburden and under-burden. The constitutive models and corresponding parameters for each stratum are listed in Table 5-4.

Table 5-4. Summary of geomechanical properties for the model used in FLAC3D

Formation	Model	Property	Units	Value
Wellbore	Elastic	Density	kg/m3	2300
		Bulk	MPa	1000
		Shear	MPa	500
Shale (Over-burden and Under-burden)	Strain Softening – Perfectly Plastic	Density	kg/m3	2300
		Bulk	MPa	98e6
		Shear	MPa	37e6
		Tension	MPa	200e3
		Cohesion	MPa	300e3
		Friction	Degrees	35
		Dilation	Degrees	10
Oil Sands	Strain Softening	Density	kg/m3	2250
		Bulk	MPa	Eq.5-14
		Shear	MPa	113
		Cohesion	kPa	100
		Tension	kPa	100
		Dilation	Degrees	36.6
		Friction	Degrees	16

5.3.4. Stress and Pore Pressure Field

There are three components of in-situ stress: vertical stress (σ_v), minimum horizontal stress (σ_h) and maximum horizontal stress (σ_H). The information for in-situ stress used in the simulation was referenced from Christina Lake (Cenovus, 2014).

Three separate, but related stress fields were selected for dilation start-up analysis. The vertical and maximum total stress gradients were set to 22 kPa/m and 24 kPa/m, respectively. Three minimum horizontal stresses were selected: 15 kPa/m (Figure 5-12), 18 kPa/m (Figure 5-13) and 21 kPa/m (Figure 5-14). The water table is 30 meters below the ground surface and the entire model pore pressure gradient was set constant to be 9.8 kPa/m (Figure 5-12). It was assumed the wells were drilled in the direction of the maximum horizontal stress, therefore, the stress in the x-direction was the minimum stress.

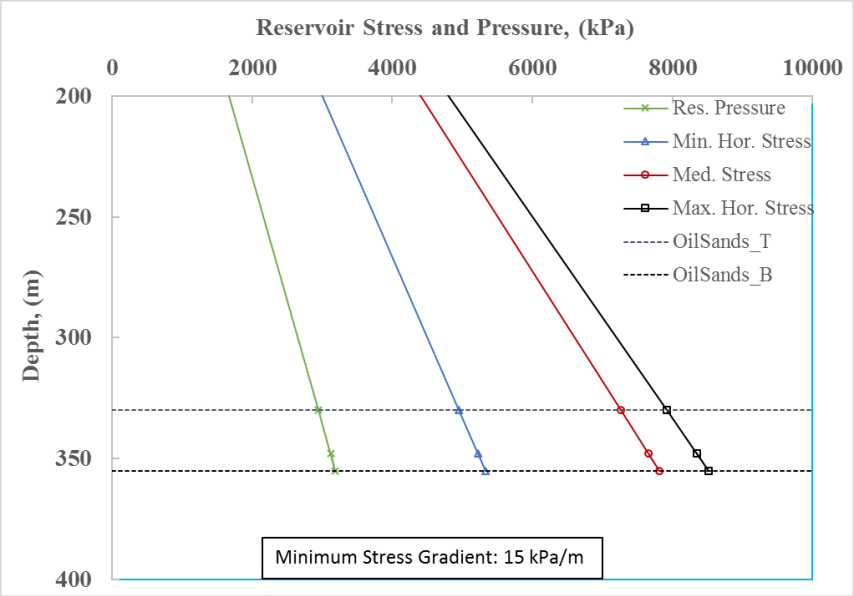

Figure 5-12. 15 kPa/m total stress profile and pore pressure showing the location of the reservoir and the wellbores (two points inside the reservoir).

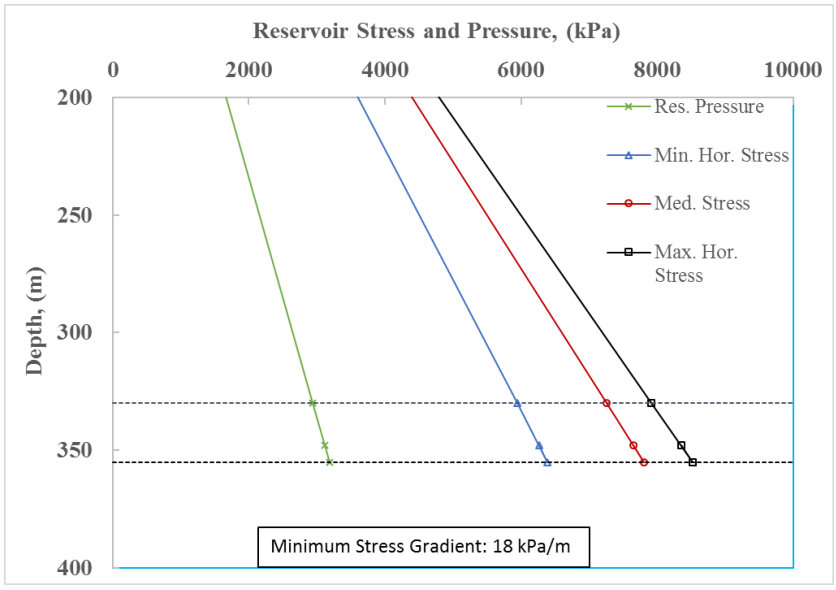

Figure 5-13. 18 kPa/m total stress profile and pore pressure showing the location of the reservoir

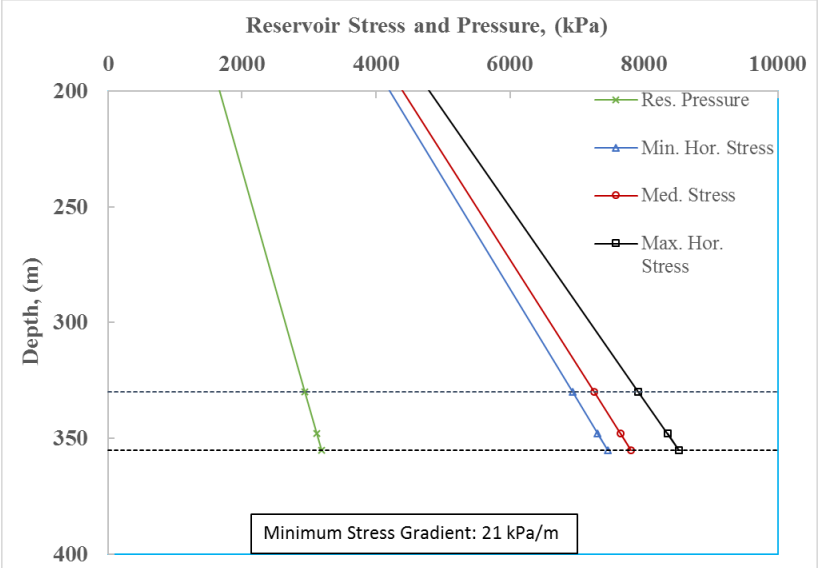

Figure 5-14. 21 kPa/m effective stress profiles showing the location of the reservoir

5.3.5. Mechanical and Flow Boundary Conditions

The mechanical and flow boundary conditions were set assuming that each of the well pairs was injected individually. Constant pressure outer boundaries for flow were imposed far away from the injection wells. The bottom mechanical boundary was allowed to translate horizontally (Figure 5-15). Given the ground surface was not modelled, a stress boundary was applied at the top. The horizontal boundary in the direction of the well pair, in this case, the y-direction, was set to allow translation in the x and z-directions and gradient stress boundary conditions were applied in the x directions.

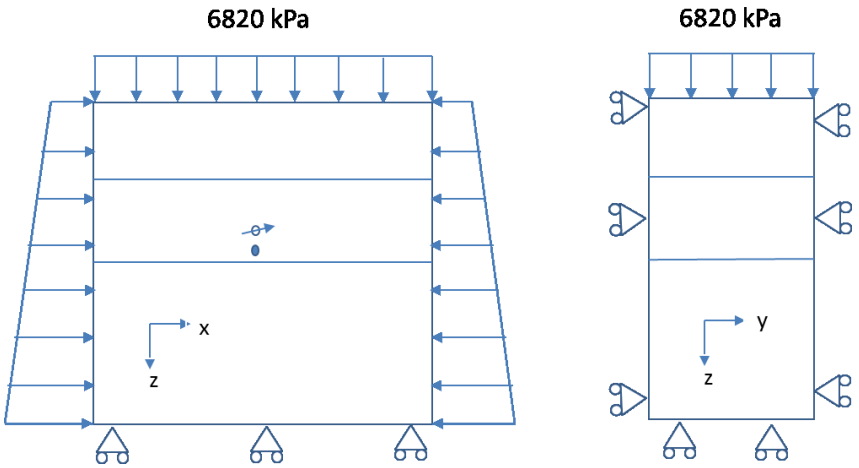

Figure 5-15. Roller and applied stress conditions for the FLAC3D model. The flow boundary conditions were all under constant pressure. (Note: not to scale).

5.4. Assessment on SAGD Performance Due to Dilation Start-Up

A reservoir geomechanical model was developed using the FLAC3D software to simulate the dilation start-up process as an alternative to the conventional SAGD start-up scheme. FLAC3D uses a finite difference scheme to solve the flow equations where the solution is solved at the grid points of the geomechanical simulation grid. The pressure was then interpolated to the zone centres for the mechanical calculations. The finite difference time step was determined for the simulation based on the geometry, permeability, fluid properties, and mechanical properties. The automatic coupling scheme, as implemented in FLAC3D, was used to perform the pore pressure and the mechanical calculations simultaneously. In this scheme, the flow is calculated for a one-time step and then the mechanical displacements corresponding to the changes in effective stress are computed. The changes in Young's modulus are calculated every one second of the flow time, while the permeability update is performed every 5 seconds of the flow time. The maximum simulation time for each injection case is 10 hours unless failure has occurred at the midpoint between the wells.

After computing the geomechanical response and permeability/porosity in the dilated zone after cold-water injection using FLAC3D, the flow simulator CMG STARS was used to simulate the full SAGD performance. Caprock integrity due to dilation start-up was not considered in the numerical simulation and is beyond the scope of this study.

The early stage of the entire SAGD process, including start-up and steam chamber development phases, was analyzed. The impact of injection pressure and steam injection rates on start-up time was evaluated over a time span of the first 200 days after steam commencement.

A list of the data output for each of the simulations is shown in Table 5-5. This data was used as input to the CMG STARS model for SAGD start-up simulation.

Table 5-5. Data output from each FLAC3D simulation at the selected times steps

Mark	Parameters
1	x,y,z Permeability
2	Pore Pressure
3	Porosity
4	Total Volumetric Strain
5	Volumetric Plastic Strain
6	Failure Mode
7	Full Strain Tensor
8	Full Stress Tensor

Cold-water was injected into the top and bottom wells simultaneously. In this case, cold-water was injected at five different pressures for a maximum of 10 hours or until failure was reached at the midpoint between the wells. The injection pressures required for failure were calculated based on the minimum horizontal stress.

Cold-water was continuously injected into both the injector and the producer for 10 hours. Three injection pressure levels (injection factors = 0.5, 1.0, and 1.5) were considered, where the injection factor is defined as the ratio of elevated injection pressure to its critical value corresponding to the onset of geomechanical dilation.

5.4.1. Field-Scale Simulation on SAGD

The field-scale simulation study consists of two main parts. The impacts of injection pressure and initial stress state on the enhanced start-up time, subsequent chamber spreading and the mature operation period were assessed individually.

The same mesh of 100 m by 100 m in the x- and z- directions ($\Delta x = \Delta z = 0.5$ m) was used for both the flow simulation model (in CMG STARS) and the geomechanics model (in FLAC3D), as shown in Figure 5-16. Only 0.2 m of the

horizontal wellbore length, which is along the y-direction, was modelled with Δy = 0.1 m. The production well was located at 1.0 meter above the bottom of the reservoir, and the injector was positioned 5.0 meters above the producer.

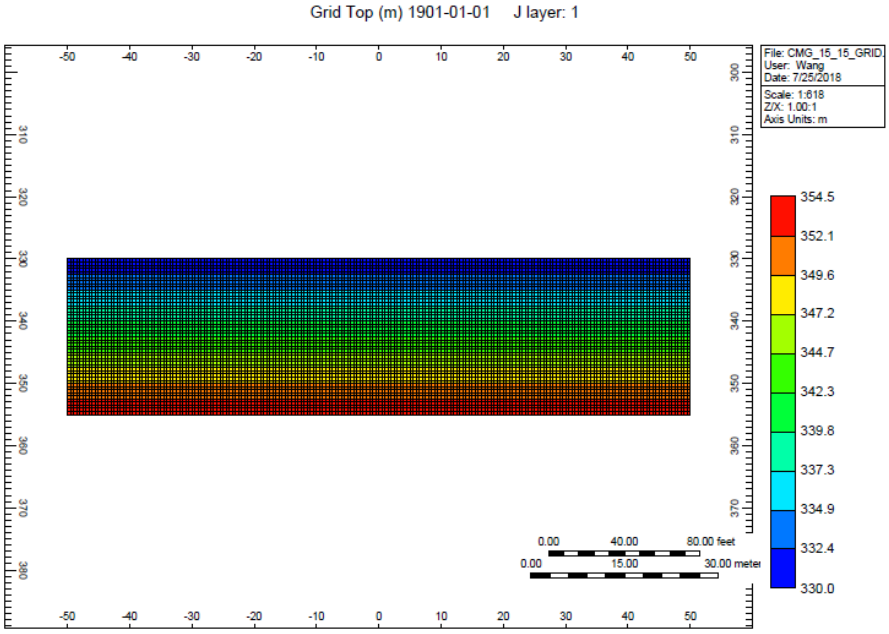

Figure 5-16. CMG STARS geometry for SAGD performance assessment modelling

The production well was located 1.0 meters above the bottom of the reservoir and the injector was positioned 5.0 meters above the producer. During the first stage, the impact of injection pressure on shortening the start-up time was evaluated.

The impact of geomechanical behaviour on oil production was investigated during the steam chamber development.

5.4.1.1. Initial Reservoir Properties

Initial reservoir properties (e.g., permeability, porosity), fluid (water and oil) saturation, as well as other parameters, prior to any start-up operations are summarized in Table 5-6.

Table 5-6. Summary of properties for the fluid-flow thermal model used in CMG STARS

Formation	Property	Units	Original Value
Oil Sands	Porosity, (Φ)	(%)	28
	Thickness(m)	m	25
	Initial Permeability, (K_x)	mD	3000
	Initial Permeability, (K_y)	mD	3000
	Initial Permeability, (K_z)	mD	1500
	Water Saturation, (S_w)	(%)	25
	Oil Saturation, (S_o)	(%)	75
	Thermal Conductivity	(J/m·day·°C)	2.74×10^5
	Initial Temperature	(°C)	10
	Initial Pore Pressure	(kPa)	3,000

The SAGD performance was examined in terms of fluid production rate and cumulative amount, steam oil ratio (SOR) and cumulative SOR (CSOR). As a comparison, a homogenous formation was assessed, which possessed the same vertical permeability, horizontal permeability, porosity, fluid saturation across the entire formation. The numerical simulation results were summarized in the following paragraphs. In the figures below each case was presented by two numbers, where the first number specifies the stress state (e.g. 15 kPa/m) as the minimum stress gradient, and the second number indicates the injection factor (e.g. 05 refers to injection factor, f=0.5).

5.4.1.2. Steam-Based SAGD Start-up Strategy

The impact of steam injection pressure on the start-up time required for establishing inter-well communication was examined. Steam circulation is the default start-up method for most existing SAGD projects; it involves injecting steam down the tubing of each well producing the condensed water from the annulus. The near-wellbore region is heated initially by conduction and the oil viscosity is decreased. Communication between wells is established as oil mobility increases and steam/water flows into the oil sands.

A conventional sink/source model was used in the CMG simulations. An injector and a producer were located at the same wellbore to mimic steam injection into the tubing and fluid production from the annulus. Different levels of bottom hole pressure (BHP) were tested. A pressure differential of 100 kPa was maintained between the well pairs to promote hydraulic and thermal communication. A relatively large well index is needed to achieve the necessary injectivity. A geomechanical model was used to analyze the dilation and permeability change. One injection pressure was tested, which was a modest 3500 kPa.

5.4.2. SAGD Performance due to Dilation Start-up

Recall that two stages were carried out to assess the impacts of dilation start-up on SAGD performance. During the first stage, the impact of injection pressure on the SAGD overall performance was evaluated. During the second stage, the impact of initial stress states on the SAGD performance was evaluated. Three cases with the elevated minimum stress states of 15, 18, and 21 kPa/m were tested.

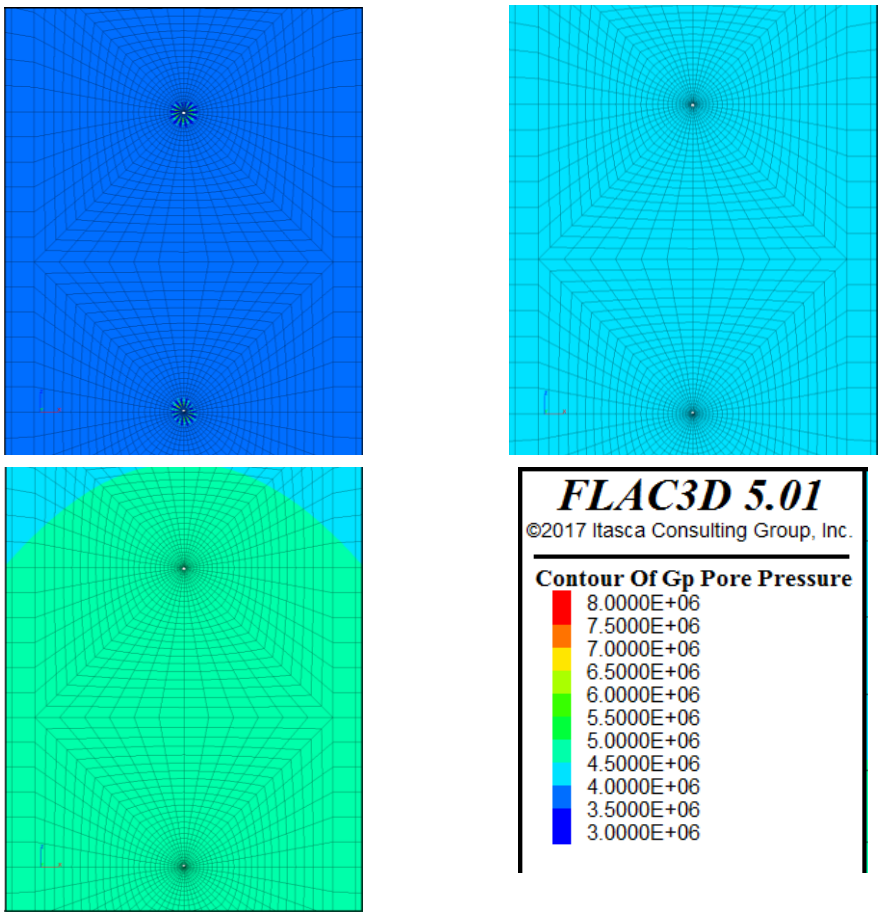

Figure 5-17. Pore pressure distribution due to cold-water under the minimum stress gradient of 15 kPa/m, with an injection factor of 0.5, 1.0, and 1.5 from left to right and to bottom, respectively.

5.4.2.1. SAGD Performance under Elevated Injection Pressure

As water injection and pore pressure increased, the effective stress in the formation decreased accordingly. After completing cold-water injection from both wells for 10 continuous hours, the pore pressure gradually approached the injection pressure in the inter-well areas, specifically around the wells.

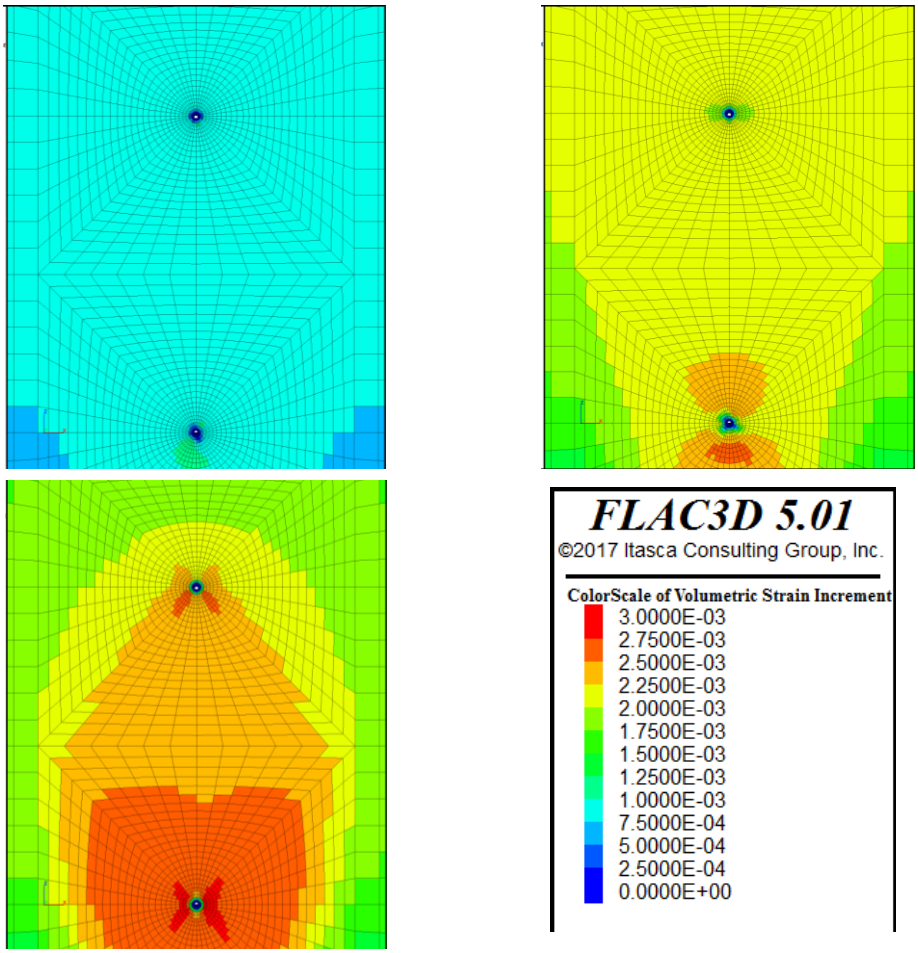

Figure 5-18. Volumetric strain distribution due to cold-water injection under the minimum stress gradient of 15 kPa/m, with injection factor of 0.5, 1.0, and 1.5 from left to right and to bottom, respectively

Figure 5-17 depicts the pore pressure distribution at the end of the cold-water injection under the minimum stress gradient of 15 kPa/m, with an injection factor of 0.5, 1.0, and 1.5 from left to right and to bottom, respectively.

The volumetric strain varied with effective stress, which can be noted in Figure 5-18. Some zones in the inter-well formation can be found with plastic change or mechanical failure in Figure 5-19.

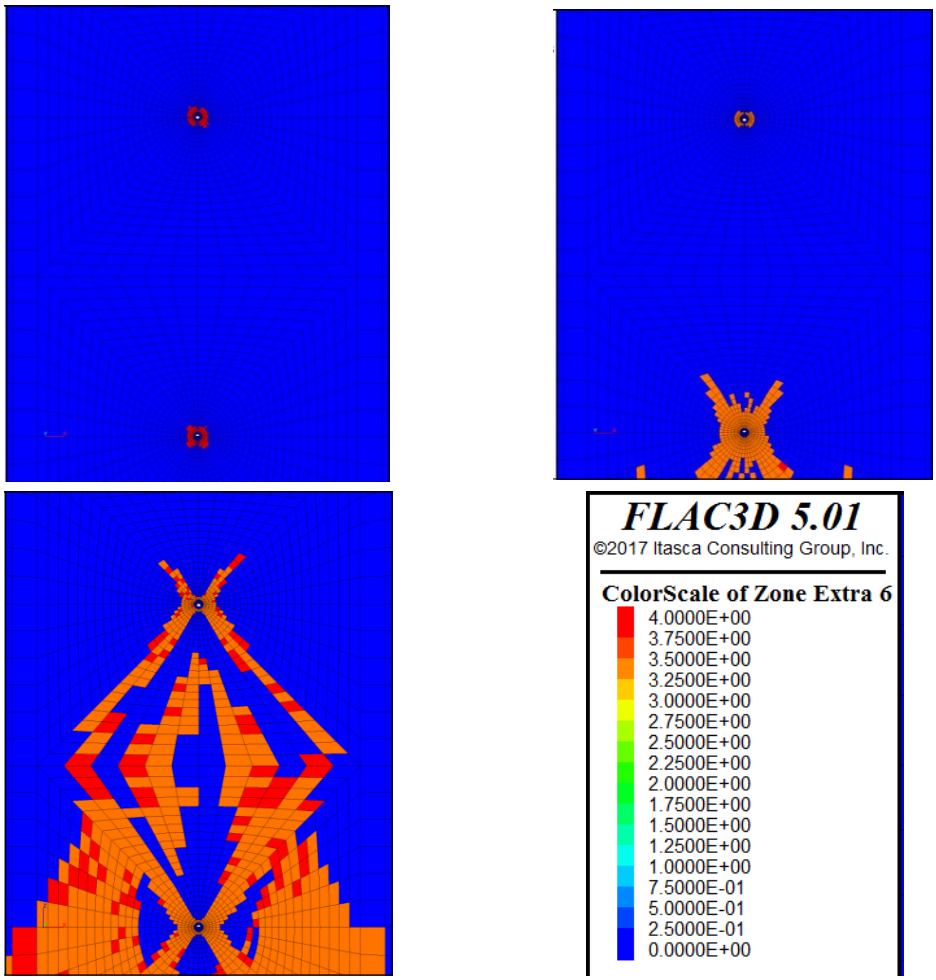

Figure 5-19. Failure zone distribution due to cold-water injection under the minimum stress gradient of 15 kPa/m, with injection factor of 0.5, 1.0, and 1.5 from left to right and to bottom, respectively

The dilated zones started around the injector and the producer, and then expanded gradually towards the well which was 5 meters away. Under the injection factor condition of 0.5, the injection pressure was not sufficiently high to trigger a big area except for the regions near the wellbores.

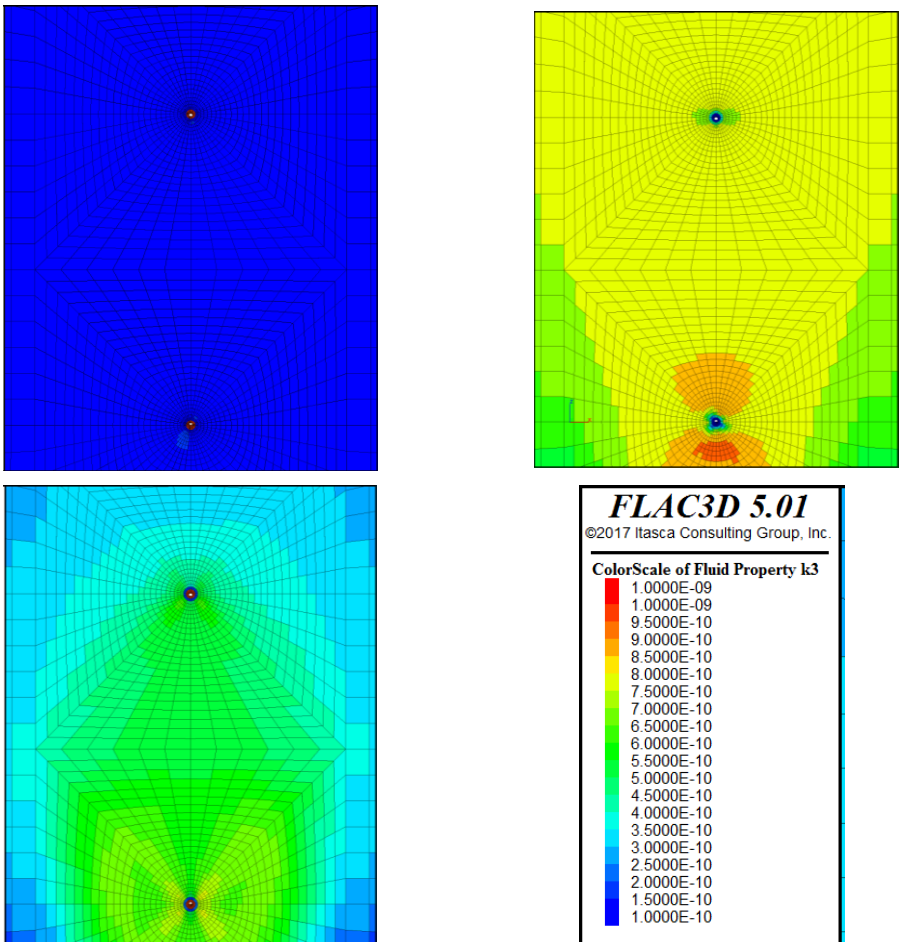

Figure 5-20. Updated vertical permeability distribution due to cold-water injection under the minimum stress gradient of 15 kPa/m, with injection factor of 0.5, 1.0, and 1.5 from left to right and to bottom, respectively

Figure 5-19 indicates that a lower injection pressure was not sufficient to induce or generate permanent dilation. When a relatively high pressure was used, as with the injection factor of 1.5, the failure zone contour is shown in the bottom left of Figure 5-19. The pressure distribution was quite uniform across the formation, specifically around the wells.

The vertical permeability changes are compared, corresponding to three cases with different injection factors (Figure 5-20). The effective permeability was dramatically enhanced in the dilated zones in the third case with an injection factor of 1.5 under the minimum stress gradient of 15 kPa/m. For the case with an injection factor of 0.5, shown in the top left contour of Figure 5-20, the effective permeability was almost unchanged in the dilated zones due to an insignificant change in porosity.

As discussed above, some of the transition areas within the well pair reached the failure state under the favourable stress conditions. With the increasing pore volume, the water saturation increased accordingly. The total amount of oil and the total bulk volume were assumed to remain unchanged, so oil saturation slightly decreased. Figure 5-21, Figure 5-22, and Figure 5-23 display corresponding changes in terms of the distributions of the porosity, water saturation, and oil saturation at the end of cold-water injection as SAGD start-up.

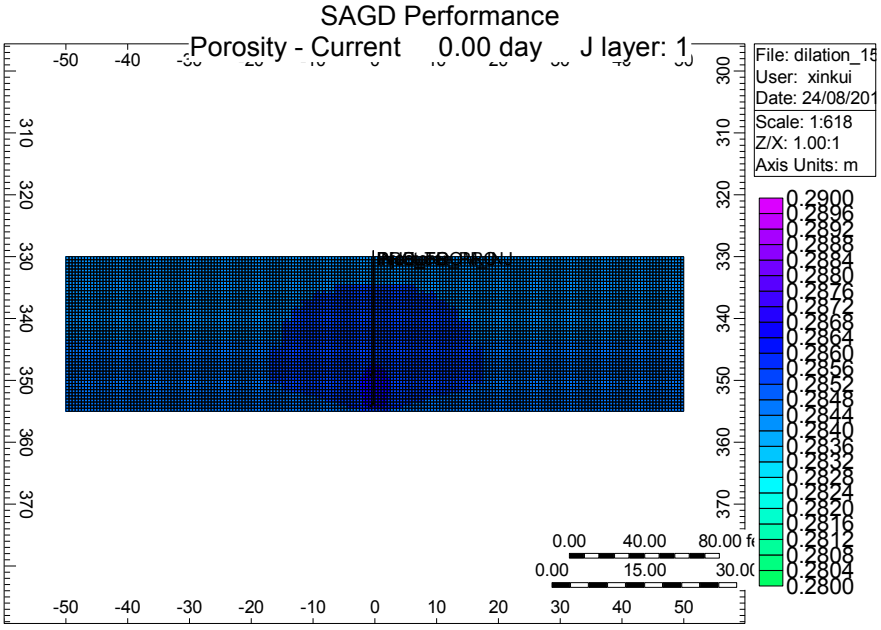

Figure 5-21. Porosity distribution at the end of cold-water injection as SAGD start-up, followed by steam circulation and full SAGD operation under the minimum stress gradient of 15 kPa/m, with an injection factor of 1.5

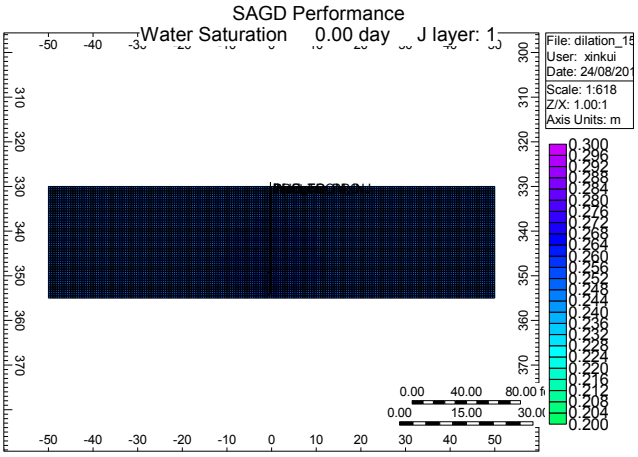

Figure 5-22. Water saturation distribution at the end of cold-water injection as SAGD start-up, followed by steam circulation and full SAGD operation under the minimum stress gradient of 15 kPa/m, with injection factor of 1.5

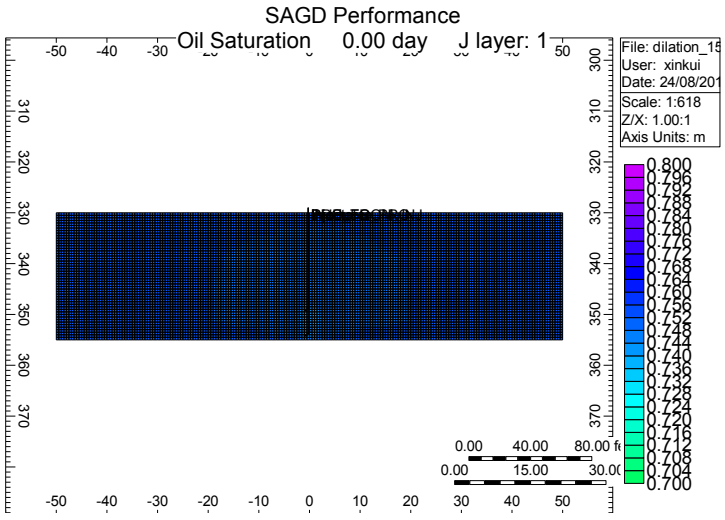

Figure 5-23. Oil saturation distribution at the end of cold-water injection as SAGD start-up, followed by steam circulation and full SAGD operation under the minimum stress gradient of 15 kPa/m, with injection factor of 1.5

At the end of the cold-water injection, steam was injected into both the injector and producer to start conventional steam circulation. The bottom hole pressure was maintained at the maximum pressure of 3300kPa. The steam quality was set at 0.9 and the injection rate was set at 0.2 tons/day. As the length of the wellbore was pre-set at 1.0 meter. In terms of the full length (800 meters) of a wellbore in an average SAGD field, the steam rate was equivalent to 160 tons/day.

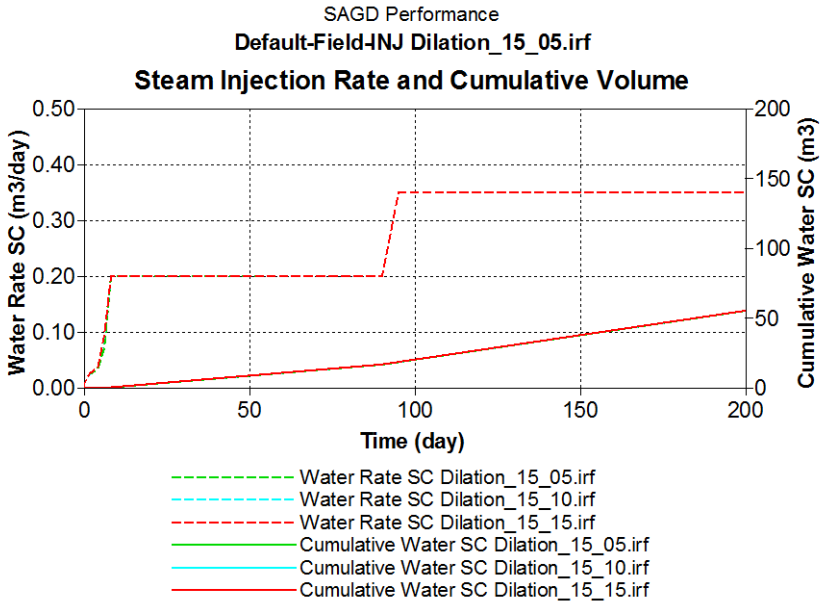

Figure 5-24. Following dilation start-up, SAGD performance in terms of injection rate and cumulative volume of steam under the minimum stress gradient of 15 kPa/m, with injection factor of 0.5, 1.0, and 1.5, respectively

The steam rate and the cumulative steam injection are shown in Figure 5-24. The steam circulation stage was switched to the full SAGD stage on the 90th day after steam commencement. From the perspective of the temperature contour, the steam chamber developed vertically and laterally, which was performed well. During the steam circulation stage, the steam rate was initially 0.20 tons/day. This was then increased to 0.35 tons/day on the 90th day when steam circulation was terminated, and the well pair was switched to full SAGD stage. The steam injection patterns were the same in both steam rate and duration for all scenarios studied. At the end of steam circulation, thermal communication was established in the inter-well region. On the 90th calendar day, the temperature exceeds 160 °C in the region between the injector and the producer.

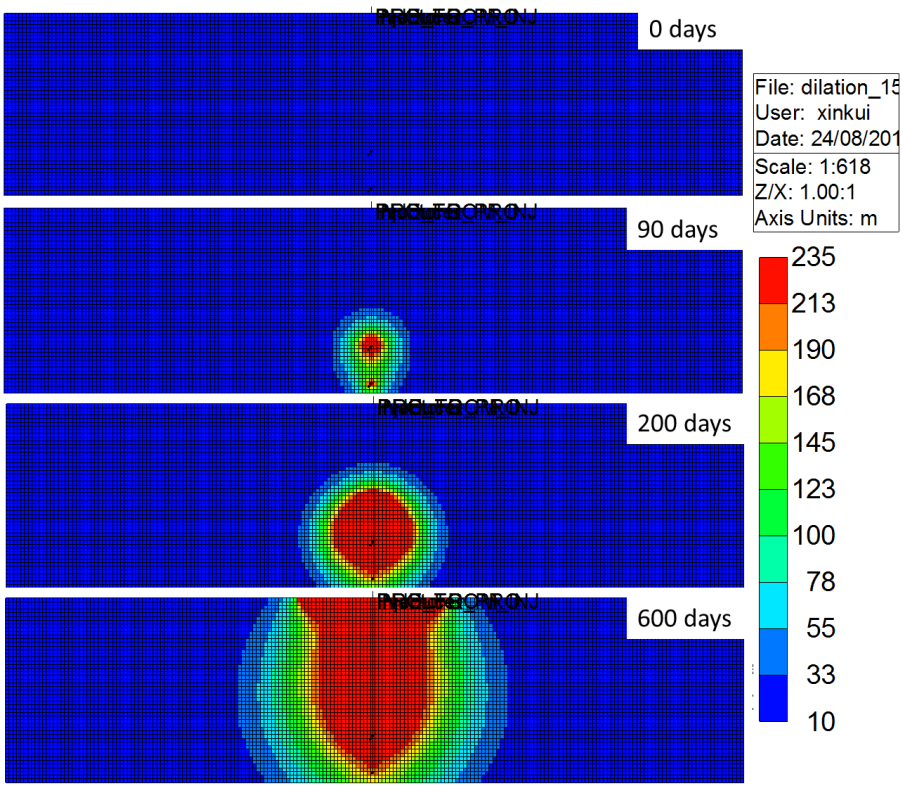

Figure 5-25. Following dilation start-up, temperature distribution under the minimum stress gradient of 15 kPa/m, with injection factor of 1.5 at the injection time of 0 days, 90 days, 200days, and 600 days respectively

At the end of steam circulation, the steam chamber developed well, as noted by the temperature contour shown in Figure 5-25. On the 90th calendar day, the temperature in the mid area between the injector and the producer was over 160 °C, which was high enough to assure the well pairs thermally and hydraulically communicated.

Figure 5-26, Figure 5-27, Figure 5-28, and Figure 5-29 show insignificant impacts of the injection pressure on the water production rate, oil production rate, the cumulative oil production, and the cumulative gas production.

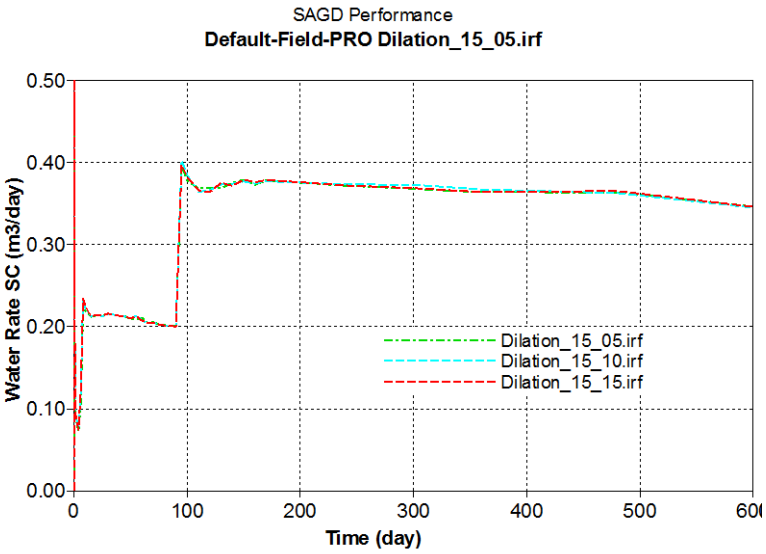

Figure 5-26. Following dilation start-up, SAGD performance in terms of water production rate under the minimum stress gradient of 15 kPa/m, with injection factor of 0.5, 1.0, and 1.5, respectively

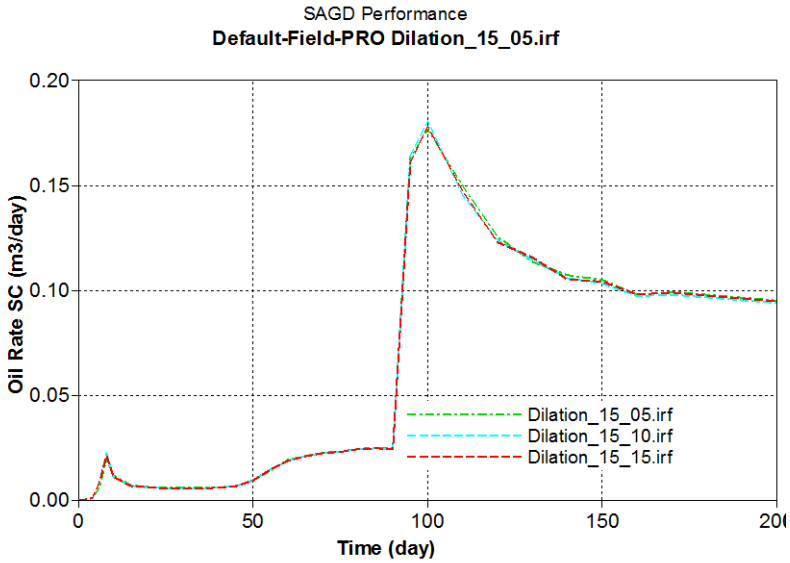

Figure 5-27. Following dilation start-up, SAGD performance in terms of oil production rate under the minimum stress gradient of 15 kPa/m, with injection factor of 0.5, 1.0, and 1.5, respectively

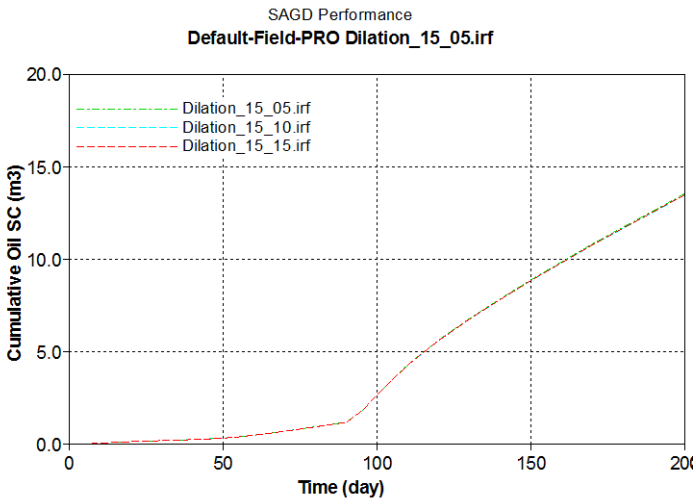

Figure 5-28. Following dilation start-up, SAGD performance in terms of cumulative oil production under the minimum stress gradient of 15 kPa/m, with injection factor of 0.5, 1.0, and 1.5, respectively

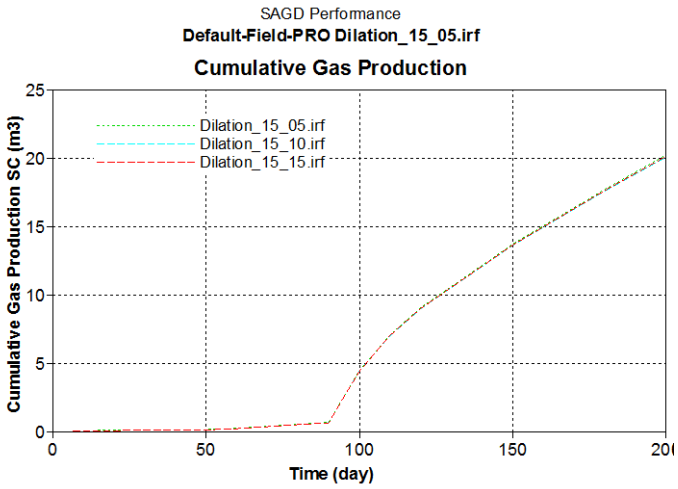

Figure 5-29. Following dilation start-up, SAGD performance in terms of cumulative gas production under the minimum stress gradient of 15 kPa/m, with injection factor of 0.5, 1.0, and 1.5, respectively

At the end of the 200th production day, the SAGD well pair yielded 13.1 m^3 of cumulative oil and 20.0 m^3 of cumulative oil, as shown in Figure 5-28, and Figure 5-29, respectively.

Figure 5-30 shows some impacts of the injection pressure on the cumulative gas-oil ratio (cGOR). Starting with 1.90 (m^3/m^3), cGOR abruptly dropped on the 6th day and reached a minimum at 0.45 (m^3/m^3) for the injection factor of 0.5; and 0.48 (m^3/m^3) and 0.57 (m^3/m^3) for the injection factor of 1.0 and 1.5 respectively on the 50th calendar day.

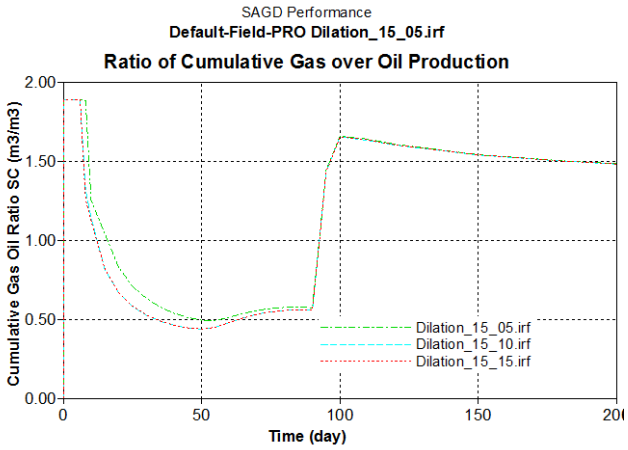

Figure 5-30. Following dilation start-up, SAGD performance in terms of cumulative gas oil ratio under the minimum stress gradient of 15 kPa/m, with injection factor of 0.5, 1.0, and 1.5, respectively

It can be found that once the well-pair finished steam circulation and turned to the regular SAGD stage, the cGOR jumped to 1.66 (m^3/m^3) for each injection factor condition.

Figure 5-31 shows some slight impacts of the injection pressure on the steam oil ratio (SOR). The impacts were mainly reflected at the steam circulation stage rather than the regular SAGD stage. After the 50th day since the steam commencement, the SOR profiles overlapped one another. The SOR increased slightly and slowly within the range of 2.1 and 3.8.

Figure 5-32 shows the impacts of the injection pressure on the cumulative steam-oil ratio (cSOR). No significant impacts were found on the cSOR except for the early steam circulation stage.

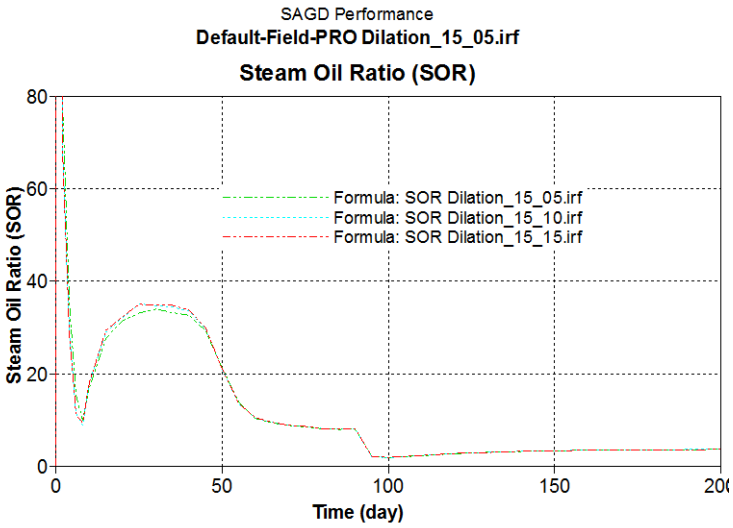

Figure 5-31. Following dilation start-up, SAGD performance in terms of steam oil ratio under the minimum stress gradient of 15 kPa/m, with injection factor of 0.5, 1.0, and 1.5, respectively

On the 40th day of the steam commencement, the cSOR reached the maximum value of 30 under the minimum stress gradient of 21 kPa/m. Then, the cSOR decreased gradually and slowly within the range of 5.0 and 4.2.

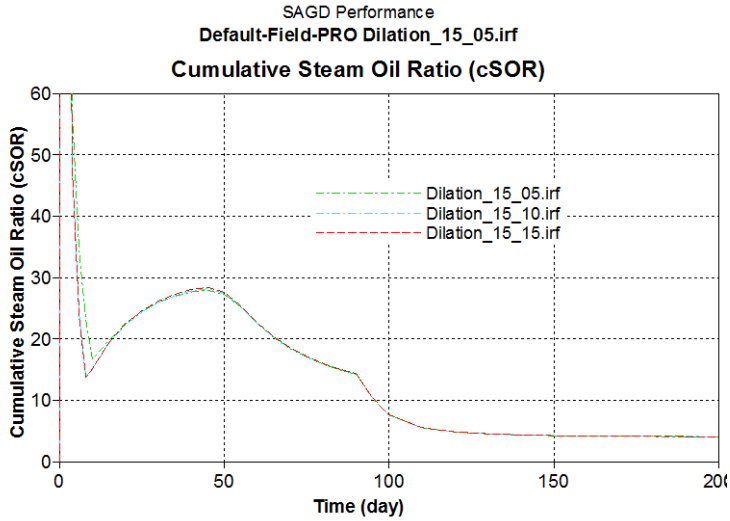

Figure 5-32. Following dilation start-up, SAGD performance in terms of cumulative steam-oil ratio under the minimum stress gradient of 15 kPa/m, with injection factor of 0.5, 1.0, and 1.5, respectively

5.4.2.2. SAGD Performance under Different Stress State

The updated effective permeability at the end of cold-water injection is displayed in Figure 5-20. The permeability to water 6.0×10^{-11}(m^3·sec/kg), which was (60 mD) enhanced to 6.0×10^{-11} (m^{3}sec/kg), which was (604 mD).

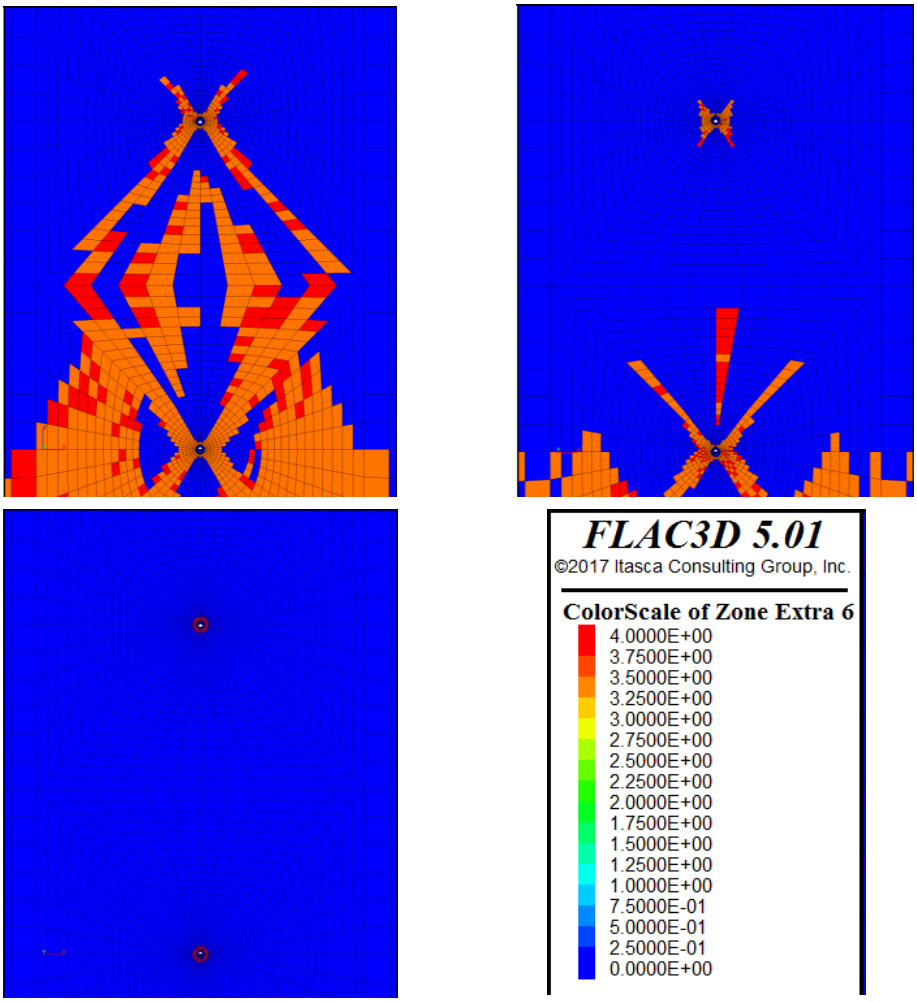

Figure 5-33. Failure zone distribution due to cold-water under the minimum stress gradient of 15 kPa/m, 18kPa/m, and 21kPa/m with injection factor of 1.5 from left to right and to bottom, respectively

Under the lower minimum stress gradient of 15 kPa/m, the stress ratio reached the lowest and the most favourable initial stress condition to generate permanent dilation. It can be noted in Figure 5-33.

Under the minimum stress gradient of 15 kPa/m, the dilation zones were widely developed across the injection well and production well areas and connected each other between the well pair.

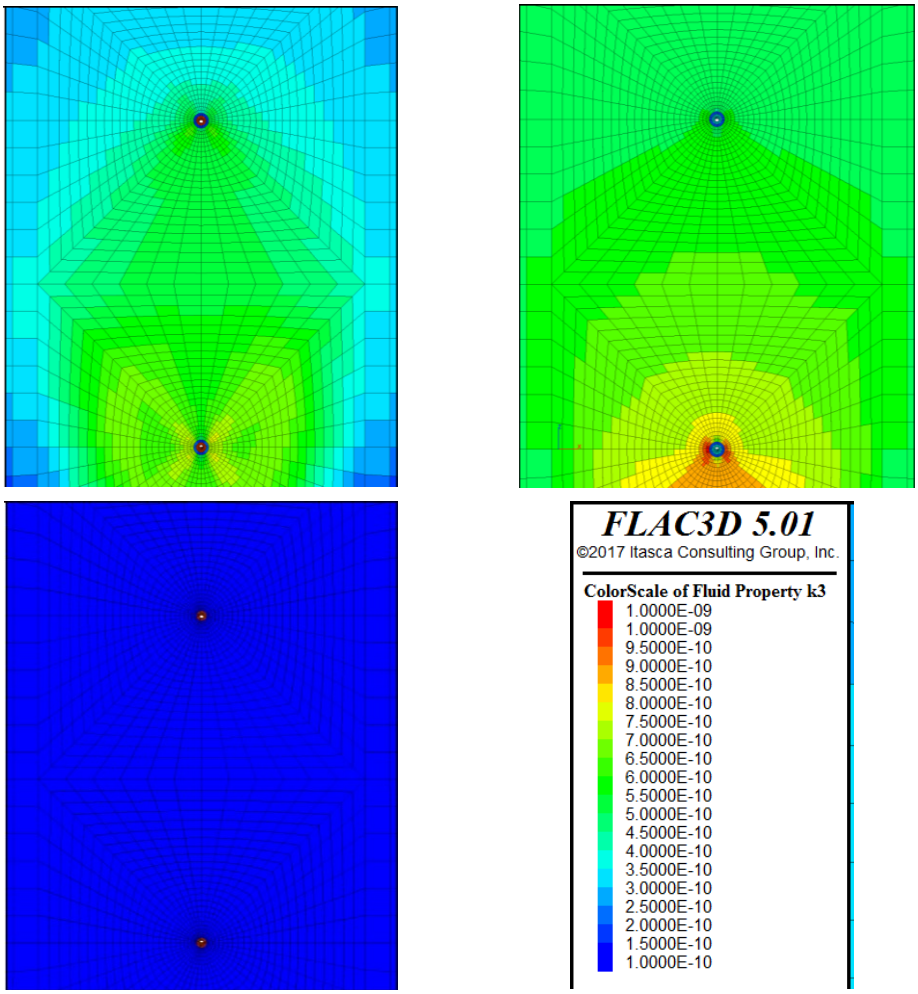

Figure 5-34. Vertical permeability distribution due to cold-water under the minimum stress gradient of 15 kPa/m, 18kPa/m, and 21kPa/m with injection factor of 1.5 from left to right and to bottom, respectively

However, in the cases where the minimum stress gradient was 18 and 21 kPa/m, the stress ratios were not favourable in creating plastic dilation. In addition, failure zones did not develop widely and connect with the adjacent well. Especially, for the latter case (21 kPa/m), failure zones are limited to the areas within the vicinity of the wells. Under the minimum stress gradient of 21 kPa/m, the stress ratio approached one, which was close to the isotropic stress state.

The vertical permeability changes are compared between three cases with different minimum stress gradients, as shown in Figure 5-34. The effective permeability was dramatically enhanced in the dilated zones in the first case under the minimum stress gradient of 15 kPa/m. Under the minimum stress gradient of 21 kPa/m, the effective permeability was almost unchanged in the dilated zones due to an insignificant change in porosity.

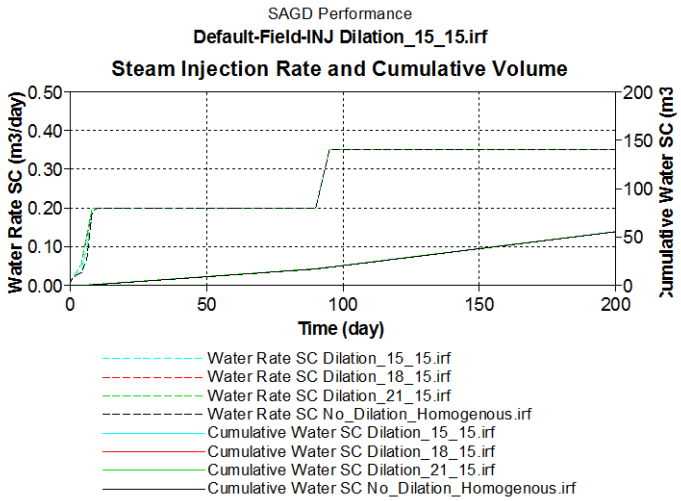

Figure 5-35. Following dilation start-up, SAGD performance in terms of steam injection rate and cumulative steam volume under the minimum stress gradient of 15, 18, 21 kPa/m with injection factor of 1.5, respectively

After the oil sands formations had undergone cold-water injection, the high quality of steam was then pumped into both the injection well and the production well. The water rate increased to around 0.21 m^3/day from 0.10 m^3day on the 10^{th} day and then to 3.80 m^3/day on the 90^{th} day. The differences in water rate between the different initial stress states (15, 18, and 21 kPa/m) were insignificant.

The results of the water injection scheme showed an insignificant enhancement of 2-3 % in oil production rate for the dilation start-up scheme compared to no dilation within the first 200 days as shown in Figure 5-36, the cumulative oil production in Figure 5-37, cumulative water production in Figure 5-38, cumulative gas production in Figure 5-39. This indicates that the cold-water injection did not lead to significant production improvement in SAGD operations.

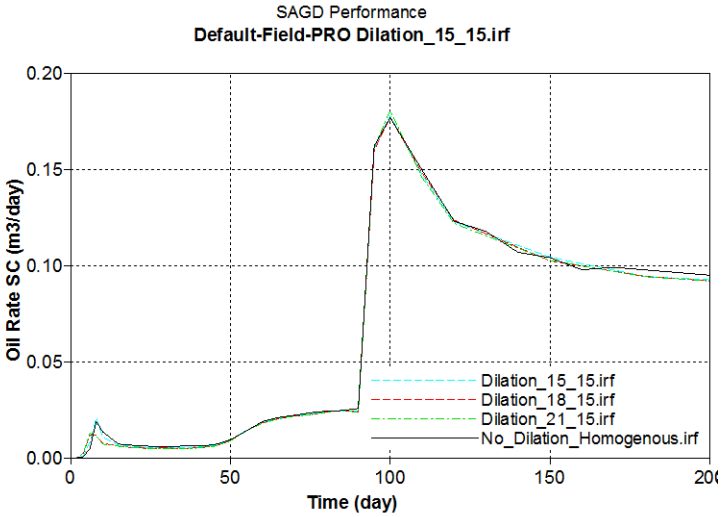

Figure 5-36. Following dilation start-up, SAGD performance in terms of cumulative gas production under the minimum stress gradient of 15, 18, 21 kPa/m with injection factor of 1.5, respectively

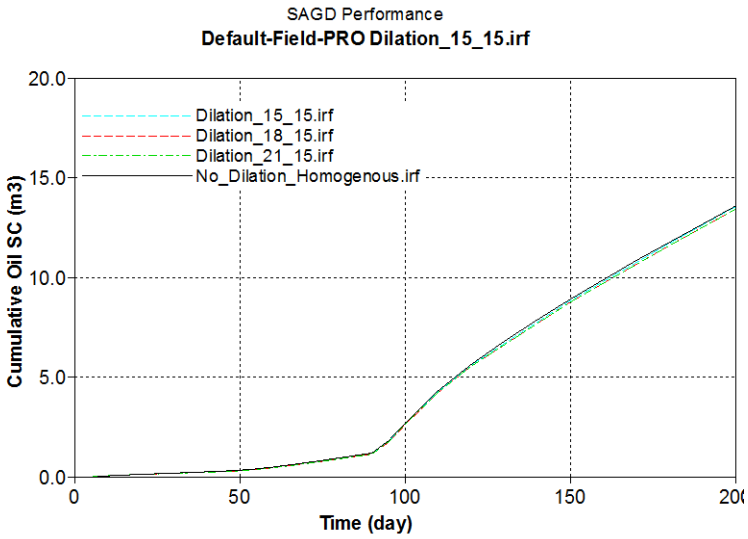

Figure 5-37. Following dilation start-up, SAGD performance in terms of Oil production rate under the minimum stress gradient of 15, 18, 21 kPa/m with injection factor of 1.5, respectively

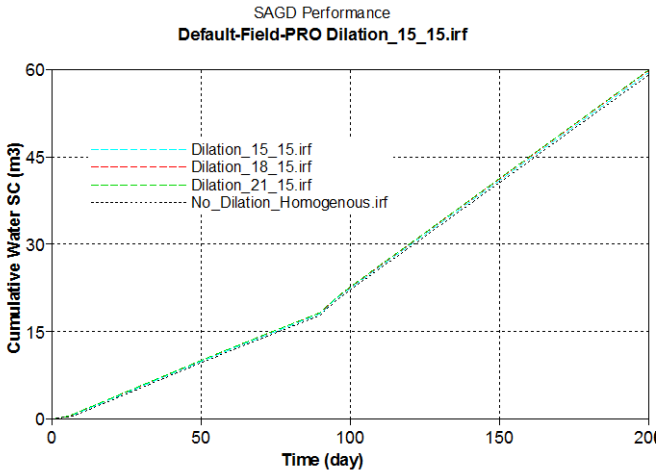

Figure 5-38. Following dilation start-up, SAGD performance in terms of cumulative water production under the minimum stress gradient of 15, 18, 21 kPa/m with injection factor of 1.5, respectively

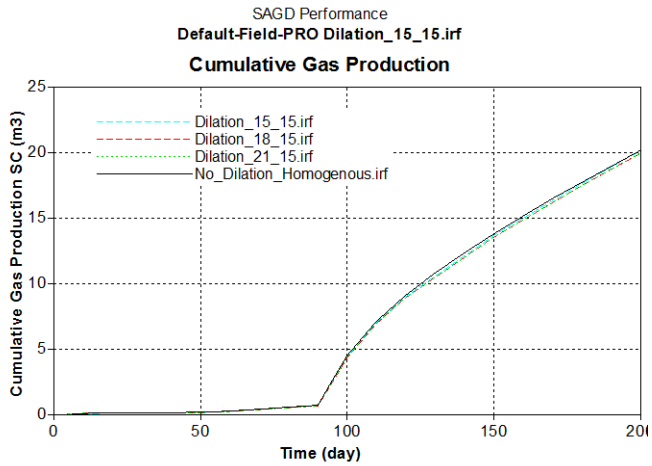

Figure 5-39. Following dilation start-up, SAGD performance in terms of cumulative gas production under the minimum stress gradient of 15 kPa/m, with injection factor of 0.5, 1.0, and 1.5, respectively

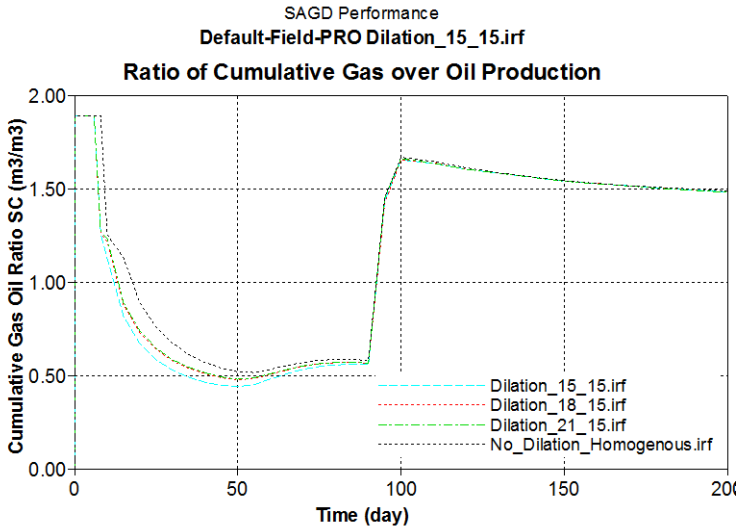

Figure 5-40. Following dilation start-up, SAGD performance in terms of cumulative gas oil ratio under the minimum stress gradient of 15 kPa/m, with injection factor of 0.5, 1.0, and 1.5, respectively

Considering the steam oil ratio (SOR) and the cumulative SOR (cSOR), the simulation results showed an insignificant enhancement of 5-10% in the early steam circulation stage (shown in Figure 5-41 and Figure 5-42). After the well pair switched to full SAGD, no difference in SOR and cSOR were apparent among the three cases.

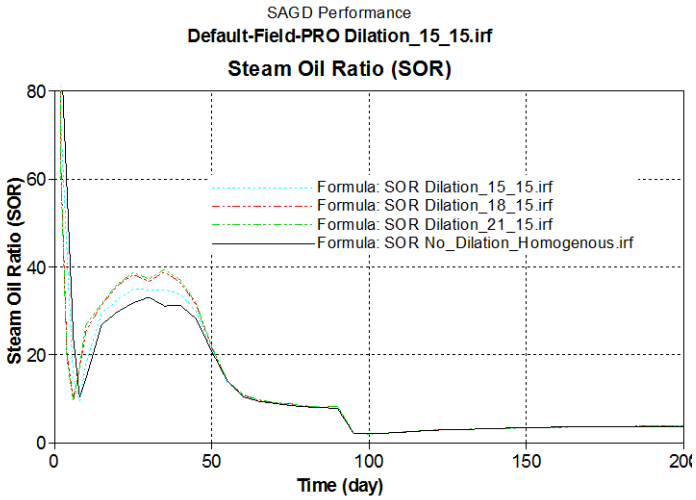

Figure 5-41. Following dilation start-up, SAGD performance in terms of steam oil ratio under the minimum stress gradient of 15, 18, 21 kPa/m with injection factor of 1.5, respectively

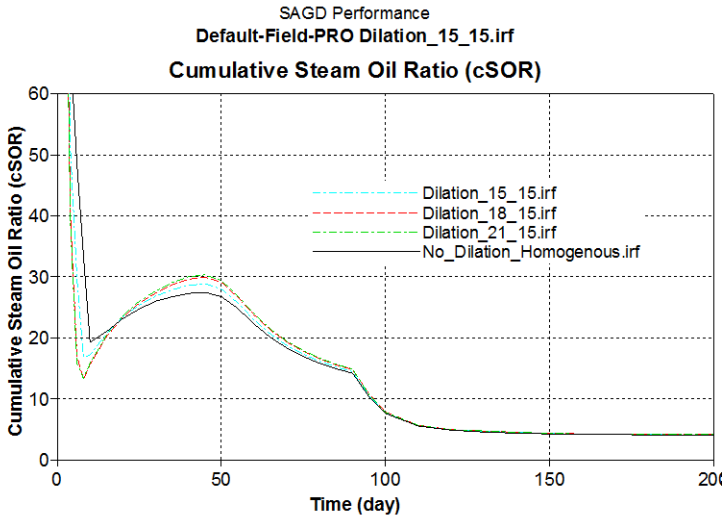

Figure 5-42. Following dilation start-up, SAGD performance in terms of cumulative steam-oil ratio under the minimum stress gradient of 15, 18, 21 kPa/m with injection factor of 1.5, respectively

5.4.2.3. Impacts of Relative Permeability Curve on SAGD Performance

In the previous set of simulation studies, it was clear that enhancement in absolute permeability in the near-well region does not improve long-term SAGD production. However, the experimental studies in Chapters 3 & 4 seem to suggest that it is the effective permeability to water that is enhanced during the dilation process. Therefore, in this section, the potential impact of relative permeability enhancement is explored. Previously, the relative permeability function is unchanged during the geomechanical dilation start-up.

The set of lab-scale on cold-water injection tests demonstrated some very thought-provoking tests. On one hand, tests on the bitumen-free sands core specimen revealed that there is a slight reduction in absolute permeability with decreasing effective stress. On the other hand, tests on the bitumen-filled sands core specimens showed a dramatic enhancement in the effective permeability to water. Other studies have also shown that the effective permeability varies more significantly than absolute permeability in response to variations in stress stage (Li, 2006).

It is challenging to measure the relative permeability functions during geomechanical dilation. Therefore, a sensitivity analysis is formulated by postulating that the relative permeability endpoint is shifted as a result of varying effective stress. The original relative permeability curve used in this study is shown as K_{row} and K_{rw} in Figure 5-43.

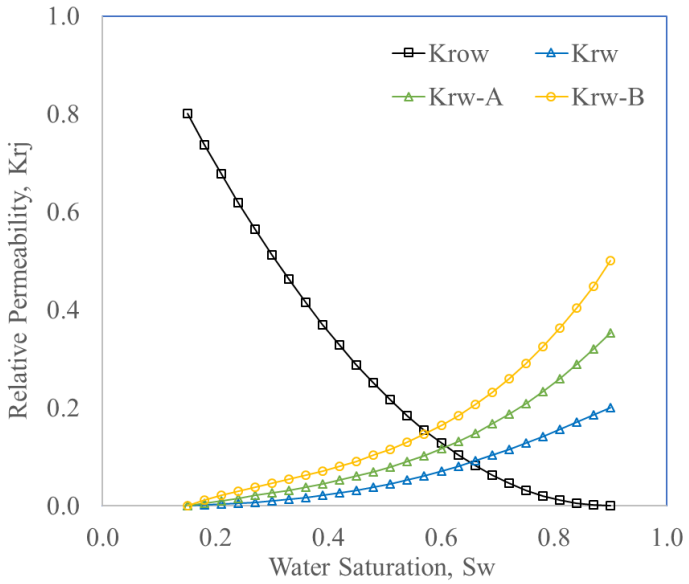

Figure 5-43. Relative Permeability Curve in CMG, with the endpoint of K_{rw}=0.20, K_{rw} -A=0.35, and K_{rw} -B=0.50 at S_w=0.9

Two additional water relative permeability functions are modified from the original one by increasing the endpoint to 0.35 and 0.50 for "Krw-A" and "Krw-B", respectively.

The oil relative permeability function remains unchanged, considering the extremely high viscosity of bitumen at the reservoir temperature, it is challenging to obtain the effective permeability to oil.

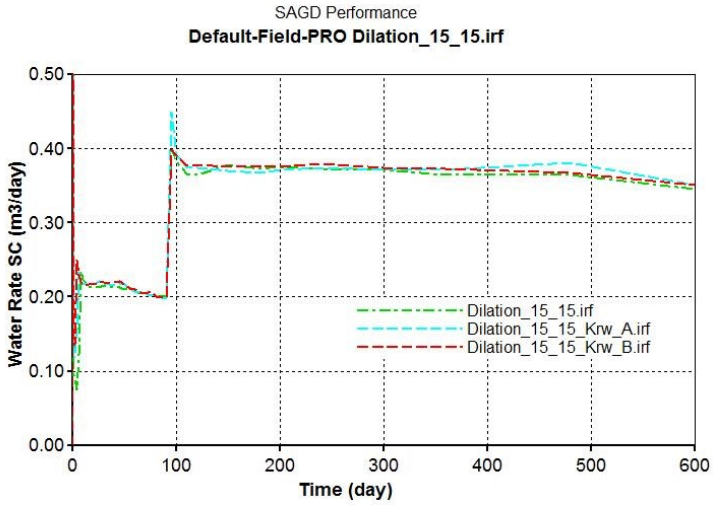

Figure 5-44. Impacts of the relative permeability curve on SAGD performance in terms of water rate under the minimum stress gradient of 15kPa/m with the injection factor of 1.5

Figure 5-44 shows the impacts of the relative permeability curve on SAGD performance in terms of water rate under the minimum stress gradient of 15kPa/m with the injection factor of 1.5. It can be noted that the relative permeability to water with different endpoints had insignificant impacts on water production even though the relative permeability to water was doubled.

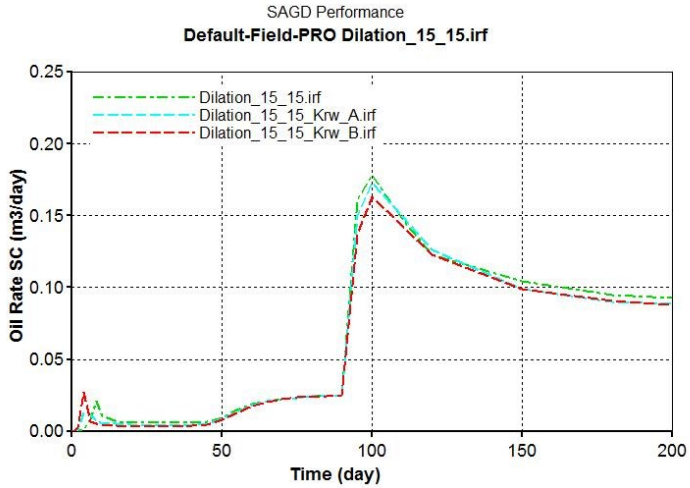

Figure 5-45. Impacts of the relative permeability curve on SAGD performance in terms of oil rate under the minimum stress gradient of 15kPa/m with the injection factor of 1.5

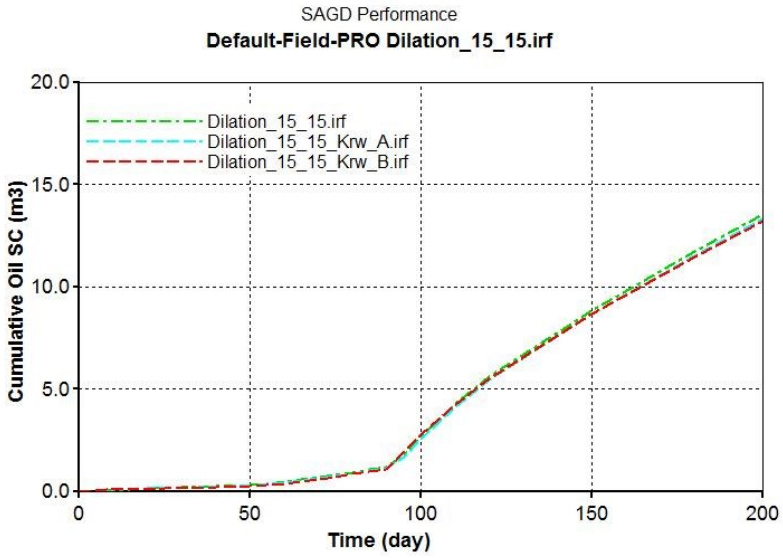

Figure 5-46. Impacts of the relative permeability curve on SAGD performance in terms of cumulative oil production under the minimum stress gradient of 15kPa/m with the injection factor of 1.5

Figure 5-45 and Figure 5-46 shows the impacts of the relative permeability curve on SAGD performance in terms of oil rate and cumulative oil production, respectively. It can be noted that the oil rate was slightly lower if the relative permeability to water function has a higher endpoint (recall the functions K_{rw}-A and K_{rw}-B).

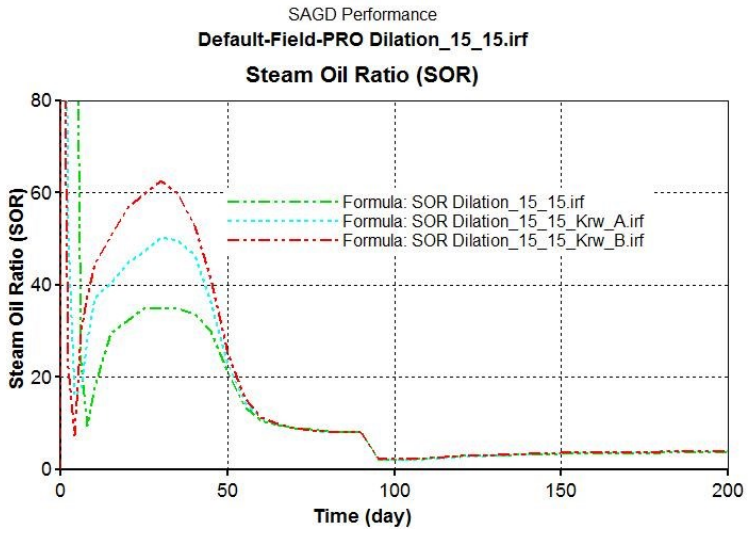

Figure 5-47. Impacts of the relative permeability curve on SAGD performance in terms of steam oil ratio under the minimum stress gradient of 15kPa/m with the injection factor of 1.5

The simulation results showed that water production seemed to be more sensitive to the relative permeability to water. The formation was favourable to steam flow with the increasing relative permeability to water.

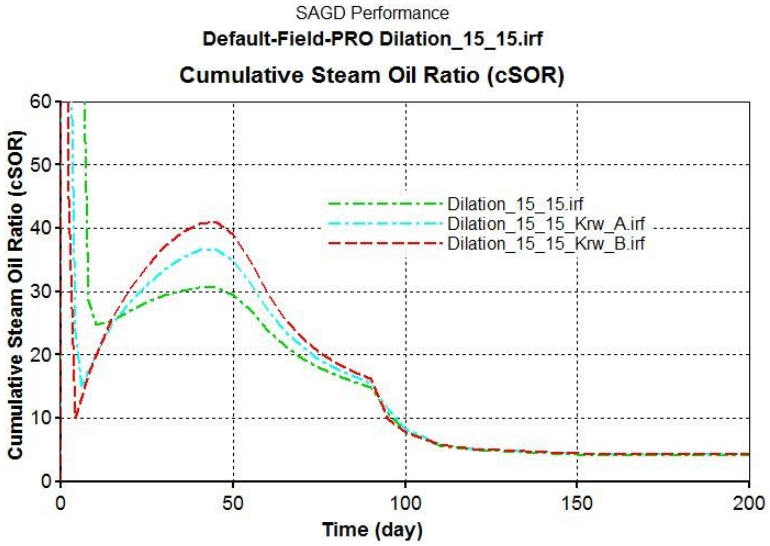

Figure 5-48. Impacts of the relative permeability curve on SAGD performance in terms of cumulative steam-oil ratio under the minimum stress gradient of 15kPa/m with the injection factor of 1.5

5.5. Discussion and Conclusions

As presented in Chapter 5, a reservoir model was developed in the numerical simulation study. It was verified that the reservoir model could examine and assess the potential of cold-water injection as a dilation start-up scheme for SAGD.

This reservoir geomechanical-coupled model was run on a geomechanical simulator, Itasca's FLAC3D. Single-phase fluid flow models were developed from the set of lab-scale tests for the oil sands formation. The relationship of the plastic volumetric strain versus the permeability enhancement was applied to the dilation process in the cell-model rather than in the full-size SAGD model. As the high temperature existed in the full SAGD including the circulation stage, the local bitumen was no long immobile. The condition had changed, so the results generated from the lab-scale were not suitable for steam circulation and full SAGD operation.

With the FLAC3D model, nine scenarios with elevated injection pressures were analyzed for three different potentials in-situ stress regimes (15, 18 and 21 kPa/m of minimum horizontal stresses). Each of the scenarios yielded different levels of failure between the top and bottom wells, resulting in permanent increases in water porosity and total porosity.

The results of the porosity enhancement distribution and the updated fluid saturation distribution were incorporated in the CMG STARS model. SAGD operation was mimicked to assess the effectiveness of the dilation start-up scheme. The SAGD operation was simulated for a 200 days period for all nine cases. Due to a relatively small change in initial water saturation, oil saturation, total porosity after cold-water injection and geomechanical dilation, there is little impact on the overall SAGD performance.

In theory, it makes sense that the fluid production will not vary much unless the main parameters in the reservoir have massive enhancement (e.g. the relative permeability of oil). To analyze the oil rate per unit length of well, Butler's analytical model was recalled (Butler, 1991).:

$$q_o = \sqrt{\frac{1.5 K_{rocw} g \alpha_{res} \varphi \Delta S_o h}{m \upsilon_{oS}}} \qquad \text{Eq. 5-26}$$

where K_{rocw} is the relative permeability of oil at connate water saturation condition;

g is the gravitational acceleration;

α_{res} is the thermal diffusivity of the reservoir;

ϕ is the initial porosity;

ΔS_o is the differential oil-saturation; S_o and S_{or} are the initial oil saturation and residual oil saturation$\Delta S_o = (S_o - S_{or})$;

h is the effective net pay thickness of reservoir (i.e., the distance between producer and top of the reservoir);

m is a coefficient,

υ_{os} is the kinematic viscosity of the oil at the interface.

It can be noted that both the relative permeability of oil (K_{rocw}) and the initial porosity (ϕ) have the same weight to contribute to the oil rate. The oil rate is directly proportional to the average K_{rocw} in the drainage area and ϕ. Given that there is little change in porosity and K_{rocw} in regions away from the well pair, the potential enhancement in oil rate is likely to be limited.

The results of the SAGD simulations indicated that the cumulative oil production did not have a significant enhancement within 200 days after steam commencement. A slight increase in production may be observed within the first few months when the steam chamber development and oil drainage are limited to

the near-well region. However, as the steam chamber travels further away from the enhanced permeability region, there is no obvious impact of the dilated zone on oil production. Nevertheless, the enhanced dilation start-up technique might reduce the conventional steam circulation time.

The set of lab-scale experimental tests indicated that the effective permeability to water was dramatically enhanced. However, the absolute permeability of sands did not show a significant increase during the coldwater injection. In the field-scale numerical simulation, the updated porosity and fluid saturation were employed accordingly. However, just as indicated in the lab-scale experimental results, the absolute permeability associated with the injection of water into the specimen decreased moderately, along with decreasing effective stress during pore pressure injection. Therefore, the initial absolute permeability was utilized in the CMG simulation. That was one of the main factors which resulted in an insignificant impact on SAGD performance. Even though the porosity and fluid saturation did increase to some extension, it was not enough to bring in a significant increase in oil production and a decrease in SOR and cSOR.

In the other simulations (Li, 2006; Nassir and Walters, 2018), the absolute permeability change due to the isotropic unloading process was integrated into the numerical model using Tortike's equation. The change of effective permeability to water due to isotropic unloading was integrated using Touhidi-Baghini's equation (Touhidi-Baghini, 1998). Finally, enhanced SAGD performance was achieved.

CHAPTER 6. CONCLUSIONS AND RECOMMENDATION FOR FURTHER STUDIES

6.1. Specimen Preparation

The quality of a test specimen is critical to obtain reliable and repeatable results in a laboratory. An improved technique for specimen preparation has been developed during this study.

The tested specimens used in the lab-scale triaxial tests must be as identical as possible. The geomechanical triaxial test is destructive for a core specimen, which cannot be restored to the initial state after the test is completed. The characterization and structural matrix of the tested specimens are expected to be almost indistinguishable in terms of the grain size distribution, density, fluid saturation, and porosity along the length of core plugs. The sample preparation technique, developed and improved in this study, provides a feasible and practical method to produce such oil sands specimens with high quality.

It is reliable in reproducing and replicating almost identical oil sands samples in terms of their geophysical properties. It will greatly enhance capability for researchers to study fundamental behaviours related to reservoir engineering and geomechanical engineering.

Regarding the relative density of a core, all sands core specimens were well densified during sand packing preparation. The sands packing procedure is consistent, controllable, repeatable and reliable. Each core specimen has a uniform distribution of grain size, density, fluid saturation, and porosity along the length of a core plug. All the core specimens are representative of McMurray Formation oil sands.

It is crucial to keep the fluid saturation well distributed along the core length in the series of experiments on geomechanical dilation. All the sands specimens used and tested in the study are preserved in vacuum bags to retain fluid moisture.

The geomaterials which constitute the synthetic core specimen are well representative of MacMurray formation oil sands, which contain sands, bitumen, and water. The sands are the reclaimed/cleaned tailings sand from oil sands mining operations while the bitumen used in this study was obtained from the Mackay River SAGD project. The bitumen possessed an extremely high viscosity of 2,863,000 cP at 10˚C. The fluid-saturated in the core plug was mimicked with a 3% brine of formation water.

As each sands pore specimen is prepared under the same controllable procedures and techniques, the experimental results obtained from one sands pore specimen can be well compared with those from another.

6.2. Lab-Scale Experimental Approach

Two sets of lab-scale triaxle tests were carried out in this study. The first set contained three compression tests at elevated effective stress, from which geomechanical properties were acquired, and later inputted into the numerical model. The second set included nine cold-water injection tests under different initial stress states.

In the triaxial compression tests, three compression tests at the effective stress of 500, 1500, 3500 kPa were conducted at the drained conditions, where the pore pressure was kept constant at 2000 kPa, and pore fluid was free to move in or out of the sample. The elastic and strength parameters of the oil sands were obtained in the lab-scale tests. All the parameters measured through the triaxial compression testing could then be inputted the geomechanical models which assess the impacts of geomechanical dilation as a start-up in full SAGD performance.

The main parameters obtained from the set of triaxial compression tests include the shear stiffness, Mohr-Column envelope, friction angle, cohesion, dilation angle, and shear strength.

In the second set of lab-scale tests, geomechanical dilation tests were conducted under two different initial stress states with different stress ratios. They concluded that the relationship between the volumetric strain and the effective stress behaves differently under different initial stress states. Under the initial stress state, the relationship between volumetric strain and effective stress was only modestly non-linear. There was no definitive inflection point to identify the transition from pre-failure to post-failure behaviour. Consequently, the initial isotropic stress states provided only a temporary improvement in permeability, returning to the original measured value once the injection was stopped. However, under the anisotropic stress state, the volumetric strain increased almost linearly when the effective stress decreased at the beginning of the water injection. However, as a result of the pore pressure increase, the volumetric strains had a dramatic increase and the effective stress remained at almost the same level. It showed the promising potential to permanently enhance the effective permeability and the porosity in the dilated zone under a deviatoric stress state.

The lab-scale tests generated new correlations between porosity/effective-permeability with volumetric stress at elevated effective stress under reservoir temperature. These correlations can be incorporated in the numerical simulation. The experimental results showed that the effective permeability was dramatically enhanced under the modest level of the anisotropy stress state. Permeability change under pore pressure injection conditions was measured for five isotropic and two anisotropic initial stress states.

The experimental results suggest that when water porosity and water saturation increases, the effective permeability to water is improved. Although some of the pore space is occupied by connate water, however, it is mostly occupied by bitumen, which is very viscous and cannot flow under the low reservoir

temperature. When cold-water is injected into the oil sands formation, it will flow into the increased pore space, and result in an increase of total porosity. The water porosity, which is the product of total porosity and water saturation, will then increase accordingly.

The set of lab-scale experimental tests indicated that the effective permeability to water was dramatically enhanced. However, the absolute permeability of sands did not show a significant increase during the cold-water injection.

The experimental results deliver some fundamental constitutive data linking the geomechanical behaviour of wet/oil sands to its hydraulic-mechanical behaviour, which provides verification data for the development of a numerical model.

The set of lab-scale tests demonstrated and verified the concept of geomechanical dilation through cold-water injection. All tests were run at a consistent condition, which mimics the reservoir environment in terms of temperature, pore pressure, and stress states. The experiment results are well representative of MacMurray formations, which can help to improve the industry's ability to understand the behaviour during fluid injection.

The impacts of some key factors on volumetric strain have been identified. However, further work is still needed to confirm the observations above and determine the potential impact of stress ratio on geomechanical dilation of oil sands under the water injection scenarios.

6.3.Numerical Simulation

A reservoir modelling approach was developed and verified so that it could examine and assess the potential of cold-water injection as a dilation start-up scheme for SAGD.

Firstly, a constitutive model was established and tested for oil sands. The main geomechanical properties were obtained through the laboratory testing data, including both the deviatoric stress and the volumetric strain against the axial strain, which were tested in the geomechanical compression test on cylinder cores. The simulation results indicated that the constitutive model could capture the main mechanisms during a geomechanical compression test.

Next, single-phase fluid flow models were developed from the set of lab-scale tests for the oil sands formation. The relationship of the plastic volumetric strain versus the permeability enhancement was applied in the dilation process in the cell model rather than in the full SAGD model. The permeability and porosity updating models could capture the main mechanisms of the enhanced permeability. The permeability enhancement includes two contributing parts from the elastic dilation and the plastic dilation, respectively. Part of the strain was elastic, which was a reversible component, while the other was plastic, which was irreversible and permanent after the failure of oil sands.

Next, a geomechanical reservoir simulation was built to evaluate the SAGD performance due to an enhanced start-up operation. The set of lab-scale experimental results indicated that the effective permeability to water was dramatically enhanced. However, the absolute permeability of sands did not show a significant increase during the cold-water injection. In the numerical simulation with field size, the updated porosity and fluid saturation were employed. The initial absolute permeability was utilized in the CMG simulation. That is one of the main reasons why the impact was insignificant in SAGD performance. Even though the porosity and fluid saturation did increase to some extent, it was not enough to bring in a significant increase in oil production and a decrease in SOR and cSOR.

The results of the SAGD simulations indicated that the cumulative oil production did not have a significant enhancement even if the oil sands formation was dealt with cold-water injection. Short-term and long-term production rates did not increase significantly.

Based on the simulation results, it can draw a conclusion that the overall SAGD performance was not impacted significantly regardless of whether the oil sands formation was dealt with cold-water dilation. One of the main reasons is due to small changes in initial water saturation, oil saturation, and total porosity.

There was no obvious evidence to attest to the effectiveness of the dilation start-up process. The enhanced dilation start-up technique might shorten up the conventional steam circulation time, but the overall SAGD performance is not expected to improve. Especially, indistinguishable long-term SAGD performance can be identified between dilation start-up and non-dilation start-up for an oil sands formation.

A cold-water injection scheme is not recommended as there are not sufficient failure zones in the inter-well regions at a reasonable time and pressure under the injection scheme. This could be avoided at a lower injection pressure; however, no significant failure or permeability enhancement will occur at low pressure.

6.4. Recommendation for Future Works

With all the stress states analyzed in this work, the dilation start-up scheme could not improve the production significantly for the range of the stresses. The ultimate results seem to be more sensitive to the absolute permeability enhancement. In this work, no absolute permeability change was integrated into the simulation models.

There is also some other work to conduct in the future to evaluate and examine the impacts of geomechanical dilation on full SAGD performance.

1. The effective permeability to water was measured during and after geomechanical dilation, but the effective permeability to oil was not. To well assess the impacts of geomechanical dilation on SAGD performance, the relative permeability curves should be updated during and after geomechanical dilation.

2. A methodology and technique are desired to prepare oil sands specimens with a controllable fluid saturation in the core plug. Such a core plug can be examined to assess the impact of different initial water saturation on geomechanical dilation through cold-water injection.
3. Either a physical model or a numerical model is needed to investigate if such a dilation start-up can shorten the steam circulation time. Further work is still needed to confirm and determine the potential impact of the stress ratio on geomechanical dilation of oil sands underwater injection scenarios.
4. To well understand and evaluate such impacts of dilation start-up, the upscale technique needs developing and improving. So far, all experimental results from a core plug are directly applied to the field size formation.
5. All core specimens tested in the lab are uniformly packed with sands, so all the experimental results are suitable for a uniform and homogeneous formation. Such lab-scale tests on heterogeneous core specimens should be conducted. The test results can be applied to a field size numerical model which includes other geomaterials such as interbedded shale.
6. It is recommended to carry out a study on cyclical injection scheme, in which there are the one-hour injection and one-hour production cycles in the top and bottom wells for 10 hours. To more accurately simulate the cyclical injection start-up process, laboratory measurements are recommended to measure strength, constitutive and permeability enhancement parameters to reduce the uncertainty of the model.

Bibliography

Abbate, J. P. *et al.* (2013) 'Establishing Communication Between Well Pairs In Oil Sands By Dilation With Steam Or Water Circulation At Elevated Pressures'. USA Patent; US20130032336A1.

Abbate, J. P. *et al.* (2014) 'Establishing Communication Between Well Pairs In Oil Sands By Dilation With Steam'. USA Patent, US8905132B2.

Abdallah, K., Hamoud, M. and Chalaturnyk, R. (2014) 'Experimental Studies: Shear-induced in single-phase permeability', *SPE Heavy Oil Conference, Calgary Alberta, Canada, 10–12 June 2014.*, (SPE-170136-MS), p. 9.

Agar, J. R. G. (1984) *Geotechnical behaviour of oil sands at elevated temperatures and pressures*. Ph.D. Dissertation, the University of Alberta.

Allen, J. C. and Redford, D. (1975) 'Method for Establishing Communication Path in Viscous Petroleum-Containing Formations'. United States Patent, US3,913,672.

Anderson, M. T. I. and Kennedy, D. B. (2012) 'SPE 157918 SAGD Startup : Leaving the Heat in the Reservoir', (June), pp. 12–14.

ASTM (2000a) 'ASTM D4253-00: Standard Test Methods for Maximum Index Density and Unit Weight of Soils Using a Vibratory Table', *ASTM Standards*, 00(Reapproved 2006), pp. 1–15. doi: 10.1520/D4253-00R06.

ASTM (2000b) 'ASTM D4254-00: Standard Test Methods for Minimum Index Density and Unit Weight of Soils and Calculation of Relative Density', *ASTM Standards*, I(Reapproved 2006), pp. 1–9. doi: 10.1520/D4254-00R06E01.1.3.

ASTM (2003) 'ASTM D698: Standard Test Methods for Laboratory Compaction Characteristics of Soil Using Standard Effort', 3.

Boonen, P. *et al.* (2005) 'Analysis of LWD Propagation Resistivity Data in Anisotropic, Thinly-Bedded Formations Identifies Significantly More

Hydrocarbons', *SPE 95894*, pp. 1–8.

Brodsky, N. S., Getting, I. C. and Spetzler, H. (1985) 'An Experimental and Theoretical Approach to Rock Deformation at Elevated Temperature and Pressure', in *Measurement of Rock Properties at Elevated Pressures and Temperatures, ASTM SPECIAL TECHNICAL PUBLICATION 869*. in the book "Measurement of Rock Properties at Elevated Pressures and Temperatures" edited by Pincus & Hoskins, ASTM STP 869., pp. p37-54.

Bruno, M. S. (1994) 'Micromechanics of stress-induced permeability anisotropy and damage in sedimentary rock', *Mechanics of Materials*, 18(1), pp. 31–48. doi: 10.1016/0167-6636(94)90004-3.

Butler, R. M. (1979) 'Method for continuously producing viscous hydrocarbons by gravity drainage while injecting heated fluids'. United States Patent, US4,344,485.

Butler, R. M. (1991) *Thermal Recovery of Oil and Bitumen*. 4th Print, *Chemical and Petroleum Engineering*. 4th Print. GravDrain Inc.

Butler, R. M. and Stephens, D. J. (1981) 'The Gravity Drainage of Steam-heated Heavy Oil to Parallel Horizontal Wells', *JCPT*, 02(07).

Cenovus (2014) *Cenovus Christina Lake In-situ Oil Sands Scheme (8591) 2013 Update*. Available at: https://www.aer.ca/documents/oilsands/insitu-presentations/2014AthabascaCenovusChristinaSAGD8591.pdf.

Chalaturnyk, R. J. (1996) *Geomechanics of the Steam Assisted Gravity Drainage Process in Heavy Oil Reservoirs*. University of Alberta.

Chalaturnyk, R. J. and Scott, J. D. (1997) 'Geomechanical Response of Heavy Oil Reservoir to the SAGD', *SPE 37569*.

Chhina, H. S. *et al.* (1987) 'A Horizontal Fracture Test In The Athabasca Oil Sands', *Petroleum Society of CIM*, (Paper No. 87-38-56).

Coccia, C. J. R. and McCartney, J. S. (2012) 'A Thermo-Hydro-Mechanical

True Triaxial Cell For Evaluation Of The Impact Of Anisotropy On Thermally Induced Volume Changes In Soils', *Geotechnical Testing Journal*, 35(2), pp. 1–11. doi: 10.1520/GTJ103803.

Davidson, B. C. and Frederick, L. J. (2015) 'A method for determining along a length of a wellbore situated in an underground hydrocarbon-containing formation', *United States Patent Application Publication*. United States Patent, US 20150075787Al.

Davidson, B. C., Frederick, L. J. and Meling, T. (2015) 'Method For Determining Regions For Stimulation Along A Wellbore Within A Hydrocarbon Formation, And Using Such Method To Improve Hydrocarbon Recovery From The Reservoir'. United States Patent, US 2015/0075787 A1.

Davidson, B. and Spanos, T. (2004) 'Pressure Pulse Technology: An Enhanced Fluid Flow and Delivery Mechanism', in *International Conference on Remediation of Chlorinated and Recalcitrant Compounds*.

Dusseault, M. B. (1977) *The Geotechnical Characteristics of The Athabasca Oil Sands*. Ph.D. Dissertation, the University of Alberta.

Dusseault, M. B. and Morgenstern, N. R. (1979) 'Locked sands Relative densities of locked sands', *Q. Jl Engng Geol.*, 12, pp. 117–131.

Dusseault, M. b., Soderberg, H. and Sterne, K. (1984) 'Preparation Techniques for Oil-Sand Testing', *Geotechnical Testing Journal*, 7(1), p. 7. doi: 10.1520/GTJ10478J.

Edmunds, N. and Gittins, S. D. (1991) 'Effective Steam Assisted Gravity Drainage to Long Horizontal Well Pairs', *CIM/AOSTRA 1991 Technical Conference*, pp. 1–13. doi: 10.2118/93-06-05.

Fan, Y. *et al.* (2017) 'In-Situ Catalytic Aquathermolysis Combined with Geomechanical Dilation to Enhance Thermal Heavy-Oil Production', *SPE-184981-MS*, pp. 1–14.

Git, B. L. *et al.* (2002) 'Cyclic Solvent process for insitu bitumen and heavy

oil production'. USA Patent, US 6,769,486 B2. doi: 10.1074/JBC.274.42.30033.(51).

Hamoud, M. T. (2012) *Influence of Geomechanical Processes on Relative Permeability*. MSc. Thesis, University of Alberta.

Hamza, S. M. F. (2012) *Shear-enhanced permeability and poroelastic deformation in unconsolidated sands*. MSc. Thesis, University of Texas at Austin.

Howard Douglas Plewes (1987) *Undrained strength of Athabasca oil sand*. MSc. Thesis, University of Texas at Austin.

Ivory, J. *et al.* (1987) 'Development and Testing of a Synthetic Cold Lake Oil Sand.', *Journal of Canadian Petroleum Technology*, 26(3), pp. 48–53. doi: 10.2118/87-03-05.

Ivory, J. *et al.* (2010) 'Solvent processes for SAGD and heavy oil investigation of cyclic solvent injection process for heavy oil recovery', *Journal of Canadian Petroleum Technology*, 49(9), pp. 22–33.

Khajeh, M. M., Chalaturnyk, R. and Boisvert, J. B. (2011) 'Determination of Equivalent Elastic Moduli for Coupled Geomechanical- Flow Simulation of SAGD', *Canadian Society for Unconventional Gas/ SPE*, (SPE 148977), pp. 1–13. doi: 10.2523/30280-MS.

Khan, H. (2009) *Shear Induced Relative Permeability Change in Uncemented Sands*. MSc. Thesis, University of Texas at Austin.

Khan, H. A., Olson, J. E. and Holder, J. (2011) 'Shear Dilatancy in Unconsolidated Laboratory Samples Improves Relative Permeability Performance', in *SPE The Canadian Unconventional Resources Conference, Calgary, Alberta, Canada, 15–17 November 2011*, pp. 1–11. doi: 10.2118/147474-MS.

Khodaverdian, M. and McElfresh, P. (2000) 'Hydraulic Fracturing Stimulation In Poorly Consolidated Sand: Mechanisms and Consequences', in *SPE Annual Technical Conference and Exhibition, Dallas, TX, 1-4 Oct. 2000*, pp. 715–

727. doi: 10.2118/63233-MS.

Kosar, K. M. (1989) *Geotechnical Properties of Oil Sands and Related Strata*. Ph.D. Dissertation, University of Alberta.

Kry, P. R. (1990) 'Field Observations of Steam Distribution During Injection to the Cold Lake Reservoir', *Rock at Great Depth, Maury & Founnaintraux (eds), © 1989 Balkema, Rotterdam. ISBN 90 6191 9754*, pp. 1–20.

Leung, S. K., Kry, P. R. and Wong, R. C. K. (1995) 'Visualization of Deformation in Unconsolidated Athabasca Oil Sand', in *SPE International Heavy Oil Symposium, Calgary, Alberta, Canada, 19-21 June 1995.*, pp. 637–645. doi: 10.2118/30315-MS.

Li, P. (2006) *Numerical Simulation of the SAGD Process Coupled with Geomechanical Behavior*. PhD Dissertation; The University of Alberta.

Li, P. *et al.* (2011) 'Partial-SAGD applications in the jackfish SAGD project', *Journal of Canadian Petroleum Technology November/December*, (SPE 149708), pp. 19–32. doi: 10.2118/2009-190.

Li, P. and Chalaturnyk, R. J. (2005) 'Geomechanical Model of Oil Sands', in *2005 SPE International Thermal Operations and Heavy Oil Symposium, Calgary, Alberta, Canada, 1–3 November 2005*, pp. 1–5. doi: 10.2118/97949-MS.

Li, P. and Chalaturnyk, R. J. (2006) 'Permeability variations associated with shearing and isotropic unloading during the SAGD process', *Journal of Canadian Petroleum Technology*, 45(1), pp. 54–61. doi: 10.2118/06-01-05.

Li, P. and Chalaturnyk, R. J. (2009) 'History match of the UTF phase a project with coupled reservoir geomechanical simulation', *Journal of Canadian Petroleum Technology*, 48(1), pp. 29–35. doi: 10.2118/09-01-29.

Lin, B. *et al.* (2016) 'Experimental Investigation On Dilation Mechanisms Of Land-Facies Karamay Oil Sand Reservoirs Under Water Injection', *Rock Mechanics and Rock Engineering*. Springer Vienna, 49(4), pp. 1425–1439. doi: 10.1007/s00603-015-0817-8.

Manchanda, R., Olson, J. E. and Sharma, M. M. (2012) 'Permeability anisotropy and dilation due to shear failure in poorly consolidated sands', *Society of Petroleum Engineers - SPE Hydraulic Fracturing Technology Conference 2012*, pp. 551–563. doi: 10.2118/152432-ms.

Morris, K. A. (2011) 'Innovative Use of a Pressure-Pulse Injection Tool to Increase Transmissivity in a Collection Trench', *Remediation Spring*.

Mostafa H, S., V, J. H. L. and Zubair, S. M. (2013) 'Thermophysical Properties Of Seawater: A Review Of Existing Correlations And Data', 16(10), pp. 1–67.

Muhamad, H. *et al.* (2012) 'Performance Enhancement Of VAPEX By Temporal Variation Of Solvent Injection Pressure', *Journal of Petroleum Science and Engineering*, 96–97, pp. 93–101. doi: 10.1016/j.petrol.2012.08.018.

Mukherjee, N. *et al.* (1995) 'A comparison of field versus forecast performance for Phase B of the UTF SAGD project in the Athabasca oil sands', in *6. UNITAR international conference on heavy crude and tar sands on fueling for a clean and safe environment, Houston, TX (United States), 12-17 Feb 1995*.

Nassir, M. and Walters, D. (2018) 'Permeability Enhancement of Oil Sands', *ARMA18 - 52nd US Rock Mechanics / Geomechanics Symposium*.

Oldakowski, K. (1994) *Stress Induced Permeability Changes Of Athabasca Oil Sands*. MSc. Thesis, University of Alberta.

Pang, H. *et al.* (2015) 'Numerical Simulation Of Hydraulic Fracture Propagation Of Land- Facies Ultra-Heavy Oilsands In Xinjiang Oilfield', in *13th International Congress of Rock Mechanics ISRM13 10-13 May 2015, Montreal, Canada*, pp. 1–11.

Polikar, M. *et al.* (1988) 'Preparation of synthetic oil-sand cores', *Journal of Petroleum Science and Engineering*, 1(4), pp. 263–270. doi: 10.1016/0920-4105(88)90001-0.

Scott, J., Proskin, S. and Adhikary, D. (1994) 'Volume And Permeability

Changes Associated With Steam Stimulation In an Oil Sands Reservoir', *Journal of Canadian Petroleum Technology*, 33(7), pp. 44–52. doi: 10.2118/94-07-06.

Sedgwick, G. and Miles-Dixon, E. (1988) 'Application Of XRay Imaging Techniques To Oil Sands Experiments', *Journal of Canadian Petroleum Technology*, (PETSOC-88-02-07).

Somerton, W. H. (1961) 'Thermo-Mechanical Behavior Of Porous Rocks', in *SPE of AIME, Bakersfield, Calif., November 2-3, 1961*.

Stone, T. W., Edmunds, N. R. and Kristoff, B. J. (1989) 'A Comprehensive Wellbore/Reservoir Simulator', *SPE Symposium on Reservoir Simulation in Houston,TX, February 6-8, 1989.*, (SPE 18419). doi: 10.2118/18419-MS.

Touhidi-Baghini, A. (1998) *Absolute Permeability of McMurray Formation Oil Sands at Low Confining Stresses*. Ph.D. Dissertation, University of Alberta. doi: 10.7939/R3Z31P07M.

Tran, D., Nghiem, L. and Buchanan, L. (2009) 'Aspects of Coupling Between Petroleum Reservoir Flow And Geomechanics', *43rd US Rock Mechanics Symposium 4th USCanada Rock Mechanics Symposium*, p. 14. doi: 10.13140/RG.2.1.4769.0966.

Wang, J. *et al.* (1998) 'Fluid Enhancement Under Liquid Pressure Pulsing At Low Frequency', in *Proceedings 7th Unitar International Conference on Heavy Crude and Tar Sands, , Beijing, China, October 1998*, pp. 1–9.

Wang, Xinkui *et al.* (2015) 'Experimental Study on Geomechanical Dilation during Injection', in *the SPE Canada Heavy Oil Technical Conference held in Calgary, Alberta, Canada, 9–11 June 2015.*, pp. 1–17.

Wang, X. *et al.* (2015) 'Permeability Variations Associated with Various Stress State during Pore Pressure Injection', *49th US Rock Mechanics / Geomechanics Symposium held in San Francisco, CA, USA, 28 June- 1 July 2015*.

Wang, X. *et al.* (2018) 'Experimental study on geomechanical dilation of oil sands during cold-water injection', *SPE Reservoir Evaluation and Engineering*,

21(2), pp. 433–444.

Warpinski, N. R. *et al.* (2012) 'Hydraulic Fracture Geomechanics and Microseismic Source Mechanisms', *SPE Annual Technical Conference and Exhibition, San Antonio, Texas, USA, 8-10 October 2012.*, (SPE 158935).

Wong, R., Barr, W. and Kry, P. (1993) 'Stress-strain response of Cold Lake Oil Sands', *Canadian Geotechnical Journal*, 30(2), pp. 220–235. doi: 10.1139/t93-019.

Wong, R. C. K., Samieh, A. M. and Kuhlemeyer, R. L. (1994) 'Oil Sand Strength Parameters at Low Effective Stress: Its Effects on Sand Production', *JCPT*, 33(5), pp. 44–49.

Xie, S. Y. and Shao, J. F. (2006) 'Elastoplastic deformation of a porous rock and water interaction', *International Journal of Plasticity*, 22(12), pp. 2195–2225. doi: 10.1016/j.ijplas.2006.03.002.

Yaich, E. (2008) *The Effect of Stress Paths and Shear Failure on the Permeability of Unconsolidated Sands*. MSc. Thesis, University of Texas at Austin.

Yale, D. P. *et al.* (2010) 'Large-scale laboratory testing of the geomechanics of petroleum reservoirs', *44th US Rock Mechanics Symposium - 5th US/Canada Rock Mechanics Symposium*, pp. 1–14. Available at: http://www.scopus.com/inward/record.url?eid=2-s2.0-78751542558&partnerID=tZOtx3y1.

Yale, D. P., Mayer, T. and Wang, J. (2010) 'Geomechanics of oil sands under injection', in *44th US Rock Mechanics Symposium and 5th U.S.-Canada Rock Mechanics Symposium, Salt Lake City, UT June 27–30, 2010*.

Yuan, J. Y. *et al.* (2004) 'Wet Electric Heating for Starting Up SAGD/VAPEX', in *Canadian International Petroleum Conference, Calgary, Canada, June, 2004*. Petroleum Society of Canada, pp. 1–12. doi: 10.2118/2004-130.

Yuan, J. Y. and McFarlane, R. (2011) 'Evaluation Of Steam Circulation

Strategies For SAGD Startup', *Journal of Canadian Petroleum Technology*, 50(1), pp. 20–32. doi: 10.2118/143655-PA.

Yuan, Y. (2014) 'Method for Fast and Uniform SAGD Start-Up Enhancement'. United States Patent, US 2014/0352966 A1.

Yuan, Y., Xu, B. and Palmgren, C. (2013) 'Design of caprock integrity in thermal stimulation of shallow oil-sands reservoirs', *Journal of Canadian Petroleum Technology*, 52(4), pp. 266–278. doi: 10.2118/149371-PA.

Zimmerman, R. W., Somerton, W. H. and King, M. S. (1986) 'Compressibility of Porous Rocks', *Journal of Geophysical Research*, 91(B12), pp. 12,765-12,777.